Septin-Mediated Mechanobiological Reprogramming of T Cell Transmigration and 3D Motility

Alexander S. Zhovmer [1,✉], Alexis Manning [1,#], Chynna Smith [2,#], Yashavantha L. Vishweshwaraiah [3], Jian Wang [3], Pablo J. Sáez [4], Xuefei Ma[1], Alexander X. Cartagena-Rivera [2], Rakesh K. Singh [5], Nikolay V. Dokholyan [3,6,✉], and Erdem D. Tabdanov [3,✉]

Affiliations:

1. Center for Biologics Evaluation & Research, U.S. Food and Drug Administration, Silver Spring, MD, USA
2. Section on Mechanobiology, National Institute of Biomedical Imaging and Bioengineering, National Institutes of Health, Bethesda, MD, USA
3. Departments of Pharmacology, Penn State College of Medicine, Hershey-Hummelstown, PA, USA
4. Department of Biochemistry & Molecular Cell Biology, University Medical Center Hamburg-Eppendorf, Germany
5. Department of Obstetrics & Gynecology, University of Rochester Medical Center, Rochester, NY, USA
6. Department of Biochemistry & Molecular Biology, Hershey, PA, USA

# - These authors contributed equally

Running Title: Septins Reprogram T Cell Transmigration

✉ - **Correspondence authors:**

Alexander S. Zhovmer, Tel: 1-301-402-1606: alexander.zhovmer@fda.hhs.gov
Nikolay V. Dokholyan, Tel: 1-717-531-5177: dokh@psu.edu
(Lead contact):
Erdem D. Tabdanov, Tel: 1-717-531-0003 Ext: 4430: ekt5171@psu.edu

AUTHORS CONTRIBUTIONS

E.D.T. and A.S.Z. conceived the project. E.D.T. formulated and theoretically conceptualized the problem. E.D.T. built and coordinated the research project. E.D.T. and A.S.Z. developed the experimental framework of this study, A.M., A.S.Z. and E.D.T. carried out the principal mechanobiology, cell biology, and the microscopy studies. R.K.S. designed, synthesized, purified, chemically tested and verified mammalian septins inhibitor UR214-9. N.V.D., J.W. and Y.V. performed *in silico* modeling of septin molecular dynamics and UR214-9 docking to the key mammalian septin isoforms. Y.V. made practical contributions to the biochemical studies. E.D.T. and A.S.Z. designed and microfabricated mechanobiological platforms. A.M., C.S., and A.X.C.R. made a practical contribution with live T cell AFM analysis. E.D.T., A.S.Z., A.M., C.S., Y.V., X.M., and A.X.C.R. performed experimental data analysis and interpretation. P.J.S. conducted an automated visual data processing and interpretation, image deconvolution, quantification, and wrote scripts to analyze cell migration. E.D.T. and A.S.Z. wrote and edited all versions of the manuscript. All authors read and contributed comments to the final manuscript. E.D.T. is a principal investigator and project leader. E.D.T. oversaw all aspects of this study.

ABSTRACT

T cells migrate in nearly every healthy, inflamed or diseased tissue. Such ‘all-terrain’ motility is achieved by a dynamic mechanobiological balance between amoeboid and mesenchymal-like migration modes. Here, we report that septin proteins function as a key regulator of migratory balance in T cells. We show that active septins compartmentalize the lymphocyte’s cortex into a peristaltically treadmilling ‘tube’ during avoidance response to mechanically crowding hindrances. T cell cortical peristaltism mechanically channels nucleus and cytoplasm between mechanically crowding 3D collagen fibers. Septins’ inactivation shifts T cell motility balance towards mesenchymal-like mode, characterized by distinct contact guidance and MAP4-, SEPT9-, HDAC6-mediated enhancement of microtubules and microtubule-associated dynein contractility. The non-stretchable microtubular cables secure structurally coherent cell passage through confining spaces and long-distance transmission of dynein-generated forces, which replace diminished actomyosin contractility. Thus, septins provide T cells with a structural and signaling molecular switch between actomyosin-driven amoeboid and dynein-driven mesenchymal-like migration.

Keywords: septin, transmigration, amoeboid, mechanobiology, dynein, microtubules

GLOSSARY

1. Steric interactions - objects interactions by the means of their spatial collision, determined by objects’ shapes.
2. Steric guidance - T cell navigation within crowded 3D environments, determined by the available passages around and between steric hindrances.
3. Peristaltic treadmilling - locomotion mode by the means of repeated series of polarized cell cortex extension, stabilization, and retraction, accompanied by translocation of nucleus and cytoplasm *via* circumferential cortex contractility.
4. Dynein contractility - contractile forces within a system of non-stretchable, force-transmitting microtubular cables, generated by dynein motor proteins.

INTRODUCTION

One of the focal points of immune cell mechanobiology is lymphocytes' ability to sense various physical environments and remodel its cytoskeletal organization for optimization of their shape and motility. Motility of immune cells is a multimodal mechanobiological process, since lymphocytes utilize a variety of co-existing, dynamically superpositioned locomotion mechanisms (Krummel et al., 2014, 2016; Tabdanov et al., 2021). For instance, the non-adhesive amoeboid (Renkawitz and Sixt, 2010; Tooley et al., 2009) and adhesive mesenchymal-like (Renkawitz et al., 2019; Tabdanov et al., 2021) motility modes are combined into a 'random-walk' (Krummel et al., 2014; Tabdanov et al., 2021), which is also optionally accompanied by a 3D 'paddling' mode in fluids (Aoun et al., 2020). Immune cells that transition across microenvironments with different mechanical properties and structural organization dynamically readjust the balance of superposed motility modes (Krummel et al., 2016; Renkawitz et al., 2009). The GEF-H1→RhoA signaling axis is an example of a mechanism that immune cells use to readjust the amoeboid-mesenchymal migratory balance in response to the mechanical and architectural properties of their microenvironments (Tabdanov et al., 2021). However, despite the significant progress in understanding of amoeboid-mesenchymal migratory balance, it remains largely unknown how surveilling immune cells reorganize their major cytoskeletal systems, such as actomyosin, microtubules and septins, as they rebalance superpositioned locomotion mechanisms. Due to extreme complexity of lymphocyte locomotion, the question arises on which cytoskeletal systems generate the propulsion forces and which provide cell structural integrity? The query is particularly important for understanding migration of immune cells, since they are guided by the chemical and structural cues in a manner that often forces them to undergo rapid series of extreme deformations within highly confining and sterically challenging microenvironments.

Amoeboid motility of immune cells includes a non-adhesive propulsion of T cells within a heterogeneous, structurally discrete, and sterically interactive 3D microenvironment, such as the 3D collagen matrix (Wolf et al., 2003). The amoeboid T cells do not require any specific biochemical or structural modifications to the surrounding 3D collagen matrix for the effective propulsion. Instead, amoeboid T cells rely on the extensive shape changing, and steric (*i.e.* non-adhesive) interactions with collagen that allow them to steer around collagen fibers and find available lumens for cell passage (Sadjadi et al., 2020; Wolf et al., 2003). For all sterically interactive environments, such as nano-topographic surfaces, 3D collagen matrices, and cancer tumor tissue samples, the efficiency of amoeboid locomotion is proportional to the cortical actomyosin contractility and inversely proportional to the cell-microenvironment adhesive interactions (Krummel et al., 2014; Tabdanov et al., 2021; Takesono et al., 2010). These observations highlight the role of actomyosin contractility as the driving factor in 3D shape dynamics and propulsion of amoeboid cells. Specifically, the current paradigm states that cortical actomyosin contractility drives the amoeboid locomotion by inducing extensive formation of cell blebs (Charras and Paluch, 2008), which serve as pseudopod precursors for projected cell shape extension. Such mechanistic model considers the contractile actomyosin cortex with plasma membrane as a locomotion substrate for blebs formation and as a primary generator of cytoplasmic hydrostatic pressure, which causes blebbing represented by a repeating series of destabilization and transient ruptures of binding interactions between the underlying actomyosin cortex and plasma membrane (Charras et al., 2005, 2006; Fritzsche et al., 2013). However, the model of amoeboid locomotion does not explain the spatiotemporally coordinated blebbing of 3D amoeboid cortex which is required for an effective amoeboid propulsion within the sterically dense environments. In addition, the described model does not address the alternative modes of non-adhesive cell locomotion, *e.g.* motility by the retrograde cortex treadmilling in the 'leading bleb' and cell sliding (Adams et al., 2018; Renkawitz et al., 2009) or the motility by the active cortical deformation (Reversat et al., 2020). Moreover, the current model of blebbing-based motility does not explain the 3D guidance of amoeboid cells, *i.e.* their spatially directed and persistent migration within the complex and crowded microenvironments.

Alternatively, it is hypothesized that mesenchymal-like locomotion directs the motility of immune cells (Krummel et al., 2016) and facilitates their transmigration (Filippi, 2016), or diapedesis, which is a cascade

of integrin-dependent phenotype switching events. During diapedesis, corresponding cytoskeletal reorganizations serve for effective locomotion of immune cells between the bloodstream and the organs (Ley et al., 2007; Vestweber, 2015). Multiple direct observations in a variety of cell types amount to the conclusion that mechanobiology of transmigratory cells differs from that of amoeboid cells (Balzer et al., 2012; Carey et al., 2015; Raman et al., 2013). Instead of non-adhesive amoeboid propulsion, transitioning through the highly confining blood vessel wall is initiated by integrin-dependent adhesion, mesenchymal-like cell spreading and lateral migration on the luminal 2D surface. The mesenchymal-like locomotion relies on adhesion molecules, such as intercellular adhesion molecule 1 (ICAM1), and suppression of the actomyosin contractility. The loss of actomyosin contractility causes overall mechanical and structural "fluidization" of cell cortex, which facilitates cell deformability and elongation, allowing for cell's entrance and passage through the extremely confining spaces. These phenotypic changes are regulated *via* signaling pathways different from that of high contractile motility (Balzer et al., 2012; Hung et al., 2013; Paul et al., 2017; Rolli et al., 2010; Stroka et al., 2014). Moreover, due to the extreme "fluidization" and deformability, transmigrating cells also acquire a specific actomyosin-independent and rupture-resistant organization of the cytoskeleton that supports their structural integrity during locomotion in narrow pores. For example, in highly confining microchannels (3 μm-wide), migrating T cells do not depend on the actomyosin contractility, regardless of the specific adhesion to the surrounding microchannel (Krummel et al., 2014). Instead, these cells rely on the microtubule system (Balzer et al., 2012; Kopf et al., 2020) that becomes indispensable. These observations highlight a mechanobiological antagonism between actomyosin-dependent amoeboid and microtubule-based mesenchymal-like organization of cell locomotion. However, the exact structural and signaling role of microtubules for T cell migration in sterically complex matrices and transmigration through confined spaces remains unknown.

The locomotion phenotypes of immune cells are regulated by septins, *e.g.* knockdown of selected septin isoforms improves transmigration of T cells through confining pores, whereas native septins enable amoeboid locomotion of T lymphocytes (Tooley et al., 2009). From the perspective of septins involvement in the regulation of actomyosin and microtubular systems, septins participate in circumferential constriction of the actomyosin cell cortex, which is considered a possible mechanistic link to the amoeboid mode of T cell migration (Gilden et al., 2012; Tooley et al., 2009), as well as in the microtubule-driven mitotic cytokinesis and abscission (Estey et al., 2010; Kim et al., 2011). On the structural level, septins' GTPase activity (Spiliotis, 2018; Woods and Gladfelter, 2021) is central for organization of four septin isoforms (*i.e.* SEPT2, SEPT6, SEPT7, and SEPT9) into non-polar filaments with hexameric and/or octameric palindromic repetitions, such as 2-6-7-7-6-2 or 2-6-7-9-9-7-6-2 respectively. The assembled septin filaments are involved in the stabilization of the contractile actomyosin network structures, such as stress-fibers (Dolat et al., 2014; Schmidt and Nichols, 2004; Spiliotis and Nakos, 2021) and various cytoskeletal contractile circumferential bands within the cell cortex (Founounou et al., 2013; Kinoshita et al., 2002; Mostowy and Cossart, 2012). Thus, from the mechanobiological perspective, the current paradigm assigns septins a role of stabilizers of actomyosin structures that ensure the accumulation of substantial contractile energy (Dolat et al., 2014; Schmidt and Nichols, 2004) required for amoeboid contractile T cell cortex dynamics (Gilden et al., 2012; Tooley et al., 2009) and the cortex-driven cell mitosis cytokinesis (Estey et al., 2010). Recent reports indicate the involvement of a selected range of septin isoforms into the actomyosin-microtubules signaling axis, *e.g.* septin-9's translocation from the actomyosin-associated polymerized septin filaments, followed by its binding to microtubules causes a suppression of microtubules plus-end instability, leading to the enhancement of the microtubular apparatus (Nakos et al., 2019). Moreover, a recently found MAP-like motif in SEPT9_i1 isoform (Kuzmić et al., 2021a) suggests a dual role of septins as both an actomyosin supporting cytoskeleton, as well as a regulating factor for microtubular signaling *via* septin-9 shuttling between actomyosin and microtubules (Kremer et al., 2005). Notably, a loss of septin-9 (SEPT9 -/-) leads to a partial loss of fibroblast transmigration efficiency, highlighting a possible causative link between T cell transmigration and septin activity status (Füchtbauer et al., 2011), determined by the microtubular apparatus (Kopf and Kiermaier, 2021; Kopf et al., 2020). Similarly, active SEPT7 isoform is reported as the MAP4 binding

factor that prevents MAP4-microtubules binding and MAP4-mediated microtubules stabilization (Kremer et al., 2005; Permana et al., 2005), indicating an interconnection between actomyosin and microtubules *via* septins dynamics. Therefore, we hypothesize that septins serve as a mechanobiological switch between amoeboid and mesenchymal-like migration.

In this report, we test whether activity of septins regulates cytoskeletal reorganization, shape and migration of primary human T cells during mechanobiological sensing of various physical environments. We demonstrate that septins serve as mechanosensitive F-actin cross-linkers. In response to steric cues, septins scaffold and shape spheroid cortex of amoeboid cells into peristaltically treadmilling 'tube' which is partitioned into lined-up compartments with discrete actomyosin contractility. The acute inhibition of septins causes an abrupt loss of the amoeboid phenotype and transitioning to the microtubules-dynein-mediated contractility that facilitates mesenchymal-like adhesion and spreading. Finally, we suggest a mechanobiological model of T cell migration and transmigration that combines synergistic forces of actomyosin-driven amoeboid peristalticity and dynein-driven mesenchymal-like migration, conducted over long-distance *via* non-stretchable microtubular cables.

RESULTS AND DISCUSSION

Septins stabilize tensile actomyosin

Human T cells (*e.g.* human CD4+ T cell, *i.e.* hCD4+) robustly compartmentalize their cortex during migration within the 3D collagen matrix **(Figure 1a)**. Cortex compartmentalization results with T cell reorganization into multiple spheroid segments, separated by circumferential, F-actin-dense, cortex-indenting, and visually constricting furrows, *i.e.* cortical rings **(Figure 1a**, *F-actin, arrows***)**. The repetitive distribution of cortical rings effectively reshapes the cell cortex into a multi-segmented cortical tube that constricts and deforms the passing nuclei **(Figure 1a**, *nucleus, arrows***)**, thus, displaying a mechanical tunneling effects for translocating nuclei along the cortical tube. Notably, the observed circumferential cytoskeleton-dense structures are reminiscent of the septin-stabilized membranous and/or cortical rings, reported in the yeasts (Oh and Bi, 2011) and some mammalian cells (Bridges and Gladfelter, 2015; Founounou et al., 2013). Indeed, T cell cortex composition analysis identifies septins as the predominant component of the leading F-actin-enriched ring **(***e.g.* septin-7, **Figure 1b-c**, **+DMSO)**, which is in line with the previously reported correlative link between septins (*e.g.* septin-7) and T cell amoeboid behavior (Tooley et al., 2009). Thus, reliable instrumentations, *i.e.* methods of perturbation of septin activity, are needed to examine and test the involvement of the septins in T cell compartmentalization and motility.

Considering the inherently heightened rate of cytoskeletal dynamics in the migrating T cells compared to non-immune cells, we are seeking to detect the immediate effects of septin activity modulation in real time during 3D migration, *i.e.* using an acute method of septin inactivation. We propose that acute septins inactivation, achieved in short-term experiments, will predominantly demonstrate most immediate, cell motility-relevant, detectable in real time, and direct effects caused by changes in septins' activity dynamics. This strategy will also help to avoid the effects of the softer long-term perturbation of septins in primary T cells that may feature more complex, cumulative, non-linear, and often poorly decipherable secondary downstream effects. To reach this goal we focus on developing a small molecule pharmacological strategy with a selective septin inhibitor to achieve an abrupt and detectable loss of previously reported septin-actomyosin interactions (Cheffings et al., 2016; Dolat et al., 2014; Founounou et al., 2013; Salameh et al., 2021; Schmidt and Nichols, 2004) and septin-mediated amoeboid cell behaviors (Gilden et al., 2012; Tooley et al., 2009).

To achieve acute septins inhibition, we focus on the recently designed low-molecular mammalian septins inhibitor UR214-9 (**+UR214-9**, 40 μM) (Kim et al., 2020; Singh et al., 2020; Zhovmer et al., 2021). The UR214-9 is a fluoride-derived analogue of the fungal (*i.e.* yeast) septin inhibitor forchlorfenuron (FCF) (Hu et al., 2008). Unlike FCF, the UR214-9 displays a negligible cytotoxicity for mammalian cells, suitable for a

‘high dose-short term’ acute cell treatments (Zhovmer et al., 2021). To estimate whether the UR214-9 molecule displays competitive septin-docking energies in comparison to GTP, GDP and FCF at the septin molecules’ GTPase sites, we first aim for an *in silico* molecular modeling for septin-inhibitor and septin-GTP/GDP docking and energy of interactions. The calculated docking energies for all docking interactions between septins protein molecules and GTP, GDP, UR214-9 and FCF molecules display the competitive and comparable interactions energies for all listed molecules, while UR214-9 also displays more optimal docking energies than that of FCF for human septin-2, -6, -7 and -9 **(Figure SI1a)** in both pocket 1 (septin-7, **Figure SI1b-1**), and pocket 2 (septin-7, **Figure SI1b-2**). See **Figure SI2** for a detailed view of all docking configurations for all filamentous septin isoforms.

Next, we examine the effect of the UR214-9-mediated septin's inhibition on the contractile actomyosin structures. We choose the mesenchymal triple negative adenocarcinoma MDA-MB-231 cell line as a model of prominent and identifiable contractile actomyosin structures, *i.e.* stress-fibers. Acute septins inhibition in these cells **(+UR214-9)** results in an *en mass* translocation of septins (*e.g.* innate septin-9, immunofluorescent analysis) from the stress-fibers to the cytosol within the first hour **(Figure SI1c**, **+DMSO** *vs.* **+UR214-9)**. Rapid septin translocation is accompanied by the structural dissolution of stress-fibers, partial cell retraction and detachment **(Figure SI1c**, **+UR214-9**, 1 hour**)**. A prolonged course of the UR214-9 treatment results in further retraction of cell and translocation of septin-9 onto the microtubules, with the latter in turn reorganizing into the cell-deforming circumferential microtubule (MT) bands **(Figure SI1c**, **+UR214-9**, 4 hours**)** (Zhovmer et al., 2021). During the first hour after the addition of UR214-9 to the live cells, transfected with GFP-septin-9 (*i.e.* septin-9-overexpressing cells), we also observe a collapse and disintegration of septin-9-positive filaments network into the curled fragments **(Figure SI3a**, **+DMSO**, **+UR214-9**, 1 hour**)**.

Extended cell UR214-9-treatment beyond 1 hour displays progressing translocation and accumulation of GFP-septin-9 further into the microtubular rings in the retracted cells **(Figure SI3c, +UR214-9**, 4 hours**).** Alternatively, suppression of actomyosin contractility by myosin II inhibition with Blebbistatin results in a similar collapse of the pronounced stress-fibers decorated with septin-9, as shown for GFP-septin-9 distribution in MDA-MB-231 cells **(Figure SI3b**, **+Blebbistatin**, 50 μM, 1 hour**)**. Thus, active septin filaments demonstrate a preferential colocalization with the major tensile F-actin structures, but dissociate from the actomyosin cytoskeleton upon its acute mechanical relaxation **(+Blebbistatin)**, indicating septins’ binding preference to the mechanically stressed actomyosin. Acute septin's inhibition **(+UR214-9)** results in a similar translocation of septins from the actomyosin (stress-fibers), which is also accompanied by their rapid disassembly. Thus, the septins filaments and actomyosin contractile structures are mutually interdependent, where the septins stabilize the contractile actomyosin, while loss of myosin-driven F-actin contractility destabilizes the associated septin structures.

To confirm a bias of septins’ subcellular distribution (*e.g.* septin-9) towards tensile actomyosin structures, we enhance the mechanical and spatial actomyosin anisotropy by presenting the MDA-MB-231 cells to the biomimetic collagen ‘fibers’ (*i.e.* collagen type-1 orthogonal grid: 1 μm-wide micro-lanes, spaced with 15 μm pitch, G’=50 kPa). The ‘fibrous’ surrogate of an extracellular matrix induces adhesion and biaxial spreading of mesenchymal cells (Tabdanov et al., 2018a; Zhovmer et al., 2021), resulting in a polygonal cell configuration with arching free cell edges **(Figure SI3c)**. Since the anisotropic (*i.e.* linear) arching free cell edges cause actomyosin linear organization, the resultant linear tension subsequently reinforce the tensile stress-fibers buildup at the cell periphery *via* positive mechanosensory feedback **(Figure SI3c**, **+DMSO**, *arrows***)** (Tabdanov et al., 2018a; Théry et al., 2006). Thus, a major fraction of actomyosin filaments that also experience the highest linear mechanical tension in the cells assembles at the peripheral free cell edges (*i.e.* arcs) (McEvoy et al., 2017; Théry et al., 2006).

Immunofluorescent analysis of septin distribution in the polygonal MDA-MB-231 cells shows that septin-9 replicates spatial distribution of the tensile linear actomyosin, displaying a robust accumulation bias at the

concave free cell edges. Thus, our observations indicate that septin filamentous structures display a strong spatial and structural affinity towards the tensile actomyosin **(Figure SI3c**, **+DMSO,** single cell view, *arrows*; **Figure SI4**, **+DMSO**, population-wide view, *arrows***)**. Septins activity inhibition *via* UR214-9 treatment abrogates the accumulation of septin-9 within peripheral arc and drives its translocation onto the microtubules **(Figure SI3c**, **+UR214-9**, single cell view, *arrows*; **Figure SI4**, **+UR214-9**, population-wide view, *arrows***)**. We note that translocation of septin-9 onto the microtubules in the fully spread polygonal MDA-MB-231 cells increases MT density **(Figure SI3c**, **+DMSO** *vs.* **+UR214-9)**, while also inducing MT curling into the rings in ~80% of the cell population **(Figure SI3c**, **SI4**, **+UR214-9**, *arrows***)**. This observation complements our previous report on septin-9-mediated MTs reorganization in mesenchymal cells, induced by the kinesin overactivation *via* septin-9→kinesins signaling axis, and kinesin-mediated microtubule cross-linking, sliding, curling and bundling into the rings (Zhovmer et al., 2021). We suggest that UR214-9-induced septin-9 translocation onto MTs occurs *via* septin-9 shuttling mechanism between septin-9's (i) free cytosolic state, (ii) filamentous pool within septin-actomyosin contractile cytoskeleton, and (iii) septin-9 deposition on microtubules. Specifically, in a dynamic state, the cytosolic septin-9 adds to the 7-6-2-2-6-7 septin hexamers (Bai et al., 2016; Kim et al., 2011; Neubauer and Zieger, 2017), resulting in the formation of the 9-7-6-2-2-6-7-9 octamers. Similarly, UR214-9-inactivated and released septin-9 directly adsorbs to MT (Zhovmer et al., 2021). In support of this mechanism, a MAP-like motif has been identified for the SEPT9_i1 (*i.e.* septin-9, isoform 1), which facilitates SEPT9_i1 binding to the MTs (Kuzmić et al., 2021a).

We demonstrate that active septins serve as mechanosensitive F-actin cross-linkers that preferentially stabilize tensile actomyosin structures. This data supports previous findings that homozygous loss of septin-9 in mouse embryonic fibroblasts causes loss of stress fibers and associated long septin filaments (Füchtbauer et al., 2011). Recent reports also indicate that overly active cross-linking of the contractile cortical F-actin (*e.g.* by filamin-A and/or fascin) induces condensation of the circumferential cortical structures in sterically confined non-adherent cells (Adams et al., 2021). Thus, from the perspective of the actomyosin organization and condensation dynamics, the reported circumferential structures are analogous to the stress-fibers, yet tend to acquire a circular form, locking onto themselves within the cortex, rather than onto the adhesive focal adhesions (Adams et al., 2018; Liu et al., 2015). Consequently, the cortical cross-linking and circumferential condensation of cortical actomyosin bands into contractile structures lead to the compartmentalization of cell volume into a leading bleb and the main body that are separated by a densely cross-linked F-actin ring. The ongoing cross-linking of dynamically assembled actomyosin cortex within the leading bleb creates contractility gradient and drives bleb's cortex treadmilling that powers the amoeboid-like cell sliding between two non-adhesive, yet confining parallel flat surfaces. Described sliding locomotion is based on active friction between the cell cortex and the confining microenvironment. We conclude that septins may share a similar organizing role onto the actomyosin cortex of immune cells, which warrants a focused study of septins-mediated amoeboid motility of T cells.

Septins maintain amoeboid organization of T cells

To understand the mechanisms of septins' involvement (Gilden et al., 2012; Tooley et al., 2009) into the amoeboid locomotion of T cells (Wolf et al., 2003), we examine structural reorganization of the septin and actomyosin cytoskeletons in human CD4+ (hCD4+) T cells during their response to the surrounding 3D collagen matrix, while perturbing septins' activity. As mentioned above, T cells actively migrate through the 3D collagen matrix in control conditions **(+DMSO)** and display a robust compartmentalization of cortex by septin- and F-actin-enriched circumferential cortical rings **(Figure 1b-d**, **+DMSO)**. We note that the resulting compartmentalized cell cortex 'tube' features robust peristaltic treadmilling dynamics **(Movie 1)**. Namely, the compartments display an active, contractility-driven segment-to-segment translocation of cytoplasm and nucleus passing through the F-actin-dense cortical rings **(Figure 1b-d**, **+DMSO**; **Movies 2** and **3)**, similar to the cell amoeboid oscillation during cortex-membrane interaction instability and blebbing (Charras and Paluch, 2008). We also note that compartmentalization allows for the T cell cortex spatial

constriction, which helps to evade and/or bypass the cell-surrounding steric hindrances, such as collagen fibers, finding available lumens between collagen fibers for the newly extending compartments (blebs) (Wolf et al., 2003).

The acute inhibition of septins **(+UR214-9)** causes an abrupt loss of the amoeboid organization in migrating hCD4+ T cells: **(1)** loss of cell segmentation, **(2)** loss of septin- and F-actin dense cortical/circumferential rings, and **(3)** cell shape reorganization with formation of multiple radial linear elongated protrusions **(Figure 1b-d**, **+UR214-9)**. In addition, inhibition of septins **(+UR214-9)** diminishes the amount of discrete septin-7-enriched intracellular and extracellular vesicular structures (*i.e.* microvesicles) **(Figure 1b, +DMSO** *vs.* **+UR214-9)** (Willms et al., 2018), causing a diffuse septin (septin-7) distribution across the cytosol. Importantly, loss of the septins-dependent amoeboid propulsion substantially reduces migration speed of T cells **(Figure 1e**, **+DMSO** *vs.* **+UR214-9)**, and decreases their effective displacement **(Figure 1f**, **+DMSO** *vs.* **+UR214-9)** within a 3D collagen gel. Similarly, inhibition of the actomyosin contractility **(+Blebbistatin)**, that powers T cell's amoeboid dynamics (Tabdanov et al., 2021; Takesono et al., 2010) reduces cell speed and displacement **(Figure 1e-f**, **+DMSO** *vs.* **+Blebbistatin)**. On the contrary, enhancement of the actomyosin contractility *via* MT→GEF-H1→RhoA signaling axis, achieved by MT depolymerization **(+Nocodazole**, 5 μM**)** (Krendel et al., 2002; Tabdanov et al., 2021; Takesono et al., 2010), substantially increases migration speed **(Figure 1e**, **+Nocodazole**, 1 hour**)**, but not the effective 3D displacement **(Figure 1f**, **+Nocodazole)** due to the reduced persistency of cell migration directionality. Alternatively, overactivation and 'locking' of the non-muscle myosin in the hypercontractile state leads to a non-productive actomyosin contractility (*i.e.* high tension, low dynamics) and collapse of T cells into immotile spheroids **(Figure 1e-f**, **+Calyculin A**, 50 nM, <1 hour**)**. It has been previously reported that dynein contractility within microtubular apparatus often plays an important role in determining the cellular 2D/3D architectures, mechanical properties, alignment and migration along the microenvironment's guidance cues (Zhovmer et al., 2021). However, perturbation of dynein's activity in the T cells within collagen matrices induces no significant changes in T cell speeds and spatial displacement during dynein inhibition with Dynapyrazole A **(Figure 1e-f**, **+Dynapyrazole A)**. Combined, these findings indicate that septins are crucial for the maintenance of amoeboid phenotype in T cells, supporting previously demonstrated effects of septin-7 genetic knockdowns (Gilden et al., 2012; Tooley et al., 2009).

From mechanistic perspective of the septins role, we postulate that stress-fibers and cortical rings are both functionally and structurally analogous to each other, as the formation of either structure is dependent, at least in part, on the scaffolding and stabilizing effects of septins (Dolat et al., 2014; Kremer et al., 2007; Salameh et al., 2021). Indeed, an anisotropic (*i.e.* linear) stress-fiber condenses from an isotropic actomyosin network, forming a load-resisting and force-generating actomyosin band between anchoring focal adhesions (Lehtimäki et al., 2021; Vignaud et al., 2021). Similarly, in T cells the septin proteins condense F-actin-enriched cortical rings as a circularized (*i.e.* anchorless) form of the stress-fiber **(Figure 1a)**, and also resists the stretching forces (*e.g.* cortex-expanding hydrostatic pressure). Thus, while anchored stress-fibers enable the mesenchymal cell's mechanosensing of the adhesive microenvironments, the non-adhesive amoeboid cells utilize the anchorless septin-scaffolded cortical rings for their motility (Charras and Paluch, 2008; van der Gucht et al., 2005; Paluch et al., 2005; Reversat et al., 2020; Wolf et al., 2003). Our findings on the septin-enriched cortical rings dynamics in the amoeboid T cells are complementary to the reported reminiscent, albeit less dynamically complex structures, such as **(1)** septin-scaffolded rings at the 'necks' of the newly budding yeasts (Oh and Bi, 2011), or the **(2)** contractile rings at the mitotic furrow in cytokinetic mammalian cells (Estey et al., 2010; Kinoshita and Noda, 2001). However, the structural and migration signature of the septins within the T cells have only been studied in 2D locomotion systems, with no specific mechanistic role for septins in amoeboid motility suggested to date (Gilden et al., 2012; Tooley et al., 2009). For instance, in the 2D migration systems, only a punctuated pattern of septin striation has been observed in the crawling amoeboid T cells during their 2D 'random-walk', while a partial knockdown-induced loss of septin-7 has been reported to result in a T cell uropod elongation and a loss of 'random-walk' efficiency (Tooley et al., 2009). Thus, our data extends and

develops the described correlative phenomenology into a causative mechanism, and directly shows that septin-enriched F-actin rings (as shown with septin-7 staining) are involved in 3D amoeboid cell compartmentalization and peristaltic treadmilling motility (Charras and Paluch, 2008). Based on the acquired data we suggest that septin-enriched cortical rings **(Figure 1b-c**, **+DMSO)** serve as a direct analogue of the septin-enriched tensile stress-fibers, previously observed in the MDA-MB-231 cells **(Figure SI3c**, **+DMSO)**. Thus, we conclude that septins template contractility of the T-cell cortex to spatiotemporally coordinate and channel cytosolic hydrostatic pressure during amoeboid migration (Dolat et al., 2014; Salameh et al., 2021).

Amoeboid propulsion represents a steric guidance

Analysis of compartmentalized T cell cortex reveals an uneven spatial distribution of phosphorylated (Ser19) myosin **(Figure 2a-1)**. Differential density of activated actomyosin between individual cortical segments **(Figure 2a-2)** indicates that each segment features an individual actomyosin contractility. This observation is in line with the observed above T cell's peristaltic translocation of cytosol and nucleus across multiple segments during 3D migration in the 3D collagen matrix **(Movie 1)**. We also note that cortical rings colocalize with the sterically confining collagen fibers, and no cortical rings are observed without cortex contact with collagen fibers **(Figure 2b**, *top***)** in the control T cells **(+DMSO)** featuring an average of 1 to 2 rings/cell **(Figure 2b**, *bottom***)**. Namely, each cortical ring forms precisely at the spatially confining collagen fibers, *e.g.* collagen fibers lumen **(Figure 1b-c**, **+DMSO**, *arrows***)**. This observation links the condensation of the T cell cortex into the segment-separating rings to the steric crowding of the expanding cortical surface with the confining, cortex-indenting environment (Reversat et al., 2020).

We propose that the formation of cortical rings at the sites of cortex indenting manifest the evasive deformation of T cells in response to the external steric cues that allows to minimize physical interactions with the external steric barriers, *e.g.* collagen fibers. Such response to the steric cues allows T cells to dynamically conform their 3D shapes to fit in between the numerous steric cues, and effectively navigate within complex microenvironments. Thus, we posit that the external steric cues, substantial enough to exert the indenting mechanical forces upon the expanding T cell surface, serve as the local triggers for the condensation of the hindrance-evasive septin-scaffolded cortex constrictions in the form of the cortical rings. Indeed, septins are the prominent sensors of the plasma membrane curvatues, displaying their preferential supramolecular local assembly at the sites of null curvatures (*i.e.* indentations) on the inside surface of the positively curved (*i.e.* spheroid) plasma membrane (Beber et al., 2019). Thus, collagen fiber-induced indentation in the T cell cortex is an inherent trigger for local septins assembly into the rings precursors that scaffold and stabilize actomyosin rings formation. We also posit that cortical rings spatially coordinate formation of T cell compartments to peristaltically channel the nucleus and cytosol around steric hindrances to bypass 3D obstacles (*e.g.* collagen fibers) (Charras and Paluch, 2008; Charras et al., 2006; Paluch et al., 2005). In this model, the external 3D topography surrounding an initially spheroid T cell **(Figure 2d-1)** provides a spatial configuration of the steric and mechanical pressure stimuli, guiding a series of T-cell compartmentalization events and peristaltic translocation of cytosol and nucleus between the confining fibers **(Figure 1d-2)**. We propose that for amoeboid T cells such continuously guided peristaltic locomotion represents a previously uncharacterized steric mode of contact guidance.

Based on the existing model for the stochastic cortical instability as a driving force of amoeboid motility (Ruprecht et al., 2015), we further develop the model to the non-stochastic mechanism of ECM-determined, septin-structured amoeboid T cell compartmentalization for the spatiotemporally coordinated series of peristaltic translocation of nucleus and cytosol from one cell segment to another. The resultant T cell's trajectory is the nucleus' zigzag-like translocation between the principal segments, formed and spatially configured in response to the collagen-induced septin-mediated cytoskeleton rings **(Figure 2c)**. Thus, a T-cell transition towards 3D amoeboid migration in the structurally crowded environments (*e.g.* 3D collagen, **Figures 2d-1** and **2d-2**) represents a series of discrete shrinking and newly-formed,

expanding segments, formed in between the available collagen lumens **(Figure 2d)**. In this model, cortical rings ensure the ECM-determined subdivision of the whole cell cortex into a series of relatively independent contractile segments **(Figure 2a)**. The newly formed leading segment buds on the principal, nucleus-containing compartment, while the rear segments continuously collapse into the uropod, which results in 3D amoeboid cell locomotion in the form of the 'peristaltic treadmilling' **(Figure 2f)**.

Furthermore, by virtue of septin ring-induced 'hourglass' topography of the cell surface, each cortical ring forms a sterically interactive furrow between two adjacent spheroid compartments of larger diameters. We suggest that the 'hourglass' configuration provides a transient steric lock between cell surface and confining collagen fibers **(Figure 2e)**. Thus, the 'segment-ring-segment' topographic unit of the T-cell surface represents a mechanical basis for adhesion-independent amoeboid propulsion. The suggested mechanism renders the steric cues around a T cell into a mechanical fulcrum for the lymphocyte's cortex. By inducing a ring-based cortex partitioning, collagen fibers allow for an effective cytoplasm and nucleus peristaltic translocation **(Figures 2d** and **2e)** without friction-loaded displacement of the entire T cell cortex **(Figure 2f)**. Thus, each locomotion cycle includes nucleus propulsion and hydrostatically driven initiation of a new segment. The interaction of expanding cortex, nucleus and confining collagen fibers drives septin-based condensation of a new cortical ring and separation of a new segment. The new segment's 'neck' provides for a new 'furrow-fiber' steric lock as a mechanical fulcrum for further nucleus/cytosol translocation from the principal segment into the new leader segment. Concurrently, the utilized cortical segments, that are located behind the nucleus, undergo a gradual degradation, recycling and compaction, which manifests as the cylindrically shaped uropod **(Figure 2f)**. Indeed, live imaging of the multisegmented hCD4+ T cell within the 3D collagen matrix shows that during locomotion a lymphocyte repeatedly forms leading segments **(Figure 2c**, **Movie 1)**, which results in the zigzagging T cell migration trajectory around collagen fibers in 3D matrix through the available lumens.

We show that septins facilitate amoeboid dynamics by partitioning the spheroid actomyosin cortex into discrete actomyosin compartments. The formed actomyosin compartments line up into the cylindrical peristaltic 'tube' **(Figure 2d-f)**. The ring-based partitioning provides the mechanical and structural basis for amoeboid cells to optimize configuration of cortical forces for locomotion through the series of narrow lumens in complex 3D microenvironments. Specifically, septin-based regulation of cortical actomyosin allows contractile amoeboid T cells to adapt their shapes to the pre-existing spaces, lock on the collagen fibers and exert force sufficient enough for propulsion across the surrounding microenvironment. We propose that this model complements the previously described mechanism of actin cortex treadmilling in amoeboid melanoma cells (Adams et al., 2021; Logue et al., 2015). Indeed, although the basis of the cell motility in the melanoma cells is cortex treadmilling within a lasting leader bleb that drives friction-based cell sliding, it is only compatible with the ideal "sandwich"-like microenvironments. On the other hand, dynamic compartmentalization of the cell cortex by ECM topography-sensitive cortical rings provides a discrete and adaptive 'hindrance-evasive' motility of immune cells within complex 3D matrices. Specifically, cortex compartmentalization enables segment-wise or 'quantized' cortex treadmilling and stronger cell-environment steric interactions *via* T cell 'hourglass' surface topography. The transient 'hourglass' locking onto the ECM facilitates an effective mechanical fulcrum between a cell and surrounding collagen fibers, whereas peristaltic translocation of the cytosol and nucleus provides an energy-efficient propulsion mechanism, which does not require extensive friction-based interaction of the cell surface with a complex and sterically crowding 3D microenvironment.

Septins as a reprogramming switch from amoeboid to dynein-driven mesenchymal-like locomotion

The enhanced structural complexity and mechanical contractility of the actomyosin cortex in amoeboid T cells (Tabdanov et al., 2021; Takesono et al., 2010) allows them to redistribute cortical stresses regardless of the configuration of the underlying 2D adhesive guidance cues. Thus, amoeboid T cells are largely unresponsive to the flat 2D contact guidance cues (Aoun et al., 2020; Tabdanov et al., 2021), and despite

the T cells' active adhesiveness to the ICAM1 *via* LFA1 integrin receptors (Aoun et al., 2020; Krummel et al., 2014). Instead, the crawling T cells display a meandering 'random walk' that reflects a complex shape-changing dynamics within an amoeboid 3D cortex, dominating over the reduced T cell's 2D adhesion 'footprint' (Krummel et al., 2014; Tabdanov et al., 2021). There is still a substantial uncertainty about the contribution of two principal cytoskeleton components, *i.e.* actomyosin and microtubules, to the adhesion-free cortex dynamics (Krummel et al., 2016), since shifting T cells away from the amoeboid phenotype with contractility inhibitors does not enhance their contact guidance along the flat (2D) adhesion guidance cues, and the poor 2D contact guidance in T cells remains largely indifferent to the modulation of microtubules→GEF-H1→RhoA signaling (Tabdanov et al., 2021). Thus, an alternative cytoskeleton component is required to explain the observed instances of *in vivo* migratory compliance of T cells to the adhesion guidance cues (Krummel et al., 2016).

Since the complex mechanics of 3D amoeboid cortex interferes with T cell's ability to conform to the underlying 2D adhesion guidance cues (Krummel et al., 2014), we propose that downregulation of amoeboid cortex dynamics *via* suppression of septins activity may enhance T cells' conformity to 2D guidance cues, *i.e.* contact guidance. To test this hypothesis, we put T cells on a substrate designed to reveal cell shape and migration compliance in the form of their alignment to the 2D anisotropic adhesive contact guidance cues, *i.e.* 1 μm-wide, 15 μm-pitched ICAM1 micro-lanes **(Figure 3a)**. Our results show that in the control conditions **(+DMSO)**, T cells display a strongly amoeboid, *i.e.* 'random walk' crawling dynamics, and cells have no detectable structural or migratory alignment to the ICAM1 micro-lanes **(Figure 3a-c**, **+DMSO**, **Movies 4**, **5** and **6)**. The detailed analysis of T cell migration on the ICAM1 micro-lanes shows that T cells display a random distribution of directionalities, as measured within 20 second-long timeframes **(Figure 3b, +DMSO)**, and highly meandering migration tracks of individual cells **(Figure 3c, +DMSO)**. On the contrary, acute septins inhibition **(+UR214-9**, $t \ll 1$ hour**)** induces an abrupt transition to a mesenchymal-like T cells' alignment and elongation along the ICAM1 micro-lanes **(Figure 3a**, **+UR214-9)**, accompanied with highly aligned and persistent migration along the ICAM1 micro-lanes **(Figure 3b-c**, **+UR214-9)**. The migration speed of amoeboid T cells **(Figure 3d**, **+DMSO**) is routinely higher (~22 μm/min) compared to the mesenchymal-like leukocytes migration mode (~7.5 μm/min, **Figure 3d**, **+UR214-9**), which reflects a higher rate of the amoeboid cortex shape dynamics, compared to the rate of cytoskeleton reorganization, configured by the mesenchymal-like adhesion (Krummel et al., 2014). Therefore, the inhibition of septins suppresses the cortical ring formation **(Figure 1b-c**, **+UR214-9)**, turns off the amoeboid migration in 3D collagen gels **(Figure 1b-f**, **+UR214-9)**, and switches migration of T cells from 'random walk' towards a mesenchymal-like alignment along the ICAM1 micro-lanes **(Figure 3**, **+UR214-9)**.

Notably, along with the T cell amoeboid-to-mesenchymal-like phenotypic transition **(+UR214-9)**, septins inhibition induces a substantial increase of microtubules' density and length **(Figures 3a**, **4a**, **SI5a**, **+DMSO** *vs.* **+UR214-9)**. We confirm UR214-9-induced MT-enhancement using comparative measurements of MT density in control **(+DMSO)** and UR214-9-treated T cells **(Figure 4b-c)** by live cell SiR-Tubulin flow cytometry. The results generated with hCD4+ and hCD8+ T cells display ~60% and 45% increase of MT network density, respectively, during septin inhibition **(+UR214-9,** 1 hour**)** in comparison to the control **(+DMSO)** conditions **(Figure 4c)**. The UR214-9-induced growth of MT density and length (see also **Figures 3a**, **4a** and **5c**) is reminiscent of the Taxol-mediated MTs stabilization (Tabdanov et al., 2021), which increases MT network passive rigidity. Indeed, UR214-9-induced microtubule build-up demonstrates a substantial similarity between UR214-9- and Taxol-mediated effects on the increase of T cell mechanical rigidity **(Figure 4d)**. Notably, addition of Blebbistatin to either UR214-9 or Taxol treatments does not soften the T cells to the rigidities observed in a sole Blebbistatin treatment **(Figure 4d, ±Blebbistatin** *vs.* **+UR214-9±Blebbistatin** *vs.* **+Taxol±Blebbistatin)** or in a control condition **(+DMSO**, baseline mechanical rigidity**)**. Since we have previously demonstrated that Nocodazole-induced T cell rigidification is completely reversed by Blebbistatin co-treatment to the rigidity level of T cells in Blebbistatin alone (Tabdanov et al., 2021), the heightened T cell rigidities during **+UR214-9±Blebbistatin** or **+Taxol±Blebbistatin** treatments are attributed to the addition of the passive mechanical rigidity of stabilized MT apparatus. This observation

indicates that MT enhancement is associated with mechanobiological reprogramming of T cells towards non-amoeboid MT-based T cell rigidification. Specifically, septins inhibition with UR214-9 causes its release from actomyosin and relaxation of the amoeboid cortex (Dolat et al., 2014). Moreover, septins inhibition-induced microtubules stabilization may cause an uptake of cytosolic GEF-H1 with a subsequent reduction of the RhoA→actomyosin contractility signaling axis (Tabdanov et al., 2021; Takesono et al., 2010), whereas enhanced microtubules compensate for the diminished mechanical contribution of actomyosin to the cell rigidity.

Along with the increase of microtubules' density and length, we observe an increase of MTs post-translational modifications, *i.e.* MT acetylation (~20%) and detyrosination (~25-40%) **(Figure 5a)**. This observation indicates involvement of multiple synergized contours of the mechanobiological signaling that interconnect septins, MTs and actomyosin pathways **(Figure 5b)**. Specifically, intact septin-7 suppresses MAP4 (Kremer et al., 2005), while also sustaining the downstream HDAC6-mediated MT deacetylation (Ageta-Ishihara et al., 2013). Thus, inhibition of septin-7 converges into stabilization of the MTs network *via* both enhancement of MTs acetylation **(Figures 5a** and **SI5b**, **+DMSO** *vs.* **+UR214-9)** and MAP4-MTs binding **(Figure SI5c-d)** that also causes MAP4-induced MT detyrosination in T cells (Bustos-Morán et al., 2017) **(Figure 5a)**. Additionally, SEPT9_i1 isoform binds to microtubules *via* its MAP-like motif (Bai et al., 2016; Kuzmić et al., 2021b; Nakos et al., 2019) resulting in stabilization of the microtubular network by preventing the MT filaments growth catastrophes (Nakos et al., 2019) and directly by septin-9 MAP-like activity (Kuzmić et al., 2021b). Thus, UR214-9-induced suppression of septins' GTPase activity, followed by disassembly of septin octameric filaments, causes a release of monomeric GTPase-inactive septin-9 from actomyosin to cytosol. Subsequently, we observe translocation of the available, cytosolic GTPase-inactive septin-9 onto the MTs *via* its MAP-like motif, resulting in the stabilization of MT apparatus, as GTPase activity is dispensable for septin-9's MAP-like MT-stabilizing activity, as shown in MDA-MB-231 cells (Zhovmer et al., 2021) **(Figures SI3c** and **SI4)**, and in hCD4+ T cells **(Figure SI5e)**. This conclusion is further supported by the observed septin-9→kinesin signaling pathway effects that cause kinesin-driven microtubules curling, looping and circularization into the MT rings **(Figures SI3** and **SI4**, **+UR214-9**, *arrows***)**, reported for various types of cells (Zhovmer et al., 2021). Along these lines, the homozygous loss of septin-9 (SEPT9 -/-) in fibroblasts has been reported to result in the loss of the transmigration efficiency, further complementing the septin-9-dependent mechanism of microtubular apparatus stabilization for cell transmigration (Füchtbauer et al., 2011).

The UR214-9-induced T cell transition from the amoeboid 'random-walk' **(Figures 3a** and **3b, +DMSO; Movies 4** and **5**, **before UR214-9)** towards the mesenchymal-like contact guidance along the ICAM1 micro-lanes micropattern, cell elongation and alignment to the ICAM1 architecture **(Figure 3a, +UR214-9**, t=30 min; **Movies 4** and **5**, **after UR214-9**, **Movie 6)** extends to the more complex ICAM1-based 2D contact guidance cues - orthogonal grids **(Figure 5c, +DMSO** *vs.* **UR214-9)**. Thus, the T cells in control conditions **(+DMSO)** display a non-spreading amoeboid morphology and meandering 'random walk' migration, regardless of the geometry of the ICAM1 grid **(Figure 5c, +DMSO, Movie 7)**. Septin inhibition with UR214-9 abruptly (bi-phasically) switches T cells to the extensive 'dendritic' spreading along the ICAM1 grid within the first 30 minutes of treatment **(Figure 5c**, **+UR214-9**, t=30 min, **Movie 8)**. The 'dendritized' T cells further evolve into the extremely elongated multi-apical morphology after ~1 hour-long UR214-9 treatment **(Figure 5c, +UR214-9**, t≥1 hour**)**. UR214-9-induced dense and elongated MT bundles constitute the core of dendritic protrusions along the ICAM1 grid **(Figure 3c**, **+UR214-9**, Microtubules view**)**. The MT stabilization by hyperacetylation through a direct suppression of HDAC6 **(+Tubacin,** 25 μM,1 hour**)** in hCD4+ T cells also partially replicates the UR214-9-induced mesenchymal-like mode transition. Tubacin-treated T cells are phenocopying the 'dendritic' T cell spreading along the ICAM1 grids **(Figure SI6a**, **+DMSO** vs. **+Tubacin)**, which is accompanied by a significant enhancement of the MT acetylation from the initially limited, MTOC-associated acetylated tubulin cluster **(Figure SI6b**, **+DMSO**, *arrows***)** to the dense and elongated acetylated MT network **(Figure SI6b**, **+Tubacin)**.

Thus, UR214-9-mediated septins inhibition induces mutually complementary, coherent and synergistic effects, *e.g.* - (1) activation of mesenchymal-like 2D contact guidance along the ICAM1 micro-lanes and grids, (2) loss of the amoeboid phenotype, and (3) enhancement of the microtubular network that supports mesenchymal-like phenotype (Vasiliev et al., 1970). These results indicate that mesenchymal-like T cell adhesion, spreading and locomotion along ICAM-1 lanes and grids are facilitated by the actomyosin-independent mechanisms. Similarly to other integrin receptors, ICAM1 receptor LFA1 is a mechanosensor (Chen et al., 2010; Hynes, 2002; Tabdanov et al., 2015). Therefore the UR214-9-treated T cells with enhanced MTs generate a sufficient tension within LFA1 β2 subunit clusters to activate and sustain T cell adhesion, spreading and mesenchymal-like migration (Nordenfelt et al., 2016), supporting the observation that in a low actomyosin contractility state, stabilization and elongation of microtubules is critically important for development and maintaining the mesenchymal cells' dendritic protrusions along the collagen type-1 contact guidance cues (Rhee et al., 2007; Shakiba et al., 2020; Tabdanov et al., 2018a, 2018b).

We suggest that dynein-driven forces within the enhanced MT network produce a substantial compensatory tension for activation of LFA1 during the lack of sufficient actomyosin tension in UR214-9-treated T cells. Indeed, microtubular network is mechanically integrated into the F-actin cytoskeleton *via* force-generating dyneins (Fokin et al., 2021; Jimenez et al., 2021), forming a singular MT/actomyosin forces transmission system, sharing the same adhesion receptors to govern T cell adhesion and spreading along extracellular cues. In our previous report, we show that dyneins ('minus' end-directed microtubule motors) drive the spreading of dendritic protrusions, mediate cell contractility, microtubule bundling and topography-mediated contact guidance in mesenchymal cells (Zhovmer et al., 2021). We demonstrate that dyneins actively pull the microtubules into the adhesion sites to facilitate cell-substrate steric interactions and cell alignment *via* the MT scaffolding effects (Tabdanov et al., 2018b). Moreover, dyneins have a similar role in the fibroblasts upon suppression of the RhoA-dependent actomyosin contractility (Kim et al., 2012). In support of the proposed dynein-based force production, we show that MT acetylation **(Figure SI5b),** that enhances dynein processivity (Alper et al., 2014; Badding and Dean, 2012), and MT detyrosination **(Figure 5a)**, that enhances uninterrupted dynein processivity along the detyrosinated microtubules (McKenney et al., 2016), are both increased in response to the septins inhibition**.** Moreover, the Blebbistatin treatment does not affect structural compliance and migrational guidance response of UR214-9-treated T cells to ICAM1 grids **(Movie 9)**. This result indicates that actomyosin contractility is both dispensable and diminished during septin inhibition-induced dendritic cell spreading. On the contrary, UR214-9-induced T cell 'dendritic' spreading and mesenchymal-like locomotion along the ICAM1 micropatterns are immediately abrogated upon addition of the dynein inhibitor, Dynapyrazole A, at the final concentration of 25 μM **(Movie 10**, **+UR214-9+Blebbistatin→+UR214-9+Blebbistatin+Dynapyrazole A)**. The retraction of dendritic protrusions in UR214-9-treated cells can be achieved directly, *i.e.* by adding Dynapyrazole A to UR214-9-treated T cells without presence of Blebbistatin **(Movie 11**, **+DMSO→+UR214-9→+UR214-9+Dynapyrazole A)**, highlighting the dispensability of actomyosin contractility during UR214-9-induced mesenchymal-like T cell adhesion and spreading. The subsequent washout experiment demonstrates the reversibility of the mesenchymal-like cytoskeleton dynamics and reorganization, *i.e.* a recovery of the T cell amoeboid migration **(Movie 11**, **washout)**. Importantly, the separate treatment with either Blebbistatin or Dynapyrazole A alone does not show any change to the pre-existing T cell amoeboid migration mode **(Movie 12**, **+DMSO→+Blebbistatin**; **Movie 13**, **+DMSO→+Dynapyrazole A)**.

Our results show that the inhibition of septins induces transition of T cells from actomyosin-driven amoeboid crawling to dynein-driven mesenchymal-like spreading on ICAM1 substrates. We suggests a model **(Figure 5d)** where pharmacological targeting of septins reprograms mechanobiological behavior of T cells between (1) actomyosin-driven amoeboid T cell locomotion **(Figure 5d-1)**, and (2) dynein-driven mesenchymal-like cell motility **(Figure 5d-2)**. The inactivation of septins reduces the dynamics of the

amoeboid cortex to the level that allows for migration compliance to the 2D adhesive guidance cues. In addition, inactivated septins stabilize the microtubular network *via* septin-7 and septin-9 pathways, hence facilitating the microtubule-mediated uptake of GEF-H1 from the cytoplasm, causing sequestration of actomyosin contractility. Furthermore, the septins-mediated stabilization of microtubules also enhances the processivity of dyneins within the MT cable network, that helps to compensate for the diminished actomyosin contractility during the adhesion-based LFA1 activation, *i.e.* in the absence of the stabilizing septin-actomyosin interactions (Dolat et al., 2014; Kremer et al., 2007; Salameh et al., 2021; Schmidt and Nichols, 2004).

Pharmacological targeting of septins reprograms transmigration of T cells

Transmigration of immune cells is a complex phenomenon that consists of a series of events to include an extreme cell body deformation such as elongation and narrowing for sliding through the confining spaces between the endothelial and epithelial cells. The process of transmigration draws a significant scientific and clinical interest, and has been extensively studied, however, the exact mechanobiological fundamentals that underpins lymphocytes' motility during extreme deformation and confinement remains largely unknown. Specifically, although it is evident that an actively generated mechanical force is required to power the transmigration process, actomyosin contractility is often diminished or dispensable in transmigrating cells (Balzer et al., 2012; Hung et al., 2013; Paul et al., 2017; Rolli et al., 2010; Stroka et al., 2014). To date, no alternative to actomyosin-based force-generating system to power cell transmigration has been suggested.

Indeed, cell entrance and rapid passage through the confining spaces requires relaxation and “fluidization” of actomyosin cortex, which facilitates structural compliance and deformability of cells **(Figure 6a)**. On the other hand, transmigrating cells require a rupture-resistant cytoskeleton to avoid extreme overstretching and loss of cell integrity. Moreover, an effective, long-distance force transmission system is necessary for a structurally and mechanically coherent, coordinated locomotion of elongated cell bodies through the narrow pores. We propose that non-stretchable microtubular cables and associated dynein-powered contractility constitute a principal cytoskeletal system that provides both the long-distance transmission of mechanical forces and the structural coherence of confined cells. Indeed, we show that in the UR214-9-treated T cells the microtubules and dyneins replace actomyosin contractility to facilitate the “dendritic” mode of T cell adhesion and spreading **(Figure 5d)**, which establishes the leading role of dynein-MT system for supporting the motility and structure in non-amoeboid, low cortical contractility cells. Complementary to these findings*,* it is reported that in extremely confining microchannels (≤ 4 μm-wide) T cells migration does not depend on the actomyosin contractility (Jacobelli et al., 2010; Krummel et al., 2014), but is critically dependent on the intact microtubular system (Balzer et al., 2012; Kopf et al., 2020). These observations highlight a mechanobiological antagonism between actomyosin-dependent amoeboid and microtubule-based mesenchymal-like organization of cell locomotion. However, the exact structural and signaling role of microtubules during cell migration in sterically crowded matrices and during transmigration through the confined spaces remains unknown.

In order to test the role of each of the two principal cytoskeletal subsystem during transmigration of primary hCD4+ and hCD8+ T cells, we examine the effects of cytoskeletal drug perturbations on cell passage through the ICAM1-coated 3 μm pores in ~10 μm-thick polycarbonate TransWell membranes **(Figure 6a)**. We suggest a mechanistic model for T cell transmigration through the pores that includes a sequence of (1) the T cell adhesion and deformation-driven pore entrance, (2) confined cell passage, and (3) exit. In this model, the microtubule-based mechanical force transmission along the pore-confined portion of the cell body becomes critical for linking all parts of a T cell on both sides of the transmigration pore **(Figure 6b)**. Mechanobiologically, a more general T cell model of migration and transmigration can be represented as a combination of the (1) actomyosin-driven/septin-structured circumferential cortical contractility **(Figure**

6c-1), and (2) axial contractility of the dynein motor proteins, mechanically transmitted along the T cell axis *via* the non-stretchable microtubular cables **(Figure 6c-2)**.

Suppression of the septin-mediated amoeboid cortical dynamics either by a direct inhibition of septin **(+UR214-9,** 25 μM**)**, or by a direct inhibition of actomyosin contractility **(+Blebbistatin**, 25 μM**)**, results with a partial (≤50%) loss of hCD4+ and hCD8+ T cell transmigration efficiencies **(Figure 6d**, **+UR214-9**, **+Blebbistatin)**. Our observations complement a previous report showing that mouse embryonic fibroblasts with homozygous loss of septin-9 (SEPT9 -/-) substantially lose their transmigration efficiency through tested 8 μm pores (Füchtbauer et al., 2011). This data indicates that amoeboid 3D cortical dynamics is an important component of the T cell transmigration. Indeed, as we highlighted before, the amoeboid cortical dynamics enables T cell-microenvironment steric interactions, required for T cell-pore engagement and entrance **(Figure 6a)**. Alternatively, the porous TransWell membrane is not a fully adequate transmigration system, as the membrane represents a dense array of adjacent pores that are capable of simultaneous engagement of several alternative T cell protrusions **(Figure 6e)**. Thus, while UR214-9-treatment may enhance microtubules-dynein contractility-driven T cell transmigration through a single pore, the same stabilized and elongated microtubules may also lead to T cell entanglement and trapping between several adjacent pores **(Figure 6a,e)**. Moreover, since force transmission includes mechanical coupling of dyneins and F-actin (Fokin et al., 2021; Jimenez et al., 2021), the loss of cortical actomyosin contractility, caused by either UR214-9 or Blebbistatin treatments may compromise the transmission of dynein-generated forces to the T cell surrounding environment, causing a loss of T cell transmigratory efficiency.

In agreement to our model's prediction about the microtubule-based mechanical force transmission along the pore-confined portion of the cell **(Figure 6b)**, the suppression of the dynein motor activity **(+Dynapyrazole A,** 25 μM**)** leads to a substantial (≤40%) loss of the hCD4+ and hCD8+ T cell transmigration **(Figure 6d**, **+Dynapyrazole A)**. However, amoeboid migration of T cells through fibrous (3D collagen) matrices displays no detectable response (*i.e.* migration speeds, displacement distances) to the acute dynein inhibition, as compared to the control cell group **(Figure 1e-f**, **+DMSO** *vs.* **+Dynapyrazole A)**. Thus, the dynein-MT-based contractility and force transmission are indispensable during transmigration in confined spaces **(Figure 6b)**, while amoeboid T cell motility in low confinement, *i.e.* within fibrous collagen gel, does not require dynein-microtubules contractility. Disassembly of the microtubules **(+Nocodazole**, 5 μM**)**, that should lead to the loss of dynein-microtubule contractility and reduction of cell transmigration, results with an inconsistent and insignificant changes of the transmigration efficiency for hCD4+ and hCD8+ T cells **(Figure 6d**, **+Nocodazole)**. Indeed, Nocodazole treatment induces multiple, mutually compensating effects, *i.e.* - we have previously determined that along with the direct and evident loss of the microtubule as a structural components of T cells, destabilization and loss of the MTs also causes a substantial increase in T cell contractility and amoeboid behavior *via* microtubules→GEF-H1→RhoA signaling axis (Tabdanov et al., 2021). Thus, the loss of the dynein-microtubules contractility is compensated by an increase of actomyosin-driven amoeboid contractility. Indeed, the recent seminal work reports that in the confined migrating dendritic cells the local microtubules destabilization induces an increased RhoA-dependent actomyosin contractility (Kopf et al., 2020). Thus, within non-branching (*i.e.* non-entangling) confining pores, Nocodazole-enhanced actomyosin contractility becomes a principal transmigration force. Therefore, a direct increase of actomyosin contractility with intact MTs *via* G-switch **(+RhoA activator II,** 3 μg/mL**)** increases T cell amoeboid dynamics (Tabdanov et al., 2021), and causes an increase of transmigration for both hCD4+ and hCD8+ T cells **(Figure 6d**, **+RhoA activator II)**, which is in line with conclusion that amoeboid and mesenchymal-like modes are synergized during transmigration.

Our model predicts that disassembly of the MT network, if combined with inactivation of septins **(+Nocodazole+UR214-9),** leads to a substantial GEF-H1-mediated increase of the actomyosin contractility, yet without the septin-mediated cortex reorganization into compartmentalized 3D architectures and microtubule enhancement. Such simplified actomyosin contractility and the absence of stretch-resistant microtubular cables are expected to lead to the extreme T cell transmigratory plasticity, albeit at the cost of

substantial loss in cell structural stability (Kopf et al., 2020). Indeed, the transmigration efficiency of both hCD4+ and hCD8+ T cells during UR214-9+Nocodazole treatments display an increased rate of T cell transmigration **(Figure 6d**, **+Nocodazole+UR214-9)**. However, transmigrated T cells display decreased sizes of the nuclei **(Figure SI7a)**, as well as cell fragmentation and enucleation **(Figure SI7b)**, pointing towards a loss of cell integrity during passage through the array of 3 μm pores.

Combined targeting of actomyosin and microtubule-dynein cell components, *i.e.* - septin, myosin and dynein, leads to a more complete arrest of hCD4+ T cell transmigration (≥75%) **(Figure 6d**, **+UR214-9+Blebbistatin**, **+UR214-9+Dynapyrazole A**, **+Blebbistatin+Dynapyrazole A)**. Specifically, septin inhibition, combined with suppression of actomyosin contractility **(+UR214-9+Blebbistatin)** leads to simultaneous relaxation of actomyosin cortex *via* Blebbistatin, and enhancement of the microtubular apparatus *via* UR214-9, the T cell transmigration is virtually halted (~95%). We attribute this effect to the combined inability of cells to perform deformation-driven pore entrance and enhanced entanglement between several pores. Since the suggested model of effective T cell migration and transmigration is based on a synergistic cooperation between septin-actomyosin and microtubules-dynein cytoskeletal subsystems, the suppression of contractility within either septin-actomyosin or microtubules-dynein subsystems leads to a partial loss of T cell transmigration **(Figure 6d**, **+UR214-9**, **+Blebbistatin**, or **+Dynapyrazole)**, whereas simultaneous inhibition of both subsystems **(***i.e.* **+UR214+Dynapyrazole A** or **+Blebbistatin+Dynapyrazole A)** leads to almost complete abrogation of T cell transmigration, in a compliance with the suggested model **(Figure 6c)**.

Based on our data, we conclude that a general model of T cell migration and transmigration should combine the circumferential septin-structured cortical actomyosin contractility and axial dynein contractility along the microtubular cables (**Figures 6c and 7**). Our data shows that actomyosin-based amoeboid and dynein-based microtubular contractile systems can act synergistically during T cell transmigration through confining spaces. However, dynein-derived forces are dispensable during 3D migration within fibrous matrices, where cell confinement is less significant, and mechanical fulcrum made of collagen fibers is an adequate support system for septin-based peristaltic propulsion of amoeboid cells (**Figure 7a**). These results are in strong agreement with previous reports (Niggli, 2003; Yadav et al., 2019), which indicate that dynamic microtubules do not contribute to the force-generating mechanisms required for amoeboid migration. Moreover, our observations complement the findings showing that microtubules control cellular coherence of dendritic cells migrating in fibrous gels (Kopf et al., 2020), as we demonstrate that non-stretchable microtubule cables also prevent T cells from rupturing during extreme deformation in confining spaces. Furthermore, our results indicate that microtubules may effectively hinder transmigration by distributing pulling dynein forces between several cell protrusions within multiple adjacent pores. Namely, non-stretchable microtubules behave as a system for long-distance force transmission cables of dynein-generated forces that can capture T cells in a ‘tug-of-war’ state between several available pores. In this mechanistic model, the peristaltic dynamics drives sterically guided amoeboid translocation of the T cell cytosolic content, while the dynein-microtubule system powers coherent long-distance tensile forces transmission along the principal axis of the entire cell body (**Figure 7b**). We expect that the unified mechanobiological model of T cell motility, that includes T cell migration and transmigration, will contribute to the improvement of immunological therapies, as well as to the prevention of immune infiltration-driven neurodegenerative diseases treatments.

STAR★METHODS

Key resources table

REAGENT or RESOURCE	SOURCE	IDENTIFIER
Antibodies		
AffiniPure Fab Fragment Goat Anti-Human IgG, Fc_{γ} fragment specific	Jackson ImmunoResearch Laboratories, Inc	Cat# 109-007-008; RRID:AB_2632440
Anti-Tubulin antibody [YL1/2]	AbCam	Cat# ab6161; RRID:AB_305329
Anti-Tubulin antibody [SAP.4G5]	Sigma-Aldrich	Cat# T7816, RRID:AB_261770
Atto 647N goat anti-mouse IgG	Sigma-Aldrich	Cat# 50185, RRID:AB_1137661
Monoclonal Anti-Tubulin, Acetylated antibody produced in mouse	Sigma-Aldrich	Cat# T6793
Anti-Detyrosinated alpha Tubulin antibody - Microtubule Marker	AbCam	Cat# ab48389
Anti-GAPDH Rabbit mAb [14C10]	Cell Signaling	Cat# 2118; RRID:AB_561053
Purified Non-muscle Myosin Heavy Chain II-A Antibody (Previously Covance catalog# PRB-440P)	BioLegend	Cat# 909801
β-actin rabbit monoclonal antibody	Cell Signaling	Cat# #8457
Rabbit polyclonal anti-MAP4 antibody	AbCam	Cat#ab224543
Alexa Fluor 488 donkey anti-rat IgG (H+L)	Thermo Fisher	Cat# a21208; RRID:AB_141709
Anti-SEPT7 antibody produced in rabbit	Sigma-Aldrich	Cat# HPA023309
Anti-SEPT9 antibody produced in rabbit	Sigma-Aldrich	Cat# HPA042564
Phospho-Myosin Light Chain 2 (Ser19) Antibody	Cell Signaling	Cat# #3675
Goat Anti-Mouse IgG Antibody, Peroxidase Conjugated	Sigma-Aldrich	Cat# AP124P
Goat anti-Rabbit IgG (H + L) Secondary Antibody, HRP conjugated	ThermoFisher Scientific	Cat# 31460
Chemicals, Peptides, and Recombinant Proteins		
HMS-31, (25-35% Methylhydrosiloxane)-Dimethylsiloxane Copolymer, Trimethylsiloxane Terminated	Gelest, Inc	Cat# HMS-301; CAS#68037-59-2
VDT-731, (7.0-8.0% Vinylmethylsiloxane) - Dimethylsiloxane Copolymer, Trimethylsiloxy Terminated	Gelest, Inc	Cat# VDT-731; CAS#67762-94-1
2,4,6,8-Tetramethyl-2,4,6,8-tetravinylcyclotetrasiloxane	Sigma-Aldrich	Cat# 396281; CAS#2554-06-5

Platinum(0)-2,4,6,8-tetramethyl-2,4,6,8-tetravinylcyclotetrasiloxane complex solution	Sigma-Aldrich	Cat# 479543; CAS#68585-32-0
SYLGARD 184 Silicone Elastomer Kit, 0.5 kg KIT	Dow Corning, Sigma-Aldrich	Cat# 4019862; CAS#68988-89-6
40% Acrylamide Solution, Electrophoresis purity reagent, 500 mL	BioRad	Cat# 161-0140
2% Bis Solution, 500 mL	BioRad	Cat# 161-0142
Streptavidin Acrylamide, 1 mg	Thermo Fisher, Life Technologies	Cat# S21379
TEMED	Thermo Scientific	Cat# 17919; CAS#110-18-9
Ammonium Persulfate, BioUltra, for molecular biology	Fluka Analytical	Cat# 09913-100G; CAS#7727-54-0
3-(Trimethoxysilyl)propyl methacrylate	Sigma-Aldrich	Cat# 6514; CAS#2530-85-0
Ethyl Alcohol 200 Proof, Absolute, Anhydrous ACS/USP Grade	Pharmco-Aaper	Cat# 111000200; CAS#64-17-5
Collagen-1, rat	Corning, NY	Cat# 354249
CellAdhere™ Type I Collagen, Bovine, Solution	STEMCELL Technologies, Inc., USA	Catalog # 07001
Mineral Oil Light Oil (Neat), BioReagent, Suitable For Mouse Embryo	Sigma-Aldrich	Cat# M8410
Fibronectin Bovine Protein, Plasma	Thermo Fisher, Life Technologies	Cat# 33010018
Genemate LE Quick DIssolve Agarose	BioExpress	Cat# E-3120-500FG
ICAM1, Human Protein, Recombinant, hIgG1-Fc.His Tag, Active	Sino Biological, China	Cat# 10346-H03H-50
Paraformaldehyde, reagent grade, crystalline	Sigma-Aldrich	Cat# P6148-500G; CAS#30525-89-4
Triton X-100	Sigma-Aldrich (Roche)	Cat# 11332481001 CAS#9002-93-1
DMSO (Dimethyl sulfoxide)	Sigma-Aldrich	Cat# 472301-100ML; CAS#67-68-5
(−)-Blebbistatin, 1-Phenyl-1,2,3,4-tetrahydro-4-hydroxypyrrolo[2.3-b]-7-methylquinolin-4-one	Sigma-Aldrich	Cat# 203391; CAS#856925-71-8
Nocodazole, Microtubule Inhibitor	AbCam	Cat# ab120630; CAS#31430-18-9
Paclitaxel (Taxol)	Sigma-Aldrich	Cat# T7402; CAS#33069-62-4
Dynapyrazole A	Sigma-Aldrich	Cat# SML2127
UR214-9	Dr. Rakesh Singh	Custom synthesis
Calyculin A	Sigma-Aldrich	Cat# 208851
Tubacin	Sigma-Aldrich	Cat# SML0065
Latrunculin A	Thermo Fisher	Cat # L12370
0.25% Trypsin, 2.21 mM EDTA, 1× [-] sodium bicarbonate	Corning	Cat# 25-053-CI

Plasmocin	Fisher Scientific	Cat# NC9698402
Penicillin Streptomycin Solution, 100X	Corning	Cat# 30-002-CI
Fetal Bovine Serum	HyClone	Cat# SH30910.03
Acetic Acid, Glacial	Fisher Chemical	Cat# BP2401-500; CAS#64-19-7
Silanization solution-I	Sigma-Aldrich	Cat# 85126; CAS#75-78-5
6.5 mm Transwell® with 3.0 µm Pore Polycarbonate Membrane Insert, Sterile	Corning	Cat# 3415
35 mm NanoSurface Dish	NanoSurface Biomedical, Seattle, WA	Cat# ANFS-0001
25 mm NanoSurface Coverglass	NanoSurface Biomedical, Seattle, WA	Cat# ANFS-CS25
35 mm Dish | No. 1.0 Coverslip | 20 mm Glass Diameter | Uncoated	MatTek Corporation	Cat# P35G-1.0-20-C
Cover Glasses, FisherFinest Rectangles, 25×60-1, Thickness 0.13-0.17 mm	Fisher Scientific	Cat# 24X60-1
Cover Glasses, Circles, 15 mm, Thickness 0.13-0.17 mm	Carolina Biological Supply Company	Cat# 633031
SiR Actin, Spirochrome Kit	Cytoskeleton Inc.	Cat# CY-SC001
SiR Tubulin, Spirochrome Kit	Cytoskeleton Inc.	Cat# CY-SC002
Phalloidin-Atto 488	Sigma-Aldrich	Cat# 49409
Phalloidin-iFluor 647 Reagent - CytoPainter	AbCam	Cat# ab176759
Bovine Serum Albumin (BSA), fatty acid-free powder	Fisher Bioreagents	Cat# BP9704-100; CAS#9048-46-8
(+)-Biotin N-hydroxysuccinimide ester	Sigma-Aldrich	Cat# H1759; CAS#35013-72-0
Alexa Fluor 568 carboxic acid, succinimidyl ester	Molecular Probes	Cat# A20003
Alexa Fluor 488 carboxic acid, succinimidyl ester	Molecular Probes	Cat# A20000
Atto 647 NHS ester	Sigma-Aldrich	Cat# 07376
Hoechst 33342, Fluorescent Dye for labeling DNA	Tocris	Cat# 5117; CAS#23491-52-3
Slide-A-Lyzer MINI Dialysis Device, 7K MWCO, 0.1 mL	Thermo Fisher	Cat# 69560
Rho Activator II	Cytoskeleton, Inc.	Cat# CN03-A
Soybean Trypsin Inhibitor	ATCC	Cat# 30-2104
Hepes (1M)	Thermo Fisher Scientific	Cat# 15630080
Phosphate Buffered Saline (PBS) pH 7.4 (1×)	Thermo Fisher Scientific	Cat# 10010023
Penicillin Streptomycin Solution, 100X	Corning	Cat# 30-002-CI

DMEM, 1× (Dulbecco's Modification of Eagle's Medium) with4.5 g/L glucose, L-glutamine & sodium pyruvate	Corning	Cat# 10-013-CV
HyClone Cosmic Calf Serum, US Origin, 500 mL, Heat-inactivated	Cytiva	Cat# SH30087.03HI
RPMI 1640 with L-glutamine	Corning	Cat# 10-040-CV
EasySep Human CD4+ T Cell Isolation Kit	STEMCELL Technologies, Inc., USA	Cat# 17952
EasySep Mouse CD8+ T Cell Isolation Kit	STEMCELL Technologies, Inc., USA	Cat# 19853
ImmunoCult Human CD3/CD28/CD2 T Cell Activator	STEMCELL Technologies Inc., USA	Cat# 10970
Dynabeads Mouse T-Activator CD3/CD28	Thermo Fisher Scientific	Cat# 11456D
"The Big Easy" EasySep Magnet	STEMCELL Technologies, Inc., USA	Cat# 18001
MojoSort Human CD4 Nanobeads	BioLegend	Cat# 480014
GE Healthcare Ficoll-Paque PLUS Media	Thermo Fisher Scientific	Cat# 45-001-750
Ammonium-Chloride-Potassium (ACK) Lysing Buffer	VWR International	Cat# 118-156-101
Dynabeads Human T-Activator CD3/CD28 for T Cell Expansion and Activation	Gibco	Cat# 11132D
CTS Immune Cell SR	Gibco	Cat# A2596101
Recombinant Human IL-2 (rhIL-2)	PeproTech	Cat# 200-02
Recombinant human IL-7 (rhIL-7)	PeproTech	Cat# 200-07
Recombinant human IL-15 (rhIL-15)	STEMCELL Technologies, Inc., USA	Cat# 78031
CTS OpTmizer T Cell Expansion SFM	Gibco	Cat# A1048501
L-glutamine (200mM)	Gibco	Cat# 25-030-081
EmbryoMax Penicillin-Streptomycin Solution, 100X	Sigma-Aldrich	Cat# TMS-AB2-C
ImmunoCult-XF T Cell Expansion Medium	STEMCELL Technologies, Inc., USA	Cat# 10981
ImmunoCult Human CD3/CD28/CD2 T Cell Activator	STEMCELL Technologies, Inc., USA	Cat# 10990
Human Recombinant IL-2, ACF	STEMCELL Technologies, Inc., USA	Cat# 78145.1
0.01% poly-L-lysine	Sigma-Aldrich	Cat# P4707; CAS#25104-18-1

Experimental Models: Cell Lines		
Human CD4+ T cells (derived from commercially supplied human whole peripheral blood).	STEMCELL Technologies, Inc., USA	Cat#70507.1
Human CD8+ T cells (derived from commercially supplied human whole peripheral blood).	STEMCELL Technologies, Inc., USA	Cat#70507.1
Human MDA-MB231 cells	ATCC, USA	HTB-26
DNA constructs		
pEGFP-C2_SEPT9 i1	Addgene	Cat# 71609
Software and Algorithms		
KaleidaGraph 5 for MacOS	http://www.synergy.com/	RRID:SCR_014980
GraphPad Prism 7b	https://www.graphpad.com/	RRID:SCR_002798
PlotsOfData	https://huygens.science.uva.nl	N/A
Adobe Illustrator CC, 21.0.0.	Adobe Systems, Inc.	RRID:SCR_010279
NanoScope Analysis 1.7	Bruker	
MATLAB R2019a	The MathWorks	
LAS X	Leica Microsystems	
Fiji	https://imagej.net/software/fiji/	
MedusaDock	https://dokhlab.med.psu.edu/cpi	N/A
Chiron	https://dokhlab.med.psu.edu/chiron	N/A
Other		
AFM Tipless Probe	MikroMasch (µMasch), Germany	Cat# HQ:CSC38/tipless/Cr-Au, HQ:CSC38/tipless/Al BS
Instant Structured Illumination (iSIM) microscopy system	VisiTech Intl., Sunderland, UK	
Leica SP8 laser scanning confocal microscopy imaging system	Leica Microsystems https://www.leica-microsystems.com/	
TokaiHit Stage Top Incubator, Model STXG-GSI2X-SET	Tokai Hit, Fujinomiya, Japan	
Leica DMi8 system	Leica Microsystems https://www.leica-microsystems.com/	
Bruker Bioscope Catalyst Atomic Force Microscope System	Bruker https://www.bruker.com/en/meta/search.html?q0=resolve	

Cell experiments

We maintained human MDA-MB-231 cells (ATCC® HTB-26™) in DMEM with 4.5 g/L D-glucose, L-glutamine,110 mg/L sodium pyruvate (Corning Cellgro®, Cat# 10013CV) and 10% heat-inactivated FBS (HyClone®, Cat# SH30071.03H) at 37ºC in 5% CO2.

Primary human CD4+ and CD8+ T cells were isolated from commercially available whole human blood (STEMCELL Technologies Inc., USA, Cat# 70507.1) with EasySep Human CD4+ or CD8+ T Cell Isolation Kits (STEMCELL Technologies Inc., USA). Unless otherwise indicated, cells were cultured, activated and expanded in ImmunoCult-XF T Cell Expansion Medium (STEMCELL Technologies Inc., USA) with the addition of ImmunoCult Human CD3/CD28/CD2 T Cell Activator and Human Recombinant Interleukin 2 (IL-2, STEMCELL Technologies Inc., USA) as per STEMCELL Technologies Inc. commercial protocol, at 37ºC in 5% CO2.

Cells were treated either in 6.5 mm Transwell® plates with 3.0 µm pore polycarbonate membrane inserts (Corning, Cat# 3415) or in glass-bottom 35 mm Petri dishes (MatTek Corp., Cat# P35G-1.5-14-C) using dimethyl sulfoxide (Sigma, Cat# 472301), (-)-Blebbistatin enantiomer (Sigma, Cat# 203391), Dynapyrazole A (Sigma, Cat# SML2127), Paclitaxel (Sigma, Cat# T7402), Calyculin A (Sigma-Aldrich, Cat# 208851), Tubacin (Sigma-Aldrich, Cat# SML0065), and septin inhibitor UR214-9 (synthesized by Dr. Rakesh K. Singh) as indicated in the main text.

Transfection of MDA-MB-231 cells with pEGFP-C2_SEPT9 i1 (Addgene Cat# 71609) was performed in Opti-MEM (Gibco, Cat# 31985-070) using SuperFect reagent (Qiagen, Cat# 301307) according to the manufacturer's protocol.

High precision micropatterning

An instructive and detailed protocol for indirect, high-definition, submicron-scale polyacrylamide gels micropatterning with various proteins is described in the original report (Tabdanov et al., 2020). Briefly, collagen type-1 micropatterning at the micron- and submicron scale spatial precision is technically complicated by the capillary and van-der-waals effects that routinely induce a collapse of the microstamp bas-reliefs, made of conventional soft regular PDMS (rPDMS, polydimethylsiloxane), onto the printed glass surface. In order to preclude the microstamps from undesirable collapsing we replaced rPDMS stamping bas-relief with a 0.5-0.8 mm-thick veneering microprinting surface, *i.e.* - hard PDMS (hPDMS) (Schmid and Michel, 2000; Tabdanov et al., 2018b), mounted on the 5-8 mm-thick cushioning rPDMS blocks. To cast the micro-printing surfaces from the commercially fabricated and passivated molding matrix of desirable design (Minnesota Nano Center, University of Minnesota), we coated molds with 0.5-0.8 mm-thick layer of hPDMS either manually with a soft paraffin spatula or on a spin coating device. The submillimeter hPDMS layer on the silicone molding matrix was then cured in a heat chamber (70ºC, 30 minutes). Next, an ~8 mm-thick layer of bubble-free rPDMS was cured atop of the hPDMS layer (rPDMS; 1:5 curing agent/base ratio, Sylgard-184, Dow Corning, 70ºC for ~1 hour). The cured micro-stamping composite was then peeled off the mold and cut into 1×1 cm pieces for the further use.

In order to assemble the elastic ICAM1 or collagen type-1 micro-patterns, we first microprinted α-Fc FAB antibody fragment (Jackson Immunoresearch, USA, Cat# 109-007-008, RRID:AB_2632440) or α-collagen-1 rabbit pAb (AbCam, Cambridge, UK, Cat# ab34710; RRID:AB_731684) on clean "intermediate" glass surface, stripped from organic impurities by the prolonged thermal treatment (FisherFinest™ Premium Cover Glass; #1, Cat# 12-548-5 P; 450ºC, baked 20 hours in the furnace). For that, the cognate antibody for collagen-1 or an antibody fragment for ICAM-1-hFc were covalently conjugated with biotin, ((+)-biotin *N*-hydroxysuccinimide ester, Sigma-Aldrich, Cat# H1759; as per the

manufacturer's protocol) and a fluorescent Alexa Fluor tag (Alexa Fluor® succinimidyl esters, Invitrogen™, Molecular Probes®, Cat# A20000, Cat# A20003; as per commercial protocol). For that, the micro-stamps were coated with the 0.2 mg/mL α-collagen-1 antibody (or anti-Human Fc FAB) PBS solution for 40 min at 37ºC in a dark humid chamber, then gently rinsed in deionized water, and dried under a jet of argon or nitrogen immediately prior to the micro-contact soft lithography procedure. Second, glass-bottom 35 mm cell culture dishes (MatTek Corp., Ashland, MA, Cat# P35G-1.0-20-C) were activated with 3-(trimethoxysilyl)propyl methacrylate (Sigma-Aldrich, Cat# 6514, as per commercial protocol) to ensure the covalent crosslinking between the glass surface and PAA gels. Third, 5 µL of PAA premix (polyacrylamide, see the "PAA elastic gel premix" section) of the projected rigidity G' = 50 kPa(Plotnikov et al., 2014a) with the addition of the 5% streptavidin-acrylamide (ThermoFisher, Cat# S21379) were, avoiding any air bubbles formation, carefully 'sandwiched' between the activated glass surface and the micropatterned intermediate glass surface promptly after adding a curing catalyst (aminopropyltriethoxysilane, APS). The resulting 'sandwiches' with cured PAA were then incubated in deionized water (1 h, 20ºC) for hypotonic PAA swelling that ensures gentle coverglass release from PAA gel. The resulting dish-bound PAA gels were checked for quality of the transferred fluorescent micropatterns on an epifluorescent microscope. Lastly, the anti-Human Fc FAB patterns on PAA were incubated with 10 µg/mL ICAM1-hFc solution (Sino Biological, Cat# 10346-H03H-50) and α-collagen-1 Ab micropatterns on PAA gels were incubated with 1 mg/mL rat monomeric collagen-1 (Corning, NY, Cat# 354249) in cold PBS (4 °C, 12 hours), then rinsed three times with cold PBS, and utilized for experiments.

hPDMS formulation

To prepare the hPDMS mixture we used 3.4 g of VDT-731 (Gelest, Inc., Cat# VDT-731), 18 µL of Pt catalyst (Platinum(0)-2,4,6,8-tetramethyl-2,4,6,8-tetravinylcyclotetrasiloxane complex solution) (Sigma-Aldrich, Cat# 479543), and one drop of cross-linking modulator 2,4,6,8-Tetramethyl-2,4,6,8 -tetravinylcyclotetrasiloxane (Sigma-Aldrich, Cat# 396281). All components were thoroughly mixed in a 50 mL conical bottom centrifuge tube on the vortex mixer for at least 30 sec. Before use, we added 1 g of HMS-301 (Gelest, Inc., Cat# HMS-301) to the mixture, promptly mixed it for 30 sec on a vortex mixer, degassed in a high-speed centrifuge (3 minutes, 3000 rpm), and immediately used it for the mold coating. The detailed protocol is described elsewhere.(Odom et al., 2002; Schmid and Michel, 2000)

PAA elastic gel premix

For PAA premixes, we utilized 40% acrylamide (40% AA) base (BioRad, Cat# 161–0140) and 2% bis-AA (BioRad, Cat# 161–0142) cross-linker as described elsewhere.(Fischer et al., 2012; Plotnikov et al., 2014b) Additionally, streptavidin-acrylamide (Thermo Fisher, Cat# S21379) was added to the final concentration of 0.133 mg/mL to enable PAA gels cross-linking with biotinylated proteins of interest for the micropatterns transfer from the intermediate glass surface to the cured PAA gels. Briefly, for preparation of 50 µL of G' = 50 kPa PAA gel premix, the components were mixed as follows: 40% AA - 15 µL; 2% bis-AA - 14.40 µL; 2 mg/mL streptavidin-acrylamide - 3.33 µL; 10X PBS - 5 µL; deionized milli-Q water - 11.17 µL; TEMED - 0.1 µL. The premix solutions were degassed and stored at 4ºC before use. To initiate curing, 1 µL of 10% APS was added to 50 µL of PAA premix immediately before the PAA gel casting procedure.

Polymerization of prestained collagen gels

To prepare 3 mg/ml collagen-I gel, we assembled a gel premix on ice in a prechilled eppendorf tube. To 1 volume of CellAdhere™ type I bovine, 6mg/mL (STEMCELL Technologies Inc., USA) we added 8/10 volume of DMEM, 1/10 volume of 10x PBS, 1/20 volume of 1M HEPES, and 1/20 volume of 1M Atto 647 NHS Ester (Sigma-Aldrich). A drop of premixed gel (~50ul) was spread immediately on a glass surface of a plasma-treated glass-bottom 35 mm Petri dish (MatTek Corp., Cat# P35G-1.5-14-C) with a pipette tip. During polymerization (room temperature, for overnight), gels were covered with 1mL of mineral oil

(Sigma-Aldrich, Cat# M8410) to prevent evaporation of water. Before adding T cells, polymerized gels were rinsed with PBS to remove the unpolymerized gel components.

Transwell assay

We coated plasma-treated polycarbonate membranes (Corning, Cat# 3415) with 100 µl of 10 µg/mL ICAM1 PBS solution (Sino Biological, Cat# 10346-H03H-50) overnight at 4ºC. Before loading cells (100 µl, 10^5 cells), we rinsed inserts twice with PBS. During the transwell assay, T cells on the upper surface of a permeable membrane of a cell culture insert migrate across pores to the collecting bottom chamber (600 µl). Following an incubation period (6 hours), we fixed cells by adding 600 µl of ice-cold (4ºC) DMEM containing 4% paraformaldehyde (Sigma-Aldrich, Cat# P6148) and 1:1000 Hoechst (Tocris, Cat# 5117) overnight, and counted the cells that migrated through the membrane. We do not use any additional chemoattractant gradient, similarly to prior work(Tooley et al., 2009), since the chemoattractant concentration quickly equalizes between the compartment below the membrane and the compartment above the membrane due to the pore size.

Synthesis of UR214-9

Equimolar mixture of 4-amino-2,6-dichloropyridine (Tokyo Chemical Industries, Cat#A2369) and 2-fluoro-3-(trifluoromethyl)phenyl isocyanate (Alrdich, Cat#472182-2G) in dimethylformamide (DMF) was stirred and heated at 65ºC in a sealed glass tube overnight. DMF was removed using a Buchi rotary evaporator. The crude reaction mixture was dissolved in a mixture of dichloromethane(DCM)+MeOH and purified by preparative thin-layer chromatography using Hexane:EtOAc (50:50) as eluent. The pure product band was scrapped off the glass plate and UR214-9 was stripped from the silica gel using DCM+MeOH through a sintered funnel. The solvent was evaporated using a Buchi rotary evaporator to obtain UR214-9 as an off-white powder. UR214-9 was dried overnight in a desiccator and analyzed by proton and carbon NMR and mass spectrometry. MS-APCI:[368.3, singlet,100%; 370.2, doublet,60%]

Super- and high-resolution and confocal imaging

Cells were fixed with ice-cold (4ºC) DMEM containing 4% paraformaldehyde (Sigma-Aldrich, Cat# P6148) for 20 minutes. PFA-fixed samples were rinsed in 1% BSA in PBS two or three times (5 minutes for each cycle), followed by 30 minute-long blocking-permeabilization treatment in 0.1% Triton X-100 (Sigma-Aldrich, Cat# T8787) solution with 10% BSA (Fisher, Cat# BP9704) in PBS (Thermo Fisher, Cat# 10010023). For immunofluorescence sample staining, we utilized primary antibodies diluted in 1% BSA PBS (all catalog numbers of antibodies are listed in Key Resources Table). The duration of the incubation with any of the listed primary antibody solutions was 1 hour at room temperature. Similarly, labelings with Alexa-Fluor-conjugated secondary antibodies (Thermo Fisher) were performed at their final concentration of 5 µg/mL for the duration of 1 hour in 1% BSA PBS at room temperature. After washing out the excess secondary antibodies, F-actin was stained either with fluorescent phalloidin or SIR-Actin for the duration of 1 hour. Chromatin was labeled with 1:1000 Hoechst solution (Tocris, Cat# 5117) added to the mounting 90% Glycerol (Sigma, Cat# G5516) in PBS media.

High-resolution 3D and 2D imaging for cell morphometric analysis were performed on a Leica TCS SP8 laser scanning confocal microscope with LIAchroic Lightning system and LAS X Lightning Expert super-resolution capacity, 405, 488, 552 and 638 nm excitation diode lasers, with 40×/1.3 oil immersion objective (Leica, Germany). The scanning settings were optimized with Nyquist LAS X function with HyD2.0-SMD excitation sensors, at the regular pinhole size of 0.85 AU, and the scanning frequency at 100 Hz. Each frequency channel was scanned in sequence in order to avoid the signal bleeding between the channels. Additionally, live cell imaging microscopy experiments were performed on epifluorescent Leica DMi8 microscope (Leica, Germany) equipped with a temperature (37ºC), CO_2 (5%), and humidity controlled

chamber at 20×, 40X and 63X magnifications. Brightfield and fluorescent images were obtained using LAS X software (Leica, Germany).

Super-resolution 3D and 2D imaging was performed using an Instant structured illumination microscopy (iSIM). The custom built instant structured illumination microscope system (VisiTech Intl, Sunderland, UK) was equipped with an Olympus UPLAPO-HR ×100/1.5 NA objective, two Flash-4 scientific CMOS cameras (Hamamatsu, Corp., Tokyo, Japan), an iSIM scan head (VisiTech Intl, Sunderland, UK), and a Nano-Drive piezo Z stage (Mad City Labs, Madison, WI). The iSIM scan head included the VT-Ingwaz optical de-striping unit. Image acquisition and system control was done using MetaMorph Premiere software (Molecular Devices, LLC, San Jose, CA). Images were deconvolved with an iSIM-specific commercial plugin from Microvolution (Cupertino, CA) in FIJI.

All analyses were performed automatically and/or manually utilizing Leica LAS X software (Leica, Germany) and the ImageJ/FIJI. Figures were composed using unmodified LAS X -generated TIFF images with Adobe Illustrator CC 2021 (Adobe).

Atomic Force Microscopy

Depending on the pharmacological drug treatment, immune cells were incubated in Immunocult-XF culture media with the respective drug concentration (Blebbistatin: 50 μM, UR2149: 50 μM, Taxol: 1 μM, Latrunculin A: 100 nM) for the given treatment condition for total times between ~15 min to 75 min. The cells were incubated in eppendorf tubes with their respective drug concentrations, followed by plating on a glass-bottom dish (Willco Wells) precoated with 0.01% poly-L-lysine (Sigma-Aldrich). Plating was done ~15 minutes before imaging to allow cells to weakly adhere to the glass-bottom dish surface and the drug to take maximum effect. AFM force spectroscopy experiments were performed using a Bruker BioScope Catalyst AFM system (Bruker) mounted on an inverted Axiovert 200M microscope (Zeiss) equipped with a confocal laser scanning microscope 510 Meta (Zeiss) and a 40x objective lens (0.95 NA, Plan-Apochromat, Zeiss). The combined microscope instrument was placed on an acoustic isolation table (Kinetic Systems). During AFM experiments, cells were maintained at physiologically relevant temperature 37°C using a heated stage (Bruker). A soft silicon nitride tipless AFM probe (HQ:CSC38/tipless/Cr-Au, HQ:CSC38/tipless/Cr-Al BS MikroMasch) was used for gentle compression of spherical weakly-adhered cells. The AFM microcantilevers were pre-calibrated using the standard thermal noise fluctuations method, with estimated spring constants for microcantilevers used between 0.04–0.12 N/m. Immediately after probe pre-calibration, the AFM tipless probe was moved on top of a spherical cell. Five to ten successive force curves were performed on each cell. The deflection set-point was set between 4-12 nm yielding applied forces between 0.16 to 1.44 nN.

All AFM force-distance curves measurements were analyzed using a custom-written MATLAB (The MathWorks) code to calculate the cellular surface cortical tension. For curve fitting, indentation depths between 0-600 nm were relatively consistent in yielding good fits (R2>0.75). Curves with poor fits R2<0.75 were discarded from the analysis. Additionally, we discarded noisy force curves and/or curves that presented jumps possibly due to cantilever and plasma membrane adhesion, slippage, or very weakly adhered moving cells.

Spherical cell cellular surface cortical tension (T; pN/μm) was calculated by fitting each recorded force-distance curve using the cortical tension method previously described that defines the force balance relating the applied cantilever force with the pressure excess inside the rounded cells and the corresponding actin cortex tension; $T = \frac{k_c}{\pi}\left(\frac{1}{(z/d)-1}\right)$, where T is the cellular surface tension, kc is the AFM cantilever spring constant, Z is the Z-piezo extension, and d is the cantilever mean deflection.(Cartagena-Rivera et al., 2016)

In silico UR214-9-Septin docking energy simulation

Swiss-Model (Schwede et al., 2003), a homology modeling based protein structure prediction tool, was used to model the structures of Septin 2, 6, 7, and 9. Since these septins have crystal structures, Swiss-Model was mainly used to complete the missing residues and atoms. Particularly, Septin 2, 6, 7, and 9 were modeled by using 6UPA, 6UPR, 6N0B, and 5CYO as the templates for homology modeling. The dimer structure of each of the septins is built by aligning two monomer structures to the corresponding positions in 2QAG, which is a septin oligomer structure. Next, the dimer structures were optimized by using Chiron (Ramachandran et al., 2011). Two pockets were identified according to the positions of the ligands in 2QAG. The two pockets are at the dimerization interface of the dimer structures. MedusaDock (Ding et al., 2010; Wang and Dokholyan, 2019) was used to dock GTP, GDP, UR214-9, and FCF to the dimer structures of the septins. Docking poses were evaluated by MedusaScore, (Yin et al., 2008) a scoring function based on a custom physics-based force field. 1000 docking attempts were performed for each of the protein-ligand pairs, and the resulting docking poses were clustered by MedusaDock to select the centroid as the final candidate.

Statistical analysis

Only pairwise comparisons as one-sided *t* tests between a control group and all other conditions are utilized to analyze the data, as well as between paired -Blebbistatin and +Blebbistatin co-treatment groups. Statistical analysis is performed using either KaleidaGraph 5 for MacOS (Synergy Software) or Prism 7b (GraphPad Software, Inc). The exact p values are indicated on the plots, unless the $p<0.0001$, *i.e.* below the cut-off lower limit for Kaleidagraph and Prism software. Sample size n for each comparison is reported in the corresponding plots (*i.e.* n reflects the number of measured individual cells). Number of replicates is 3, unless specified otherwise. Data are shown as box and whiskers diagrams: first quartile, median, third quartile, and 95% percent confidence interval.

CONFLICTS OF INTEREST

There are no conflicts of interest to declare.

DATA AVAILABILITY STATEMENT

The authors declare that the data supporting the findings of this study are available within the paper, the supplementary information, and any data can be made further available upon reasonable request.

ACKNOWLEDGEMENTS

E.D.T. and this work were supported by the Department of Pharmacology, Penn State College of Medicine *via* the startup funds. N.V.D. is supported by the NIH grant R35GM134864 and the Passan Foundation. A.S.Z., X.M., and A.M. were supported by the FDA Intramural Research Program of the Center for Biologics Evaluation and Research. A.X.C.R. and C.S. were supported by the National Institutes of Health (NIH) Intramural Research Program in the National Institute of Biomedical Imaging and Bioengineering (NIH grant # ZIA EB000094) and by the NIH Distinguished Scholars Program. P.J.S received the support of Forschungszentrum Medizintechnik Hamburg (FMTHH, grant 04fmthh2021). We thank Christian Combs and Daniela Malide for the Light Microscopy Core support at the National Heart, Lung, and Blood Institute, NIH.

MOVIES LEGENDS

Movie 1. Brightfield live video-microscopy sequence of hCD4+ T cell migrating through 3D collagen type I matrix.

Movie 2. Fluorescent visualization of the hCD4+ T cell's nucleus passage (Hoechst, cyan) through the cytoskeletal ring (SiR-actin, yellow) that constitutes a key peristaltic translocation event during T cell's amoeboid locomotion within 3D collagen matrix (magenta).

Movie 3. F-actin-dense rings (side views, seen as bands, SiR-actin live staining, yellow) form a cortical tube that peristaltically channels the nucleus (blue) *via* amoeboid passage as seen in hCD4+ T cells.

Movie 4. Wide-field view of hCD4+ T cell migration on 2D (flat) ICAM1 parallel lanes micropattern during their transitioning from predominantly amoeboid 'random walk' towards a mesenchymal-like contact guidance mode after the addition of UR214-9 septins inhibitor.

Movie 5. Detailed zoom-in view of hCD4+ T cell mesenchymal-like contact guidance along ICAM1 micro-lanes.

Movie 6. Wide-field view of the hCD4+ T cells' contact guidance along ICAM1 micro-lanes during prolonged **+UR214-9** treatment (t > 1 hour).

Movie 7. hCD4+ T cells predominantly amoeboid 'random walk' meandering on the flat 2D ICAM1 grids.

Movie 8. UR214-9-induced hCD4+ T cells mesenchymal-like spreading and dendritization along the ICAM1 grid.

Movie 9. Non-responsiveness of UR214-9-induced mesenchymal-like hCD4+ T cell dendritic adhesion, spreading and contact guidance dynamics to Blebbistatin-mediated suppression of actomyosin contractility.

Movie 10. Dynein contractility inhibition with Dynapyrazole A abrogates UR214-9-induced hCD4+ T cells mesenchymal-like adhesion, spreading and migration along ICAM1 grids. *Note that the tested T cells are co-treated with UR214-9 and Blebbistatin to demonstrate dispensable status of actomyosin contractility during mesenchymal-like T cell contact guidance mode in UR214-9.*

Movie 11. Abrogation of hCD4+ T cell's UR214-9-induced mesenchymal-like adhesion, spreading and migration with Dynapyrazole A-induced dynein inhibition (no Blebbistatin co-treatment). Following washout demonstrates partial reversibility of treatment effects.

Movie 12. Inhibition of the actomyosin contractility **(+Blebbistatin)**, unlike UR214-9 treatment, does not not induce mesenchymal-like ‘dendritic’ cell spreading.

Movie 13. Sole inhibition of the dynein contractility **(+Dynapyrazole A)** does not change hCD4+ T cell predominantly amoeboid migratory behavior on ICAM1 grids.

FIGURES

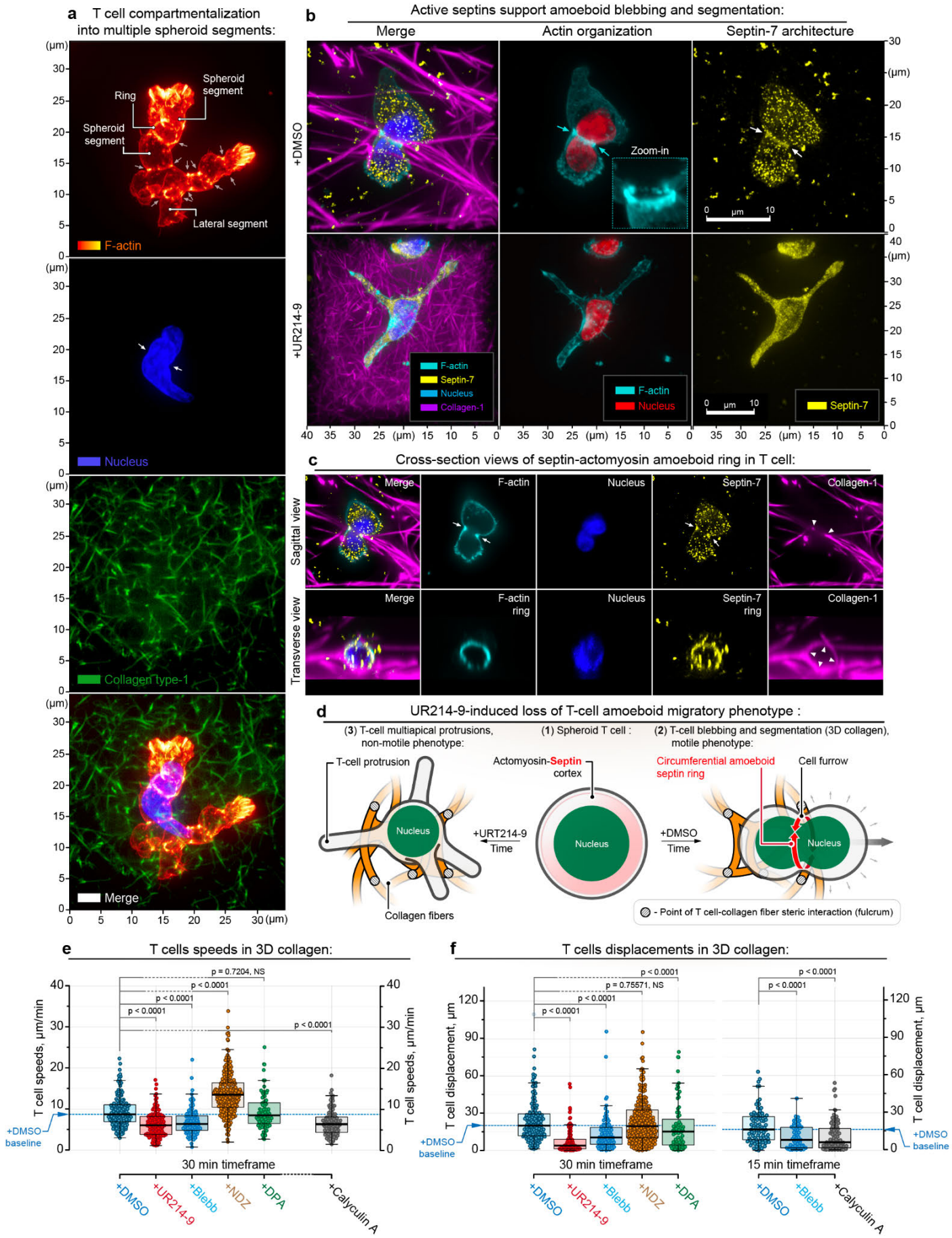
a T cell compartmentalization into multiple spheroid segments:
Ring
Spheroid segment
Spheroid segment
Lateral segment
F-actin
Nucleus
Collagen type-1
Merge
b Active septins support amoeboid blebbing and segmentation:
Merge
Actin organization
Septin-7 architecture
+DMSO
+UR214-9
Zoom-in
F-actin
Septin-7
Nucleus
Collagen-1
c Cross-section views of septin-actomyosin amoeboid ring in T cell:
Sagittal view
Transverse view
F-actin ring
Septin-7 ring
d UR214-9-induced loss of T-cell amoeboid migratory phenotype :
(3) T-cell multiapical protrusions, non-motile phenotype:
(1) Spheroid T cell :
(2) T-cell blebbing and segmentation (3D collagen), motile phenotype:
T-cell protrusion
Actomyosin-Septin cortex
Circumferential amoeboid septin ring
Cell furrow
Nucleus
+URT214-9
Time
+DMSO
Time
Collagen fibers
- Point of T cell-collagen fiber steric interaction (fulcrum)
e T cells speeds in 3D collagen:
T cell speeds, μm/min
+DMSO baseline
30 min timeframe
+DMSO
+UR214-9
+Blebb
+NDZ
+DPA
+Calyculin A
f T cells displacements in 3D collagen:
T cell displacement, μm
30 min timeframe
15 min timeframe

Figure 1. Septins mediate the T-cell cortex compartmentalization and amoeboid locomotion in 3D microenvironments.

(a) Human CD4+ T cell compartmentalization into the multiple spheroid segments within a collagen (type I) 3D matrix. Multiple spheroid segments are separated with F-actin-dense cortical rings (phalloidin F-actin channel, *arrows*) that deform and indent a passing-through nucleus (nucleus channel, *arrows*).

(b) *Top* - hCD4+ T cells in 3D collagen matrix in the control conditions **(+DMSO)** actively migrate, while maintaining the amoeboid segmentation with a septin-positive leading cortical ring (Septin-7 immunofluorescence and phalloidin imaging, *arrows*). The amoeboid T cell translocates its deformable nucleus through the cortical ring during migration. *Note that in control T cells septin-7 also enriches the cytosolic vesicular structures, as well as the vesicles outside of the cells (e.g. - microvesicles).*

Bottom - hCD4+ T cells in 3D collagen during septin inhibition **(+UR214-9)** do not develop septin-based cortical rings, leading to the loss of cortex compartmentalization and migrational behavior. Instead, T cells acquire an elongated non-migratory morphology with multiple protrusions. *Note that UR214-9 reduces septin-enriched cytosolic and extracellular microvesicles (as shown with septin-7 immunofluorescence).*

(c) Detailed transverse and sagittal cross-section views of the septin-enriched (septin-7 immunofluorescence) cortical rings in the migrating T cell (see **b**, *top*). *Note that the septin-F-actin cortical ring forms inside the confining collagen lumen (arrows).*

(d) Schematic views of spheroid T cell transition to the migratory, amoeboid cells in the sterically complex microenvironments, as well as T cell's structural response to septin chemical suppression with UR214-9.

(e) Human CD4+ T cell migration speeds within 3D collagen matrix during perturbation of the key cytoskeletal subsystems: septins **(+UR214-9)**, microtubules **(+Nocodazole**, *i.e.* +NDZ**)**, non-muscle myosin contractility **(+Blebbistatin**, *i.e.* +Blebb, and **+Calyculin A)**, and dynein contractility **(+Dynapyrazole A**, *i.e.* +DPA**)**. *Note that automatically measured T cell speed mean values do not reach zero due to the lack of sufficient T cells-collagen adhesion. Insufficient adhesion enables lymphocytes' passive oscillations (e.g. Brownian movement) within 3D collagen matrix, to include completely arrested T cells (e.g.* ***+UR214-9*** *or* ***+Calyculin A*** *treatments). Passive T cell oscillations do not result in lymphocyte's displacement within the collagen matrix, see* ***(f)****.*

(f) Human CD4+ T cell migratory displacement in 3D collagen matrix within a 30 and 15 minute-long timeframe during perturbation of the key cytoskeletal subsystems. *Note that both* ***+UR214-9*** *and* ***+Calyculin A*** *treatments induce most complete T cell displacement arrests, due to complete loss of amoeboid cortical dynamics.*

a T cell compartmentalization into the multiple spheroid chambers displays differential phospho-myosin distribution between segments:

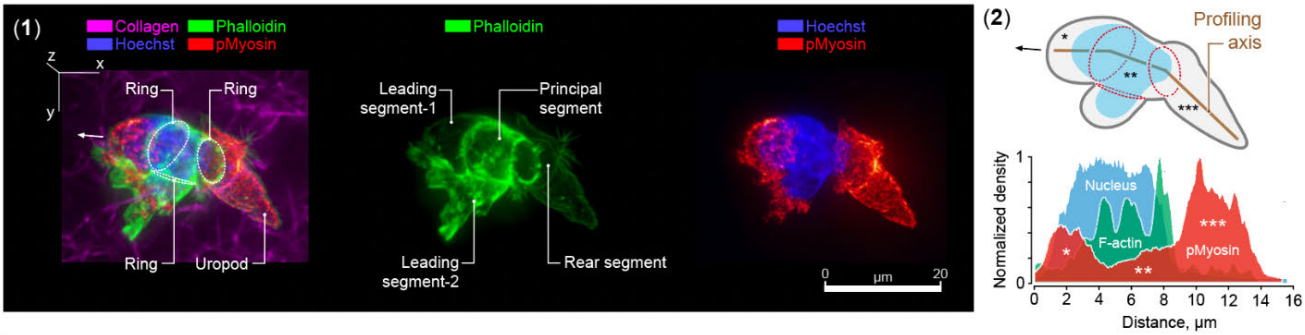

b Rings-ECM link :

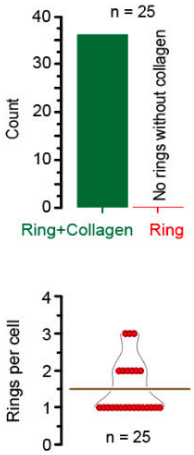

c Discrete peristaltic T cell migration within 3D collagen matrix :

Timecourse captures of T cell along its motility trajectory:

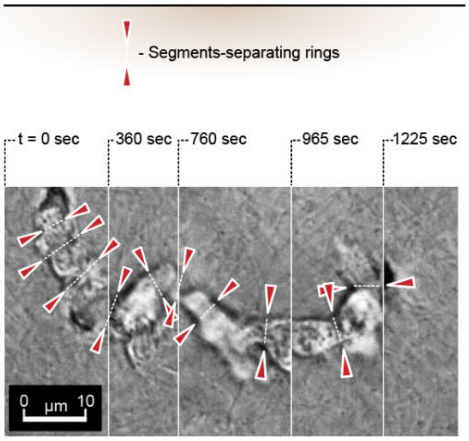

Schematic of theT cell migration track as a result of the discrete peristaltic:

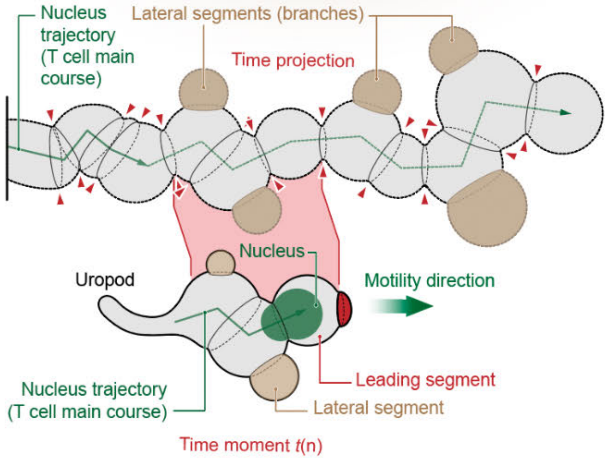

d Cortex septin rings enable T-cell navigation within complex 3D environments:

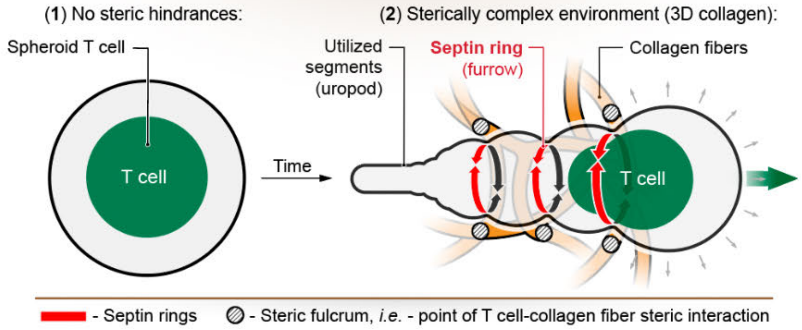

e Ring formation in response to collagen crowding:

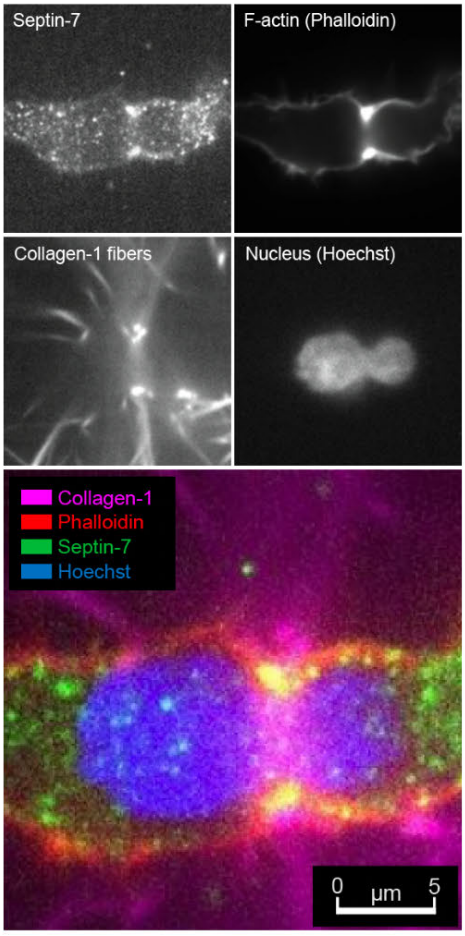

f Discrete peristaltic treadmilling of T cell *via* series of new compartment formation :

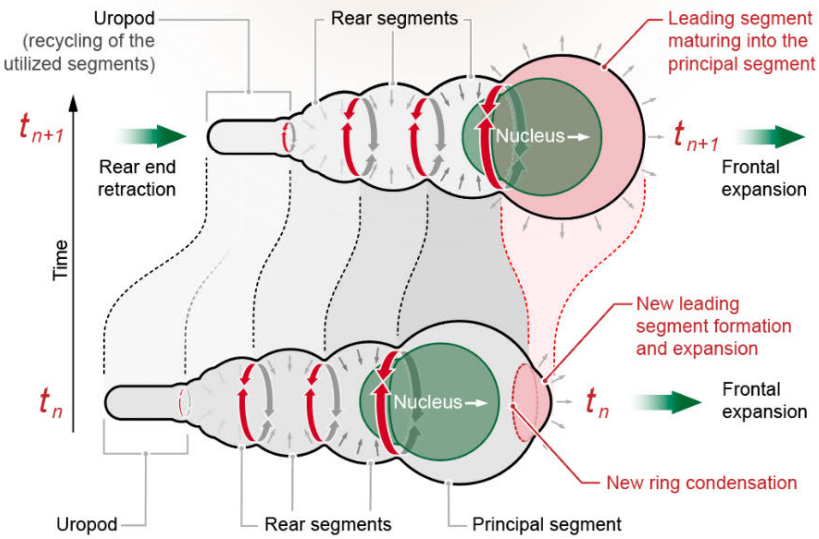

Figure 2. Compartmentalization of the actomyosin cortex into peristaltic segments by septin-actin cortical rings drives lymphocytes' amoeboid locomotion within the 3D collagen matrix .

(a) (**1**) - 3D micrographic view of the hCD4+ T cell **(+DMSO)** in the collagen matrix forming multiple rings and segments. Note that the cortex in adjacent segments displays a differential density of phospho-myosin (phospho myosin light chain 2 (Ser19)), indicating that each segment features an individual, different cortical contractility. (**2**) - Phospho-myosin, F-actin and chromatin 3D cumulative density profiling along the T cell's main axis, *i.e.* - across the principal segments. Note that phospho-myosin peaks in the leading and the rear segments, but is depleted in the main, nucleus-containing segment.

(b) *Top* - Cortical rings are linked to the presence of a cell-surface indenting ECM (collagen) fiber. Rings are always associated with the adjacent collagen fiber (ring+collagen), while there is no T cell ring identified without a presence of the collagen fiber. *Bottom* - Distribution of the rings per cell counts (mean value ~1.5 ring/cell).

(c) (*Left*) - Time course captures of the single hCD4+ T cell along its migration track within the 3D collagen matrix. Note the T cell forms multiple segments (chambers), separated by the rings (arrowheads) along the track of its migration. The T cell trajectory is a zigzag track between the chambers that are formed during the migration. (*Right*) - Schematic representation of the spatiotemporal superposition of the migrating T cell - motility is driven by peristaltic translocation of the nucleus between segments, separated by the cortical rings (highlighted by arrowheads). Nucleus translocation forms the main zigzag track that reflects the directionality of the new leading segment formation, guided by the surrounding microenvironment steric configuration and topography. *Note that T cells also develop side branching pseudopods (lateral segments) that do not accommodate the nucleus and therefore do not become the leading segments.*

(d) Schematic representation of the multi-chambered amoeboid T cell within the sterically interactive collagen matrix.

(e) Sagittal cross-section views of the T cell migrating through the collagen matrix. Note the septin-positive (septin-7) cortical ring forms at the sites of the T-cell mechanical (cell surface-indenting) interaction (crowding) with the collagen fibers. The formation of the cortical ring allows the T cell to compartmentalize into the multiple chambers aligned into the cylindrically shaped tube that peristaltically translocates the cytoplasm and nucleus between the segments. Note that the nucleus conforms to the surrounding cortical ring.

(f) Schematic representation of T cell peristaltic treadmilling as s series of the new compartments formation at the leading front of the cell, accompanied by the nucleus and cytosol translocation **(Movies 1, 2 and 3)**.

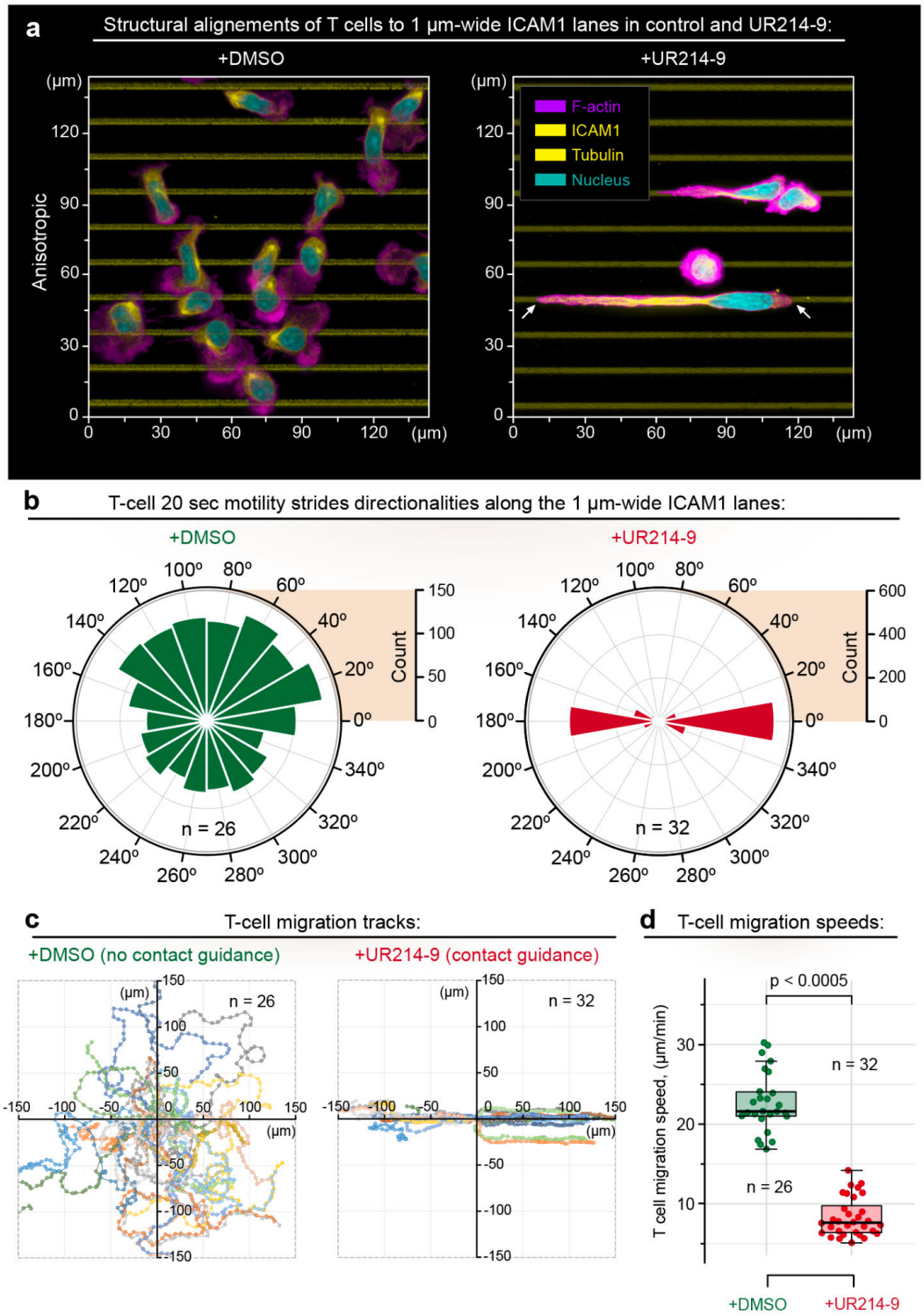

Figure 3. Septins inactivation induces amoeboid-to-mesenchymal-like phenotypic transition with a slow non-amoeboid motility and mesenchymal-like contact guidance.

(a) hCD4+ T cells during control vehicle treatment **(+DMSO)** maintain predominantly amoeboid-like non-spreading phenotype, featuring neither spreading nor alignment along the T cell adhesion cues (ICAM1 anisotropic parallel lines, see **Movies 4 and 5 (before UR214-9)**). Septin inhibition **(+UR214-9)** induces T cells phenotype transitioning towards mesenchymal-like behavior, resulting in the prominent lymphocytes adhesion, strong alignment and excessive spreading along the ICAM1 lines **(Movies 4 and 5 (after UR214-9), Movie 6)**. Comparative analysis of T cells migratory dynamics between control **(+DMSO)** and septin-inhibition **(+UR214-9)** conditions for **(b)** T cell migration directionality, **(c)** individual T cell migration tracks, and **(d)** migration speeds indicates that septins inhibition leads to

the transition of T cell migration phenotype towards extreme, mesenchymal-like migration and alignment to the contact guidance cues, *i.e.* high fidelity of the T cell migration tracks to the ICAM1 lines architecture, accompanied with the significant loss of T cell migration speed, inherent to the mesenchymal migratory dynamics.

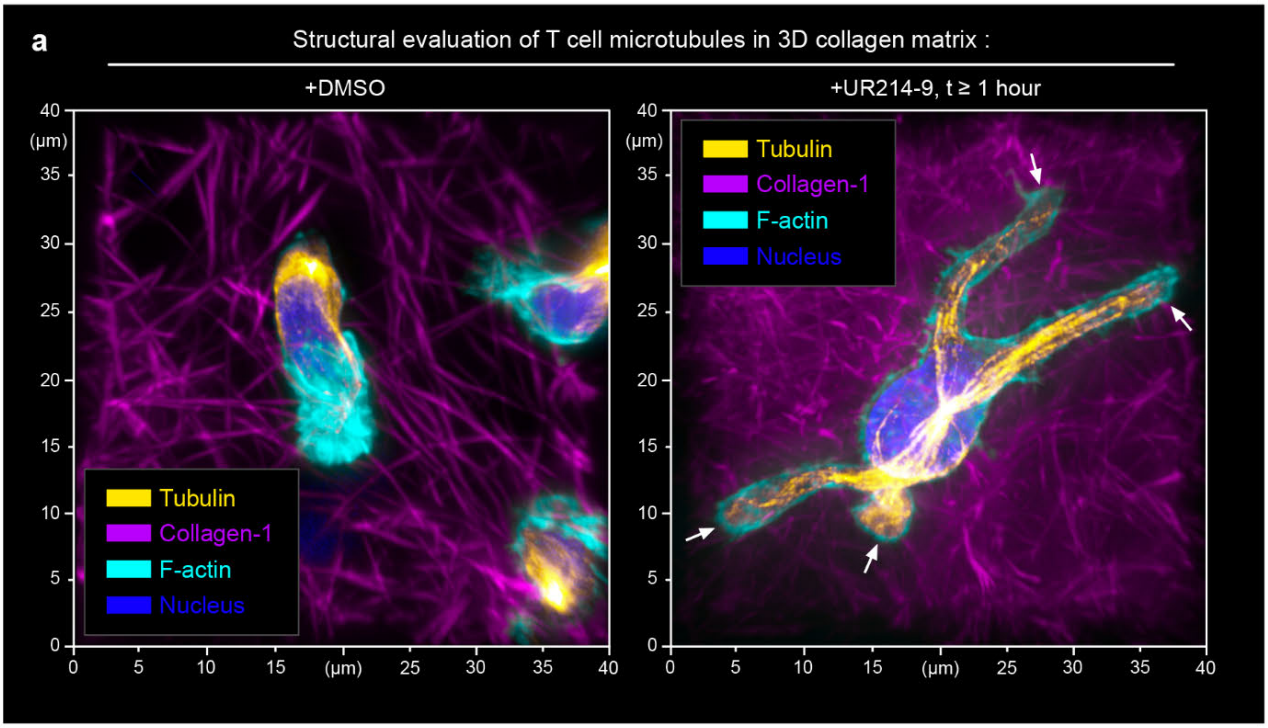
a
Structural evaluation of T cell microtubules in 3D collagen matrix :
+DMSO
+UR214-9, t ≥ 1 hour
(μm)
Tubulin
Collagen-1
F-actin
Nucleus

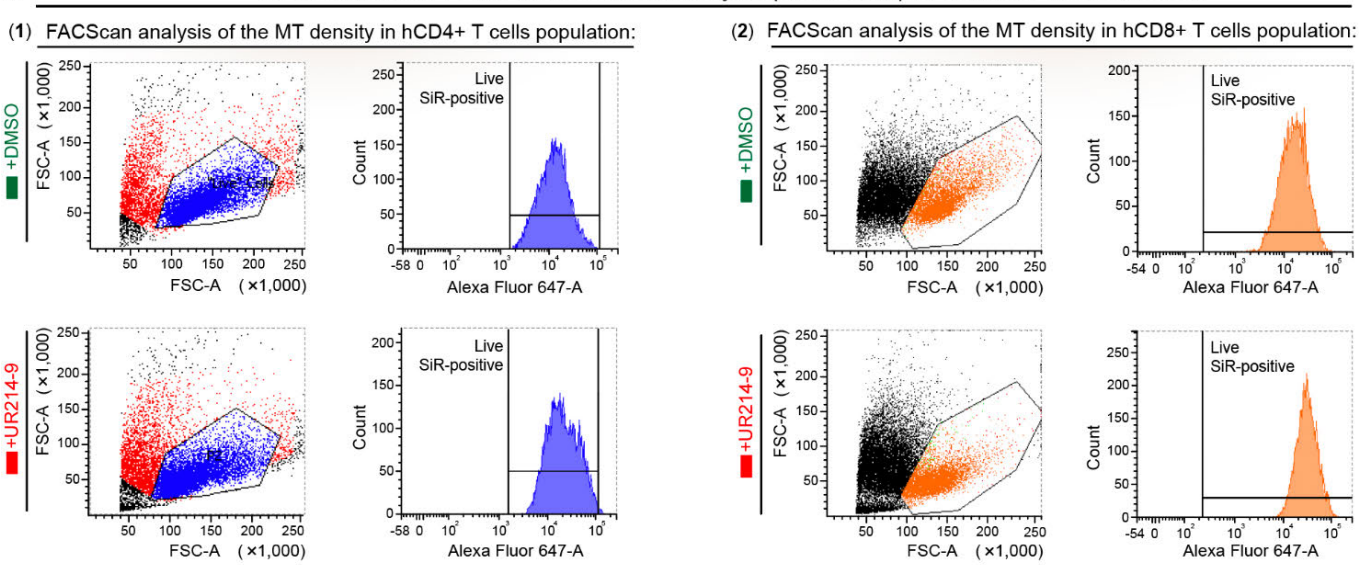
b
Measurement of T cells microtubules density response to septin inhibition with UR214-9 :
(1) FACScan analysis of the MT density in hCD4+ T cells population:
(2) FACScan analysis of the MT density in hCD8+ T cells population:
+DMSO
+UR214-9
FSC-A (×1,000)
Live
SiR-positive
Count
Alexa Fluor 647-A

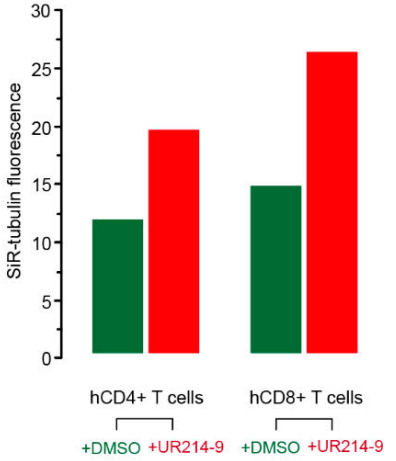
c
UR214-9 increases MT density:
SiR-tubulin fluorescence
hCD4+ T cells
hCD8+ T cells
+DMSO
+UR214-9

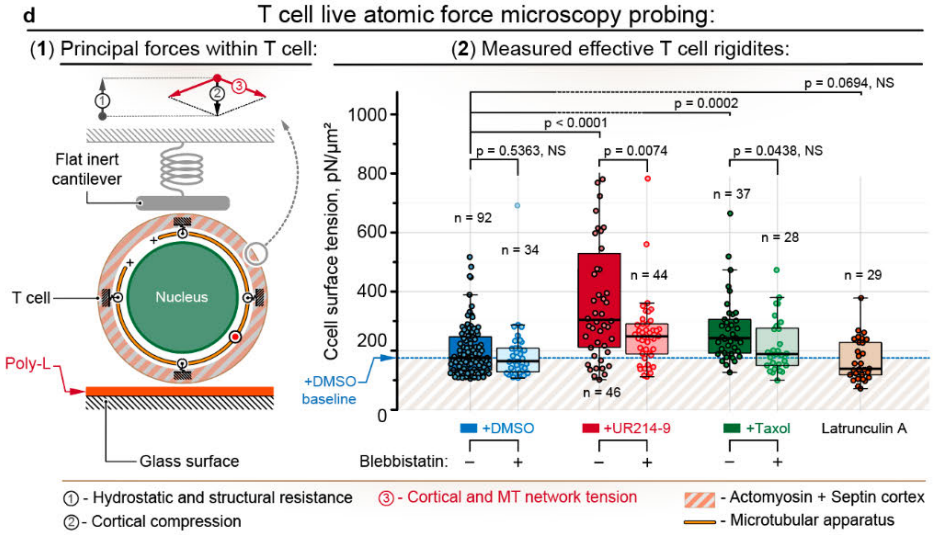
d
T cell live atomic force microscopy probing:
(1) Principal forces within T cell:
(2) Measured effective T cell rigidites:
Flat inert cantilever
T cell
Nucleus
Poly-L
Glass surface
Ccell surface tension, pN/μm²
p = 0.0694, NS
p = 0.0002
p < 0.0001
p = 0.5363, NS
p = 0.0074
p = 0.0438, NS
n = 92
n = 34
n = 46
n = 44
n = 37
n = 28
n = 29
+DMSO baseline
+DMSO
+UR214-9
+Taxol
Latrunculin A
Blebbistatin:
① - Hydrostatic and structural resistance
② - Cortical compression
③ - Cortical and MT network tension
- Actomyosin + Septin cortex
- Microtubular apparatus

Figure 4. Septins inhibition increases the structural density of microtubular apparatus and mechanical rigidity of T cells.

(a) Structural densification and elongation of microtubules (*arrows*) during septins inhibition **(+UR214-9**, t≥1 hour**)** in hCD4+ T cell within a 3D collagen matrix.

(b) FACScan flow cytometry analysis of the (**1**) hCD4+ and (**2**) hCD8+ T cells's microtubular apparatus density (*per cell*) as measured by the polymerized MT-specific SiR-tubulin live fluorescence (used as per commercial protocol, 1 hour incubation time).

(c) Population-wide mean values of MT density in hCD4+ and hCD8+ T cells during septin inhibition **(+UR214-9**, t≥1 hour**)** display 60% (hCD4+) and +90% (hCD8+) more of the MT filaments per cell in comparison to the control T cells **(+DMSO)**.

(d) Human CD4+ T cell live atomic force microscopy probing identifies T cell rigidification upon the microtubular apparatus build-up, induced by UR214-9-mediated septin inhibition. (**1**) - Schematic representation of the experimental settings and basic forces configurations for live T cell mechanical probing. (**2**) - Measured T cell mechanical rigidities as the effective cell surface tension. Both UR214-9- and Taxol-induced microtubular stabilization result in T cell rigidification.

*Note that suppression of actomyosin contractility with Blebbistatin co-treatment during **+UR214-9** or **+Taxol** treatments does not soften T cell down to the baseline level **(+DMSO)**, indicating the T cell rigidification is a combined effect of the cortical contractility and passive mechanical resistance of the enhanced microtubule apparatus. Note also that blebbistatin co-treatments do not result in the statistically significant T cell softening within all ±Blebbistatin co-treatment pairs (i.e. **±Blebbistatin**, **+UR214-9±Blebbistatin**, and **+Taxol±Blebbistatin**) due to the presence of the relatively large, mechanically resistant nuclei (~60-70% of T cell volume), and dense microtubules (**+UR214-9** and **+Taxol** treatments). Similarly, pharmacologically-induced disintegration of the F-actin network **(+Latrunculin A)** shows no statistically significant T cell softening due to the presence of the underlying nucleus.*

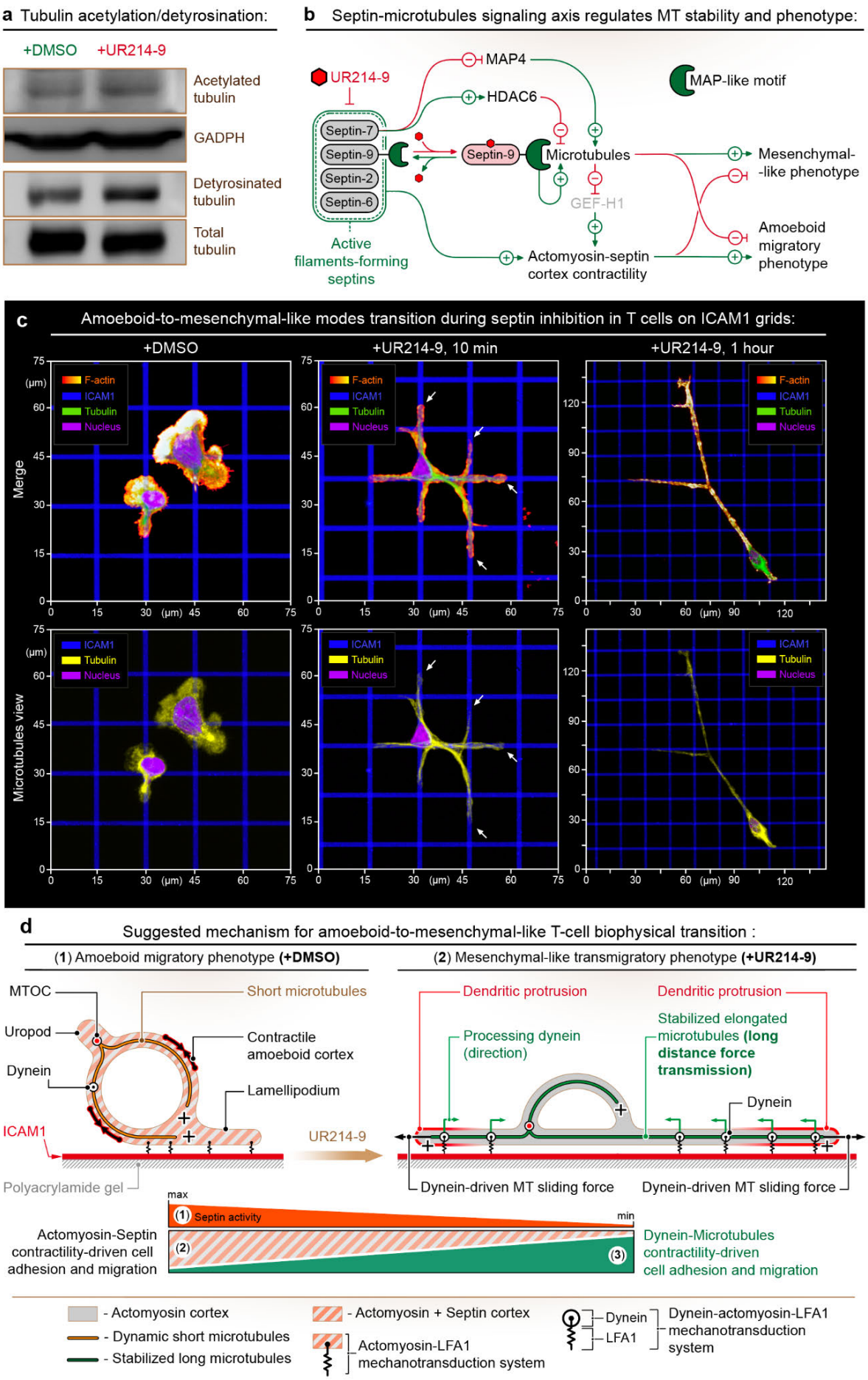
a Tubulin acetylation/detyrosination:
+DMSO
+UR214-9
Acetylated tubulin
GADPH
Detyrosinated tubulin
Total tubulin
b Septin-microtubules signaling axis regulates MT stability and phenotype:
UR214-9
MAP4
HDAC6
MAP-like motif
Septin-7
Septin-9
Septin-2
Septin-6
Septin-9
Microtubules
GEF-H1
Mesenchymal--like phenotype
Amoeboid migratory phenotype
Active filaments-forming septins
Actomyosin-septin cortex contractility
c Amoeboid-to-mesenchymal-like modes transition during septin inhibition in T cells on ICAM1 grids:
+DMSO
+UR214-9, 10 min
+UR214-9, 1 hour
F-actin
ICAM1
Tubulin
Nucleus
Merge
Microtubules view
(μm)
d Suggested mechanism for amoeboid-to-mesenchymal-like T-cell biophysical transition :
(1) Amoeboid migratory phenotype (+DMSO)
(2) Mesenchymal-like transmigratory phenotype (+UR214-9)
MTOC
Uropod
Dynein
ICAM1
Short microtubules
Contractile amoeboid cortex
Lamellipodium
Polyacrylamide gel
UR214-9
Dendritic protrusion
Dendritic protrusion
Processing dynein (direction)
Stabilized elongated microtubules (long distance force transmission)
Dynein
Dynein-driven MT sliding force
Dynein-driven MT sliding force
max
min
(1) Septin activity
(2)
(3)
Actomyosin-Septin contractility-driven cell adhesion and migration
Dynein-Microtubules contractility-driven cell adhesion and migration
- Actomyosin cortex
- Dynamic short microtubules
- Stabilized long microtubules
- Actomyosin + Septin cortex
Actomyosin-LFA1 mechanotransduction system
Dynein
LFA1
Dynein-actomyosin-LFA1 mechanotransduction system

Figure 5. T cells undergoing amoeboid-to-mesenchymal-like phenotype transition form multiple dendritic microtubules-rich protrusion and demonstrate aligned spreading along the ICAM1 contact guidance cues.

(a) Western blot analysis of tubulin acetylation and detyrosination displays a ~20% and ~25-40% increase, respectively of the post-translationally modified tubulin in hCD4+ T cells after the **+UR214-9** treatment.

(b) Signaling contours linking septins' activity, microtubules and actomyosin cytoskeleton behaviors, and the T cell phenotype transition between amoeboid and mesenchymal-like phenotypes. *Note that during UR214-9-induced septins' GTPase activity suppression, and septin filaments disassembly, the released and SEPT9_i1 (septin-9) acts as a MAP-like protein.*

(c) *Top* - Amoeboid hCD4+ T cells on ICAM1 grid in control conditions **(+DMSO)** display no alignment response to the underlying ICAM1 contact guidance cues (grids), **Movie 7**. Early effects of septin inhibition **(+UR214-9**, 10 min**)** display hCD4+ reorganization into the dendritic cell architecture spreading along the ICAM1 grid contact guidance cues (*arrows*), **Movie 8**. Prolonged septin suppression **(+UR214-9**, 1 hour**)** leads to an extreme T cell spreading along the ICAM1 grid, resulting with lymphocyte's dendritization and multi-apical protrusions elongation along the ICAM1 grid.

Bottom - Immunofluorescent visualization of the microtubular apparatus in the amoeboid **(+DMSO)** and mesenchymal-like **(+UR214-9)** T cells reveals the higher density and length of the microtubular apparatus during UR214-9 treatment.

(d) Schematic representation of the suggested mechanism for T cell phenotypic transition from the amoeboid **(+DMSO)** towards mesenchymal-like **(+UR214-9)** state.

a T-cell transmigration requires amoeboid-mesenchymal transition, cortex deformability and long-distance force transmission:

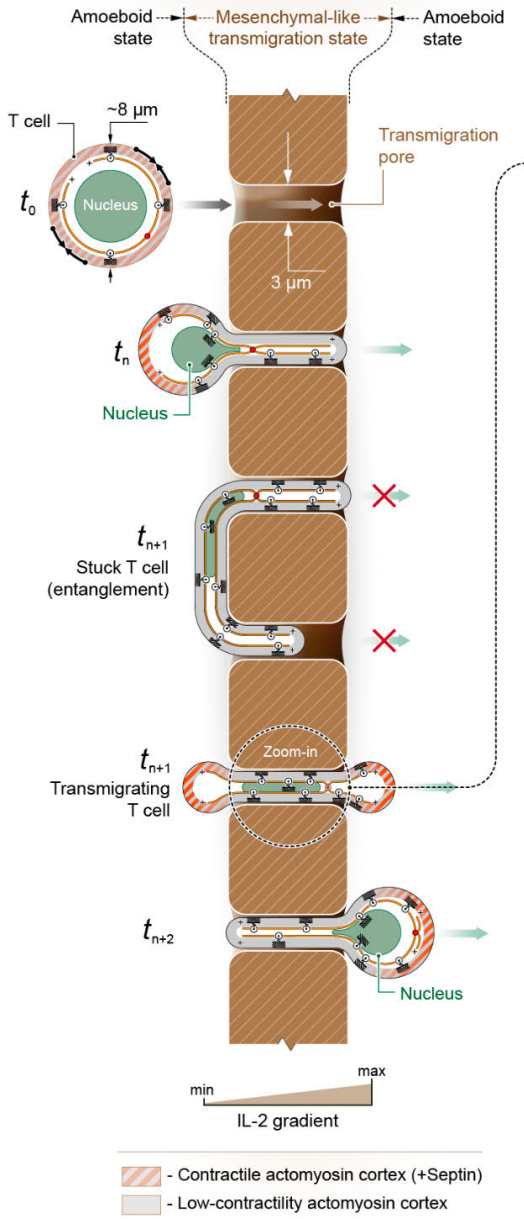

b Suggested force transmission mechanism for transmigrating T cell *via* microtubules :

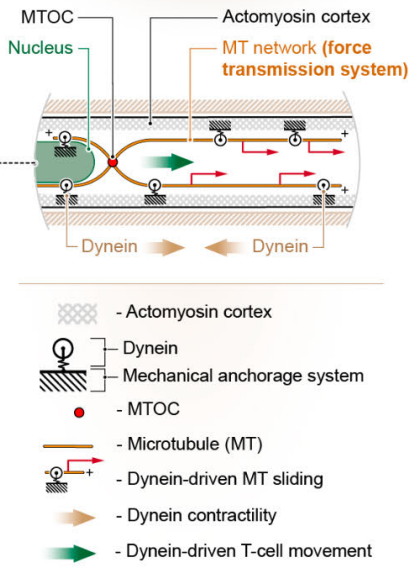

c Principal forces configuration within migrating and transmigrating T cell :

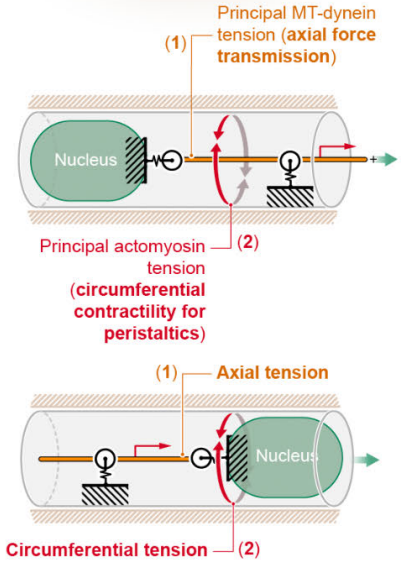

d Perturbation of the key subsystems of T cell transmigration machinery :

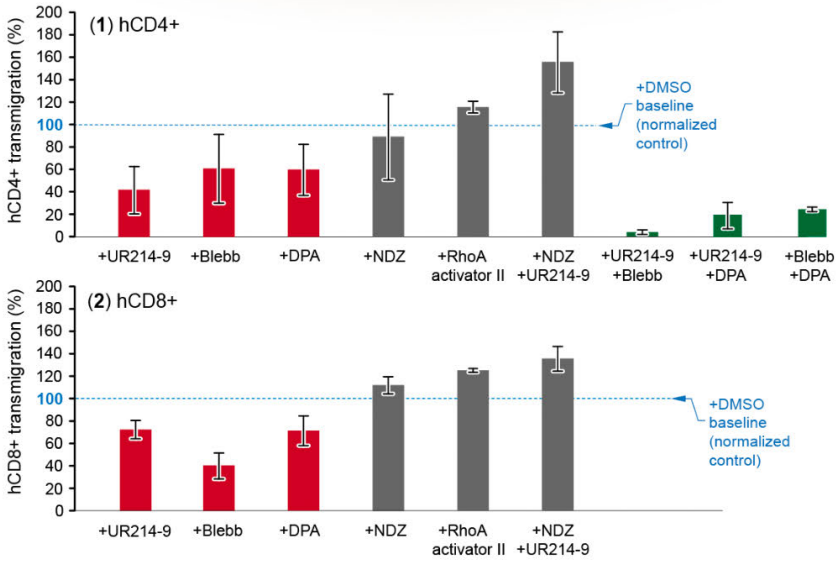

e Entangled transmigrating T cells, 3D micrography:

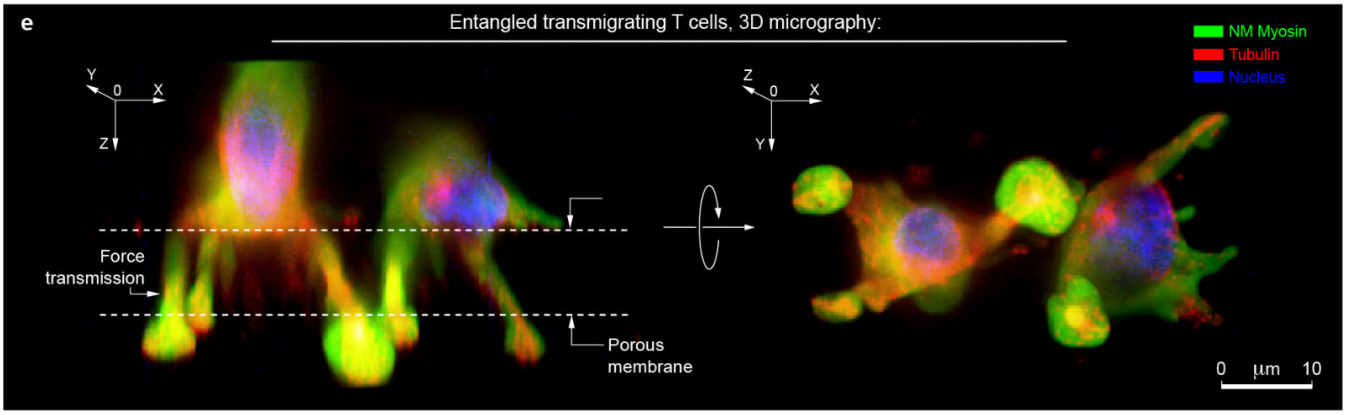

Figure 6. Model of the T cell transmigration mechanism *via* combined septin-dependent amoeboid and dynein-microtubules-dependent mesenchymal-like motilities.

(a) For entering and transmigration through narrow 3 μm pore the amoeboid T cell must transition into the confinement-induced narrowing and elongation. In order to prevent cell overstretching and rupture, and to power structurally and mechanically coherent cell body's passage through the pore the transmigrating T cell requires an efficient force transmission along the confined cell body axis. Described transmission system is presented by the dyneins generating the contractile forces within the non-stretchable microtubular cables along the elongated axis of the transmigrating T cell. Cortex-bound dynein motors mechanically pull the microtubules, forming a singular mechanical system that facilitates the mechanically and structurally coherent passage of the nucleus and rear parts of the cortex. Microtubular cables may also hinder T cell transmigration *via* the lymphocyte's structural entanglement between several alternative pores. As a T cell enters multiple pores, non-stretchable microtubular cables prevent T cells from ruptures, while distributing pulling forces between several in-pore T cell protrusions, capturing T cells in an entangled 'tug-of-war' state, 'stuck' between several pores.

(b) A detailed schematic of the transmigrating segment of the T cells, depicting a simplified mechanical system of transmigration-driving force transmission: confining pore, actomyosin cortex, microtubules, dynein motors and nucleus.

(c) Principal forces within migrating and transmigrating T cell: (**1**) dynein-generated axial forces, transmitted at long distances through microtubular cables, and (**2**) actomyosin cortex-generated circumferential tension, structured into the multiple constriction rings by septins. Actomyosin circumferential forces predominantly facilitate T cell peristaltic dynamics for the amoeboid propulsion, while dynein-microtubule system-mediated axial forces facilitate a mechanically coherent T cell passage through the confining spaces. The model is equally applicable to the transmigrating T cells that locomote the nucleus as a frontal 'piston', or pull the nucleus at the rear portion of the transmigrating cell.

(d) Normalized hCD4+ and hCD8+ T cell transmigration efficiency during perturbation of the key cytoskeletal subsystems. Inhibition of either septins as the principal amoeboid dynamics protein **(+UR214-9)**, or suppression of the actomyosin tension as the driving mechanical force for amoeboid dynamics **(+Blebbistatin)** diminishes both hCD4+ and hCD8+ T cells transmigration. Similarly, dynein contractility suppression **(+Dynapyrazole A, DPA)** reduces hCD4+ and hCD8+ T cells transmigration. Disassembly of the microtubules **(+Nocodazole, NDZ)** does not conclusively change T cell transmigration efficiency, as microtubules destabilization causes multiple effects - increase of actomyosin contractility *via* MT-GEF-H1 signaling axis, and arrest of MT-dependent dynein-generated axial forces, the opposite effects that mutually compensate for each other. A sole increase of the actomyosin tension *via* a selective RhoA activation **(+RhoA activator II)** displays an increase of both hCD4+ and hCD8+ T cells transmigration. Inhibition of amoeboid phenotype proteins (septin), combined with the suppression of either actomyosin **(+UR214-9+Blebbistatin)** or dynein **(+UR214-9+Dynapyrazole A)** contractilities almost completely abrogates hCD4+ T cells transmigration, indicating that non-amoeboid T cells require both contractility systems for transmigration. Similarly, inhibition of both dynein- and myosin-generated contractilities **(+Blebbistatin+Dynapyrazole A)** suppresses T cell transmigration.

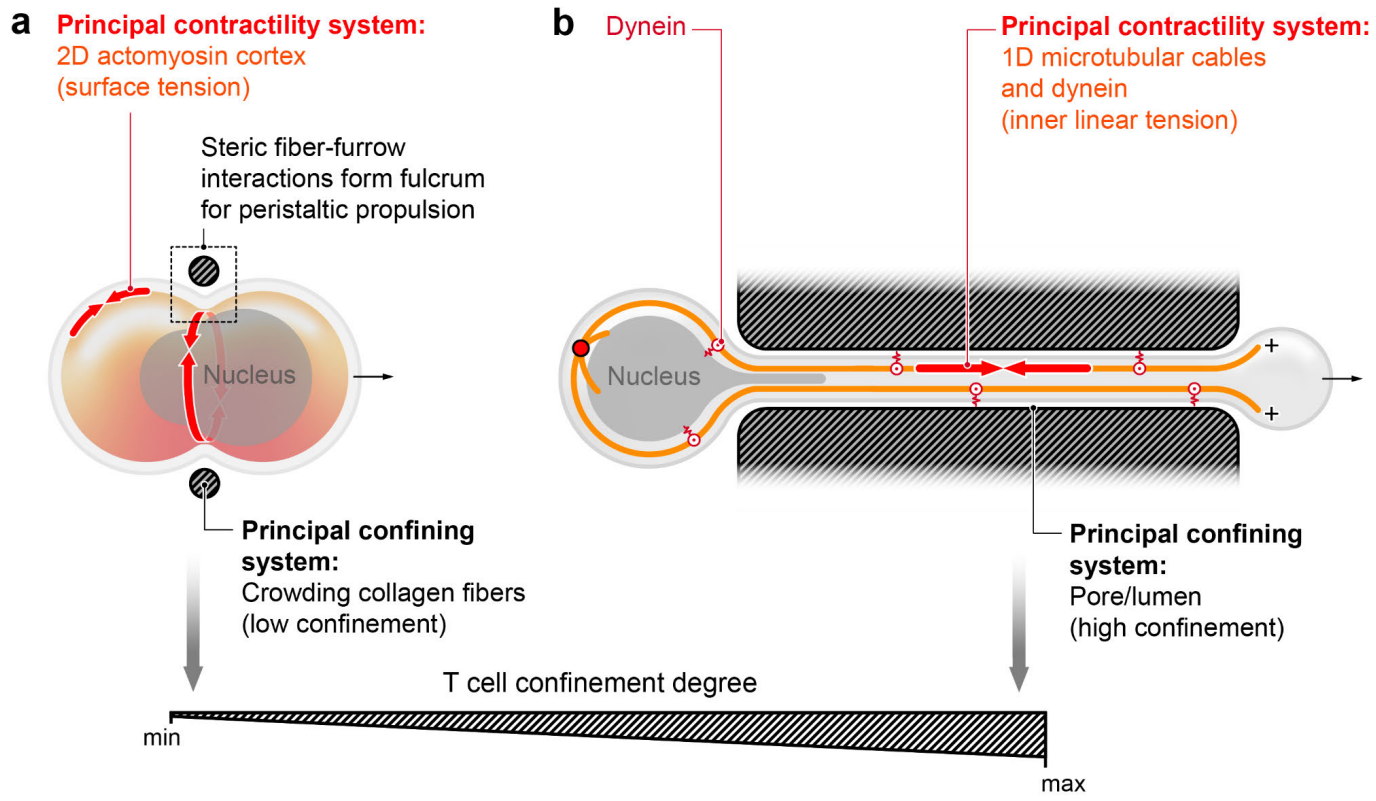

Figure 7. Summarizing model of the T cell migration and transmigration mechanism in various confinement environments.

(a) Septin-structured amoeboid cortical peristaltic contractility mechanically channels T cell migration between collagen fibers in low confinement conditions.

(b) T cell mesenchymal-like transmigration through highly confining spaces (pore) is driven by the dynein-generated mechanical forces, transmitted *via* the microtubular cables along the principal T cell axis.

SUPPLEMENTARY FIGURES

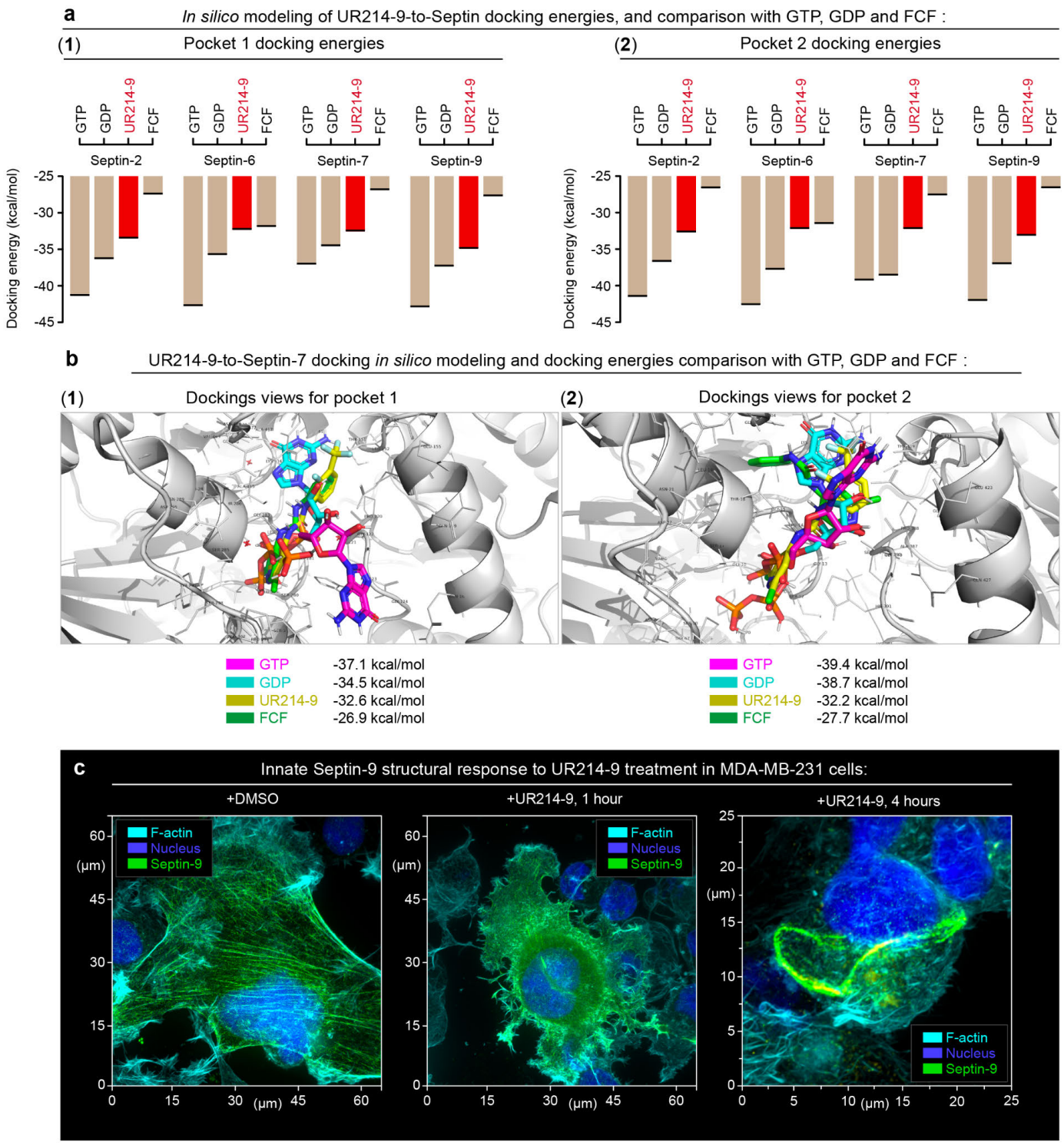

Supplemental figure SI1. *In silico* molecular docking simulations for the key filaments-related septin isoforms displays a competitive UR214-9-septins interactions energies in comparison to GTP, GDP and FCF

(a) *In silico*-computationally derived energies of GTP, GDP, UR214-9, and FCF docking to pocket-1 and -2 of Septin-7 isoform. Note, that UR214-9-septin docking energy is more optimal, than that of FCF across all key filaments-related septin isoforms.

(b) *In silico*-simulated 3D models of molecular docking of GTP, GFP, UR214-9 and FCF to the septin-7's pockets 1 and 2.

(c) Innate septin filaments respond to the UR214-9 treatment in MDA-MB-231 cells, as shown by Septin-9. Superresolution imaging of the MDA-MB-231 cells, spread on a glass surface (fibronectin) forming the stress-fibers (phalloidin) and septin filaments (Septin-9, IF) as a single cytoskeletal network **(+DMSO)**. Cells treatment with low molecular mammalian septins inhibitor UR214-9 results in the dissociation of the actin-septin filaments network and retraction of cell adhesion **(+UR214-9,** 1 hour**)**, progressing into a complete loss of cell spreading and MT reorganization into a giant ring **(+UR214-9,** 4 hours**)**.

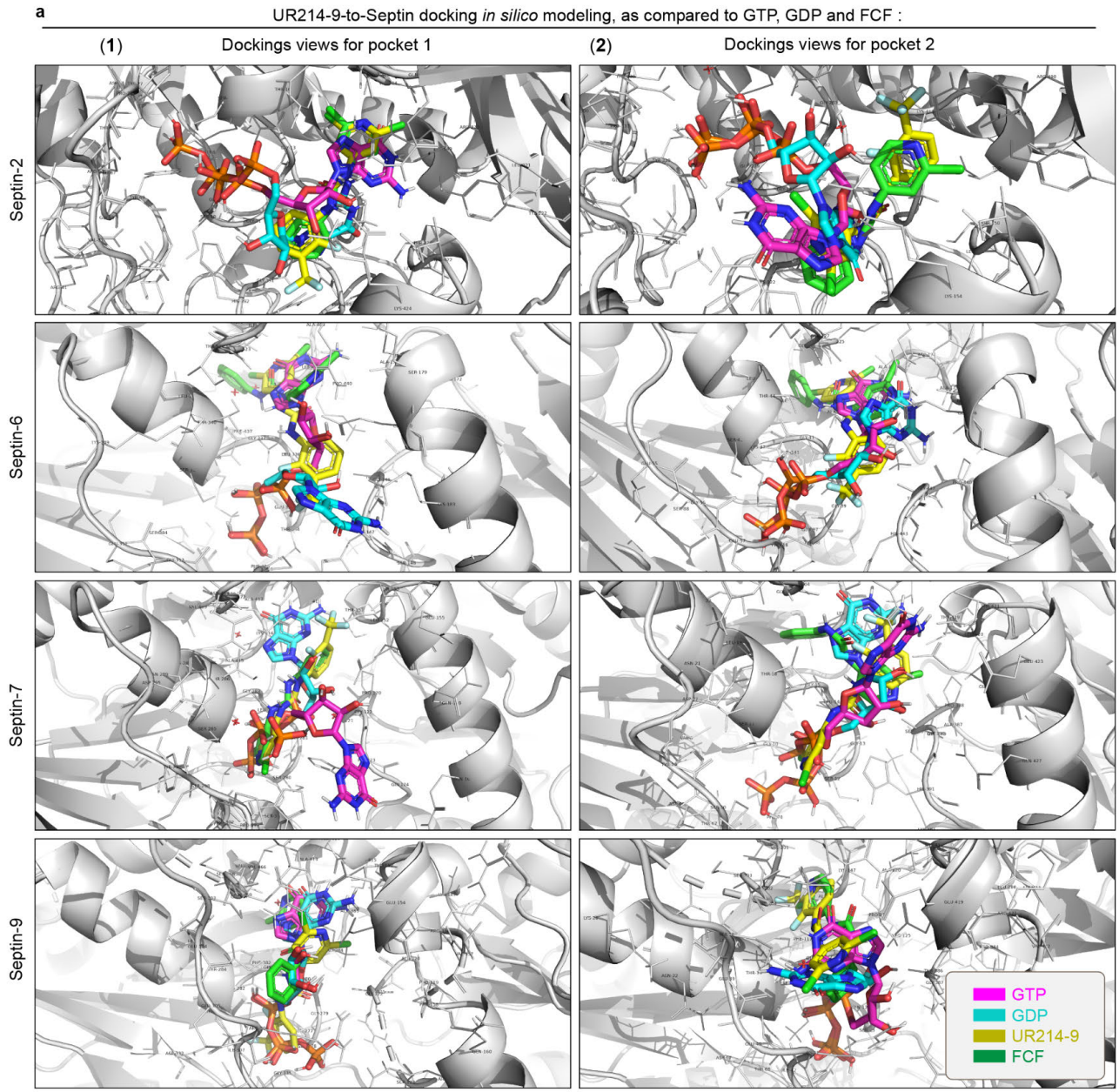

b UR214-9-to-Septin docking energy *in silico* modeling, as compared to GTP, GDP and FCF :

(**1**) Table 1

Ligand	Energy of interactions, pocket 1 (kcal/mol): Septin-2	Septin-6	Septin-7	Septin-9
GTP	-41.4013	-42.7594	-37.1021	-42.9431
GDP	-36.3165	-35.7889	-34.5495	-37.3714
UR214-9	-33.4929	-32.3030	-32.5959	-34.9654
FCF	-27.4643	-31.9061	-26.8665	-27.6648

(**2**) Table 2

Ligand	Energy of interactions, pocket 2 (kcal/mol): Septin-2	Septin-6	Septin-7	Septin-9
GTP	-41.5791	-42.7328	-39.3803	-42.1438
GDP	-36.7661	-37.8403	-38.6942	-37.0604
UR214-9	-32.6248	-32.2466	-32.2272	-33.0542
FCF	-26.6455	-31.5510	-27.6554	-26.6600

Supplemental figure SI2. UR214-9-septin *in silico* docking simulations display competitive energies of interactions as compared to FCF, GTP and GDP.

(a) *In silico* computational model for UR214-9 docking to septin-2, -6, -7 and -9's GTPase site at the respective pockets 1 and 2 in septin molecules, as compared to FCF inhibitor and GTP.

(b) *In silico*-calculated docking energies for GTP, GDP, UR214-9 and FCF.

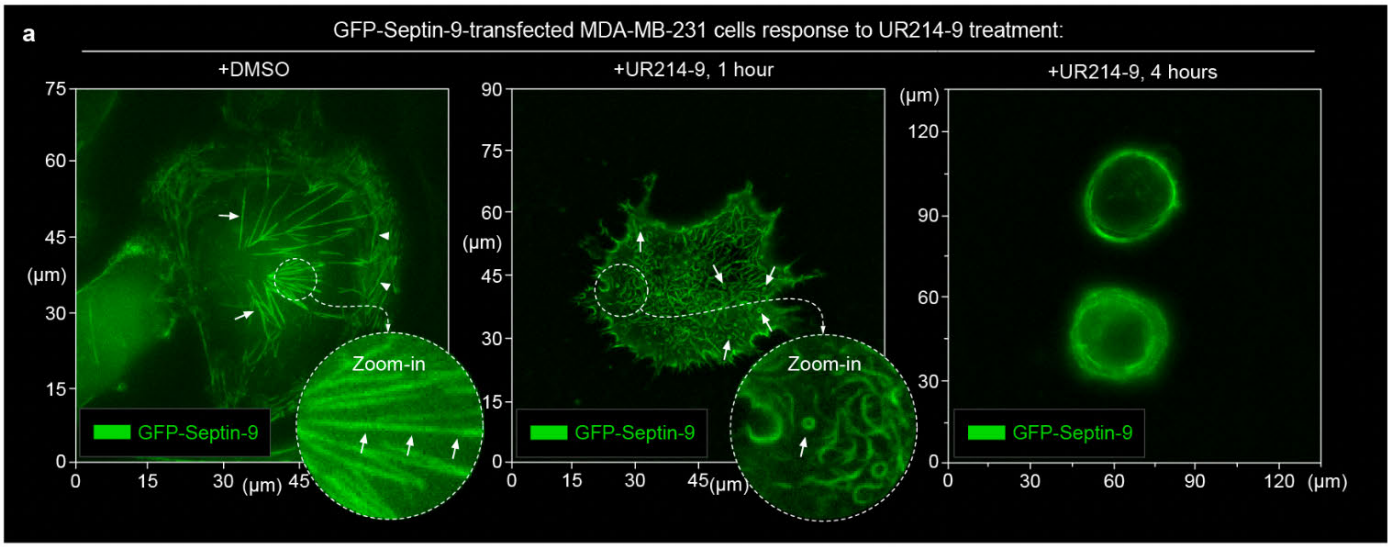
a
GFP-Septin-9-transfected MDA-MB-231 cells response to UR214-9 treatment:
+DMSO
+UR214-9, 1 hour
+UR214-9, 4 hours
Zoom-in
GFP-Septin-9
(µm)

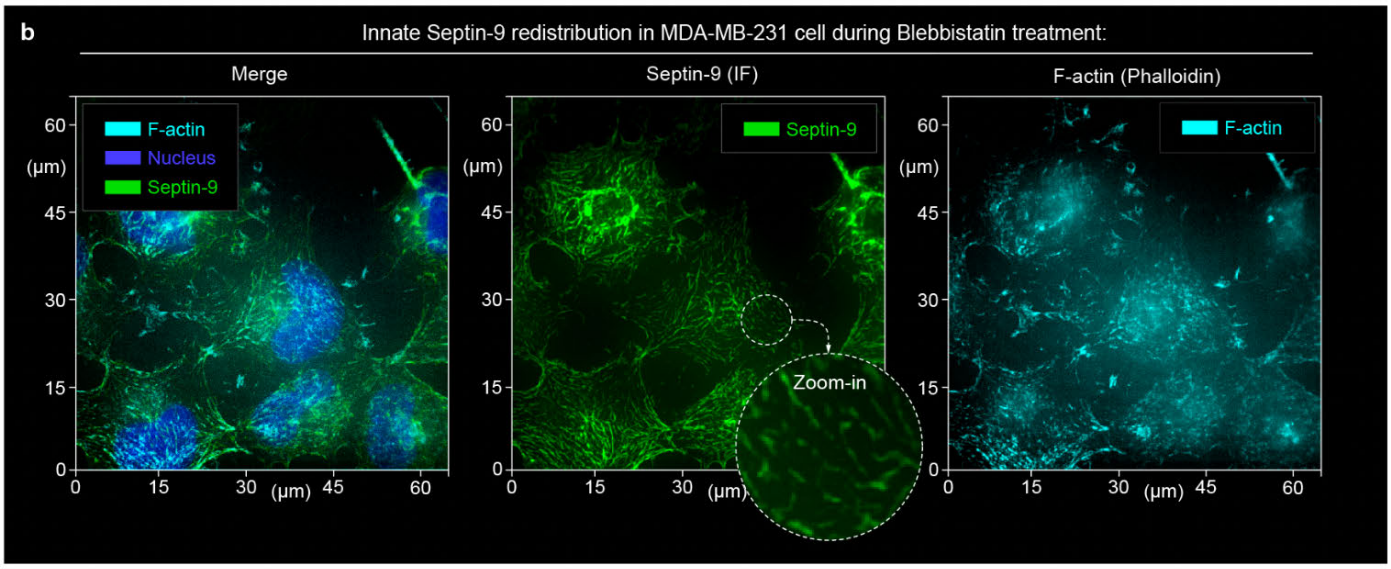
b
Innate Septin-9 redistribution in MDA-MB-231 cell during Blebbistatin treatment:
Merge
Septin-9 (IF)
F-actin (Phalloidin)
F-actin
Nucleus
Septin-9
Zoom-in
(µm)

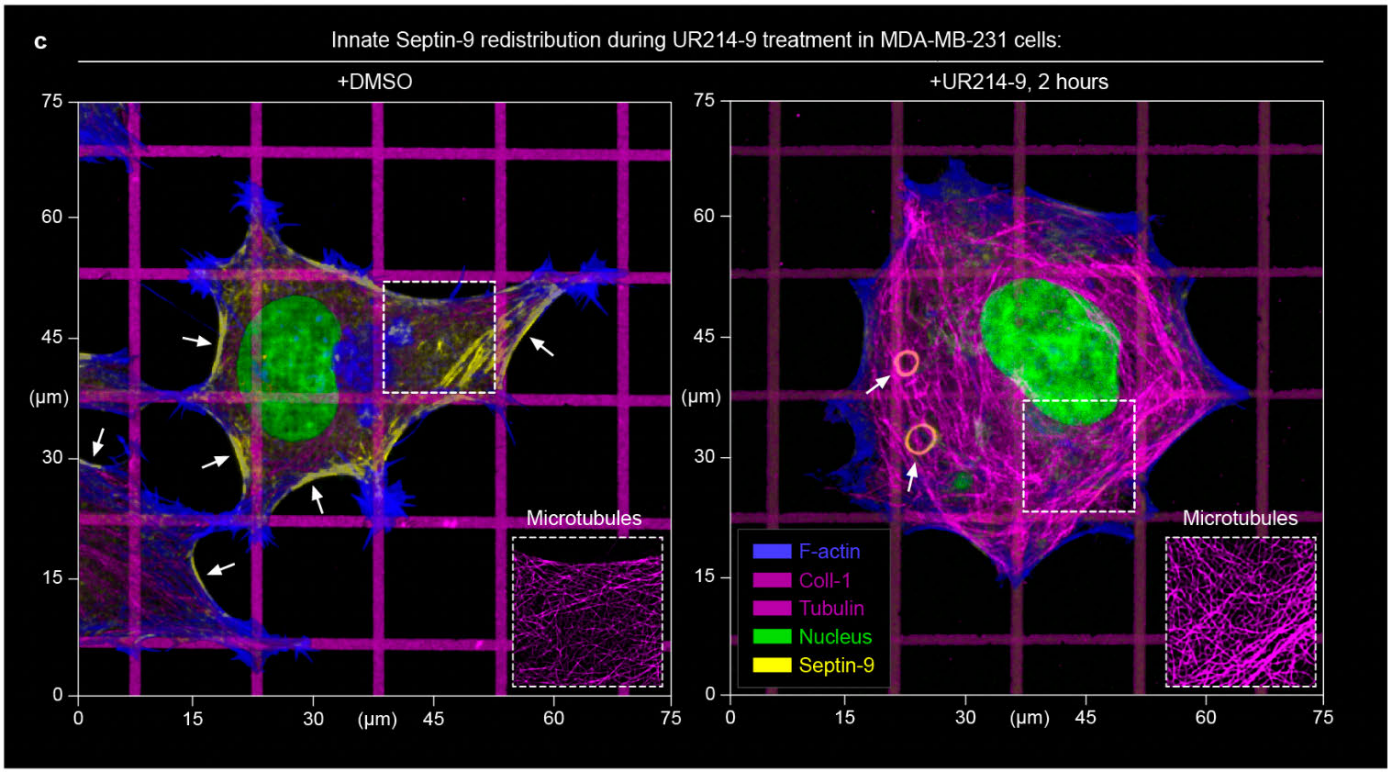
c
Innate Septin-9 redistribution during UR214-9 treatment in MDA-MB-231 cells:
+DMSO
+UR214-9, 2 hours
Microtubules
F-actin
Coll-1
Tubulin
Nucleus
Septin-9
(µm)

Supplemental figure SI3. Septin cytoskeleton (Septin-9) colocalizes with the mechanically stressed actomyosin network (stress-fibers) and disintegrate both in the presence of septin inhibitor (+UR214-9) or during suppression of actomyosin contractility (+Blebbistatin).

(a) *Left* - GFP-Septin-9 overexpressing and fully spread MDA-MB-231 cells display the Septin-9 filaments in both radial dorsoventral stress-fibers and within the transverse arcs **(+DMSO)**, while (*center*) septin inhibitor induces septin filaments (as shown with Septin-9, IF) disintegration **(+UR214-9, 1 hour)**, and (*right*) a complete cell detachment and cytoskeletal network collapse **(+UR214-9, 4 hours)**.

(b) Septin network (Septin-9) and F-actin (phalloidin) networks disintegrate as a result of actomyosin contractility inhibition **(+Blebbistatin)**.

(c) In control conditions **(+DMSO)** biaxial cells spreading along the orthogonal collagen-1 grid results with the polygonal spreading architecture. Free cell edges inherently feature linear anisotropy that within contractile cytoskeleton results with contractile actomyosin fiber alignment, and as a result - the highest tension and most developed stress-fibers. Note the most tensile regions of the cells accumulate the most of septin-9 (white arrows), while UR214-9 septin deactivation induces septin-9 translocation from actomyosin fibers to the microtubules.

MDA-MB-231 on biomimetic collagen “fibers” grid develop the adhesion anisotropy-driven tensed free cell edge stress-fibers at the cell periphery that coincide with innate Septin-9 filaments network **(+DMSO**, *arrows***)**, while septin inhibitor induces relocation of the innate Septin-9 onto the MT network **(+UR214-9)**, followed by the Septin-9-induced kinesin activation, and kinesin-driven microtubular rings formation (*arrows*).

Insets in dashed boxes show the enhanced deconvoluted details of the microtubular architectures.

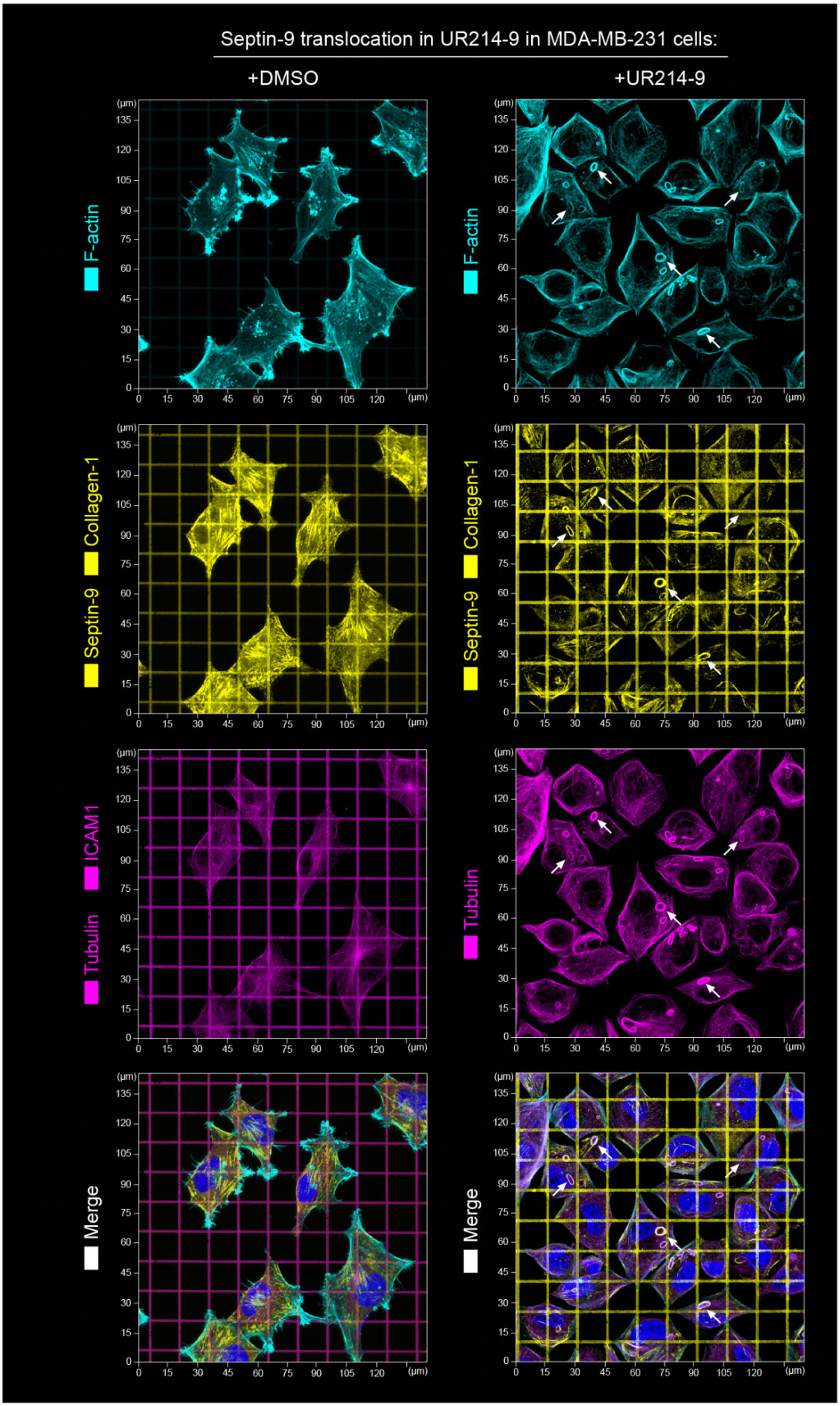
Septin-9 translocation in UR214-9 in MDA-MB-231 cells:
+DMSO
+UR214-9
F-actin
Septin-9
Collagen-1
Tubulin
ICAM1
Merge
(µm)
0
15
30
45
60
75
90
105
120
135

Supplemental figure SI4. Septins inhibition with UR214-9 in MDA-MB-231 cells on collagen (type I) grids induces a population-wide translocation of septin-9 isoform from the actomyosin stress-fibers onto microtubules.

Top - Septin-9 in vehicle-treated cells **(+DMSO)** strongly colocalizes with linear F-actin structures (stress-fibers).

Bottom - Septin-9 translocates onto the microtubular apparatus during septins GTPase activity suppression **(+UR2214-9,** t≥1 hour**)** due to its MAP-like motif. GTPase-inactive septin-9 acts as a MAP, stabilizes microtubules and induces MT curling into the rings (*arrows*) *via* previously described kinesins overactivation (Zhovmer et al., 2021).

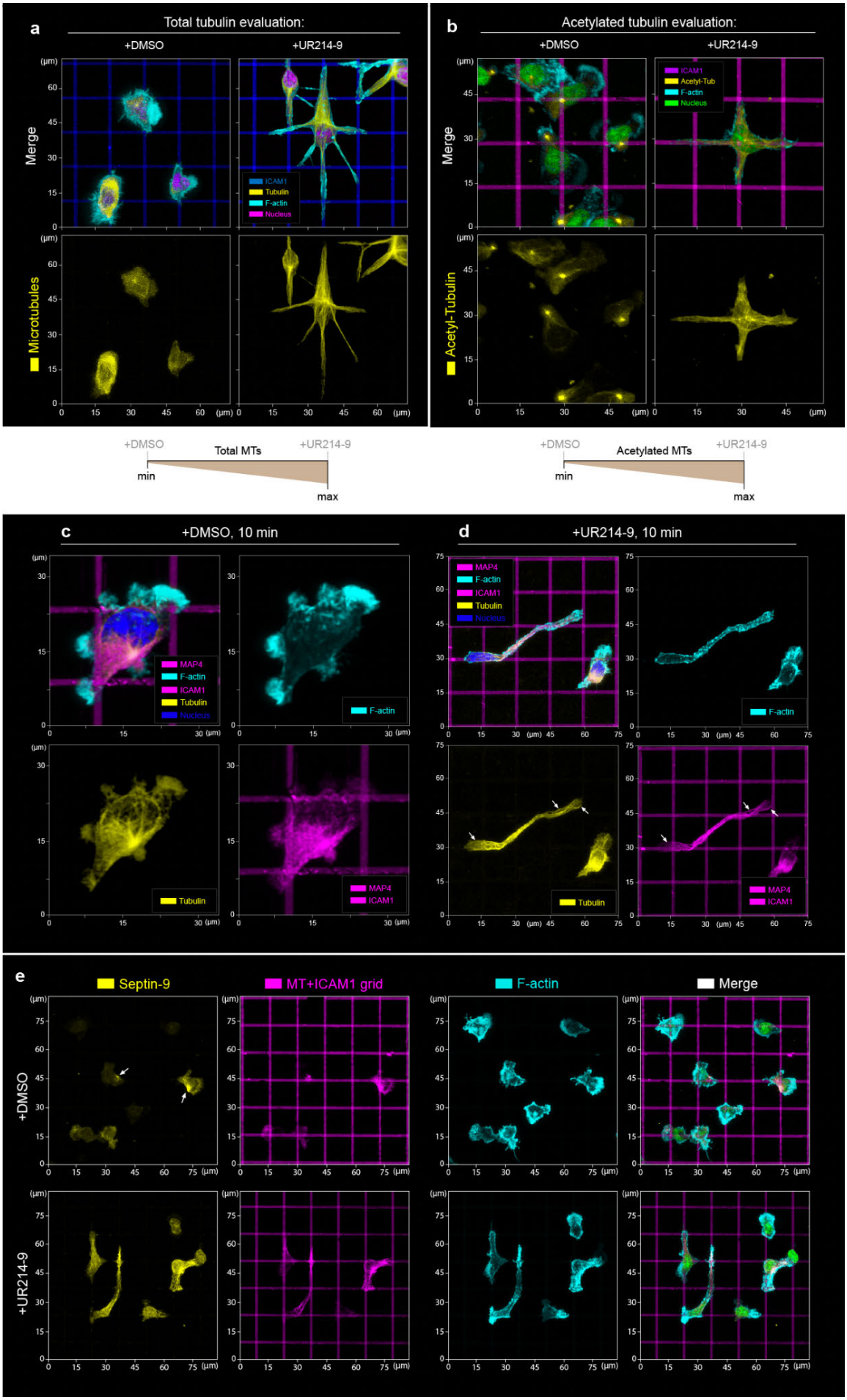
a
Total tubulin evaluation:
+DMSO
+UR214-9
Merge
Microtubules
ICAM1
Tubulin
F-actin
Nucleus
b
Acetylated tubulin evaluation:
+DMSO
+UR214-9
Merge
Acetyl-Tubulin
ICAM1
Acetyl-Tub
F-actin
Nucleus
+DMSO
Total MTs
+UR214-9
min
max
+DMSO
Acetylated MTs
+UR214-9
min
max
c
+DMSO, 10 min
MAP4
F-actin
ICAM1
Tubulin
Nucleus
d
+UR214-9, 10 min
MAP4
F-actin
ICAM1
Tubulin
Nucleus
e
Septin-9
MT+ICAM1 grid
F-actin
Merge
+DMSO
+UR214-9

Supplemental figure SI5. UR214-9-induced septin inactivation and amoeboid-to-mesenchymal-like T cell transition displays microtubules post-translational modifications, MAP4-MT adsorption, MTs elongation and densification.

(a) hCD4+ T cells during control vehicle treatment **(+DMSO)** maintain diffuse, low density MT architecture and amoeboid phenotype, featuring neither spreading nor alignment along the T cell adhesion cues (ICAM1 anisotropic parallel lines). Septin inhibition **(+UR214-9)** induces T cell dendritization along the ICAM1 grid and MT apparatus buildup.

(b) MT IF analysis displays an increased MT acetylation that accompanies MT apparatus build-up during septin inhibition **(+UR214-9)** as compared to the control T cells **(+DMSO)**.

(c-d) MAP4-MT adsorption analysis across control **(c, +DMSO)**, septin-inhibited **(d, +UR214-9)** T cells indicates that UR214-9 induces MAP4 accumulation (*arrows*) on the structurally densified and elongated MT apparatus, as compared to the cytosolic diffuse MAP4 distribution in the control T cells.

(e) Septin-9 microtubular translocation, induced by septins GTPase activity suppression **(+UR214-9)**.

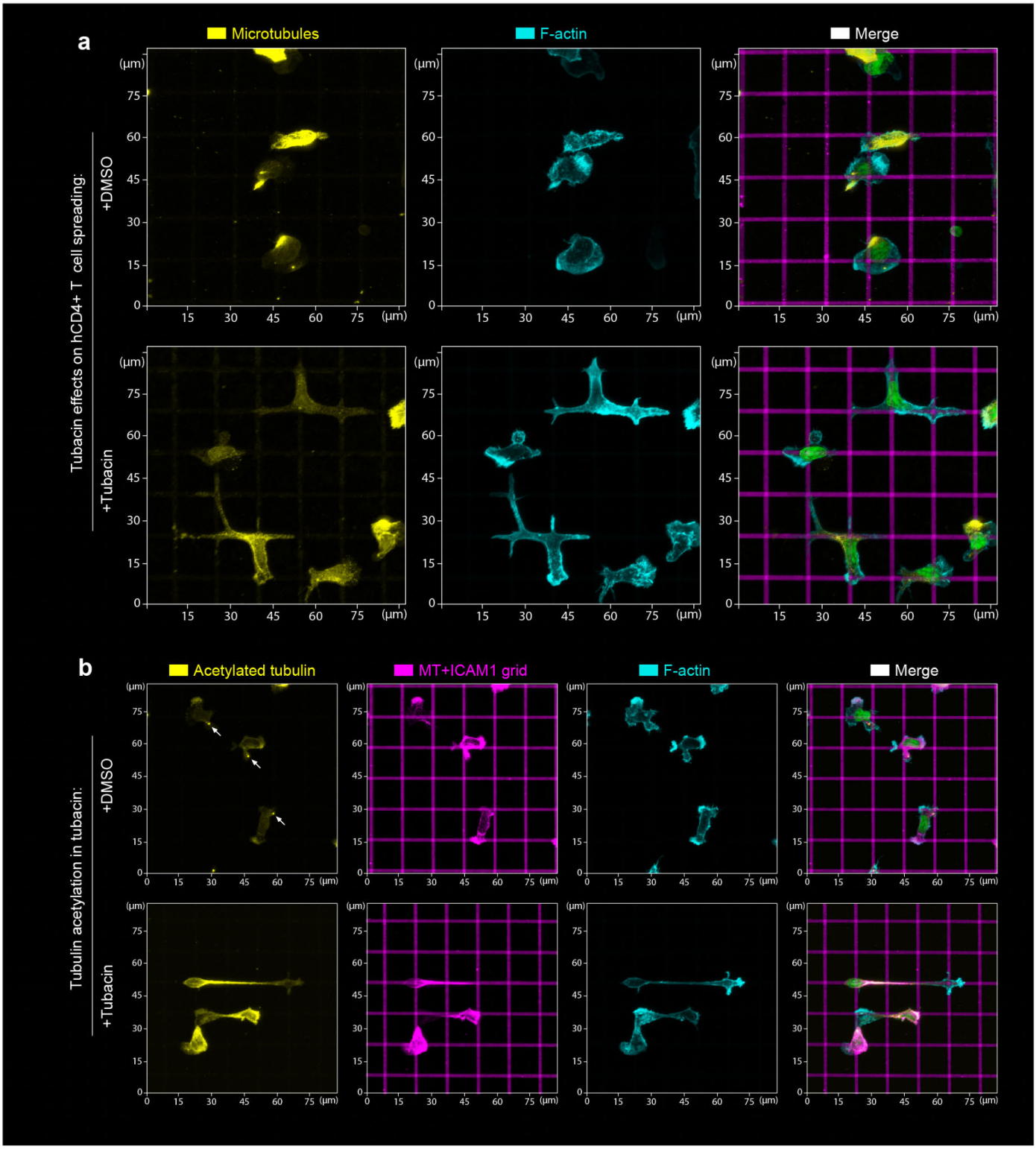

Supplemental figure SI6. Microtubules stabilization *via* Tubacin-induced hyperacetylation causes phenocopying of the UR214-9-induced hCD4+ T cell transitioning towards mesenchymal-like dendritic spreading.

(a) hCD4+ T cells during HDAC6 suppression **(+Tubacin,** t≥1 hour**)** display a partial amoeboid-to-mesenchymal-like transitioning, T cell dendritic spreading along the ICAM1 grids.

(b) Evaluation of the MT hyperacetylation in hCD4+ T cells, induced by HDAC6 suppression **(+Tubacin,** t≥1 hour**)** indicates a robust microtubular apparatus acetylation increase in comparison to the control T cell group **(+DMSO)**.

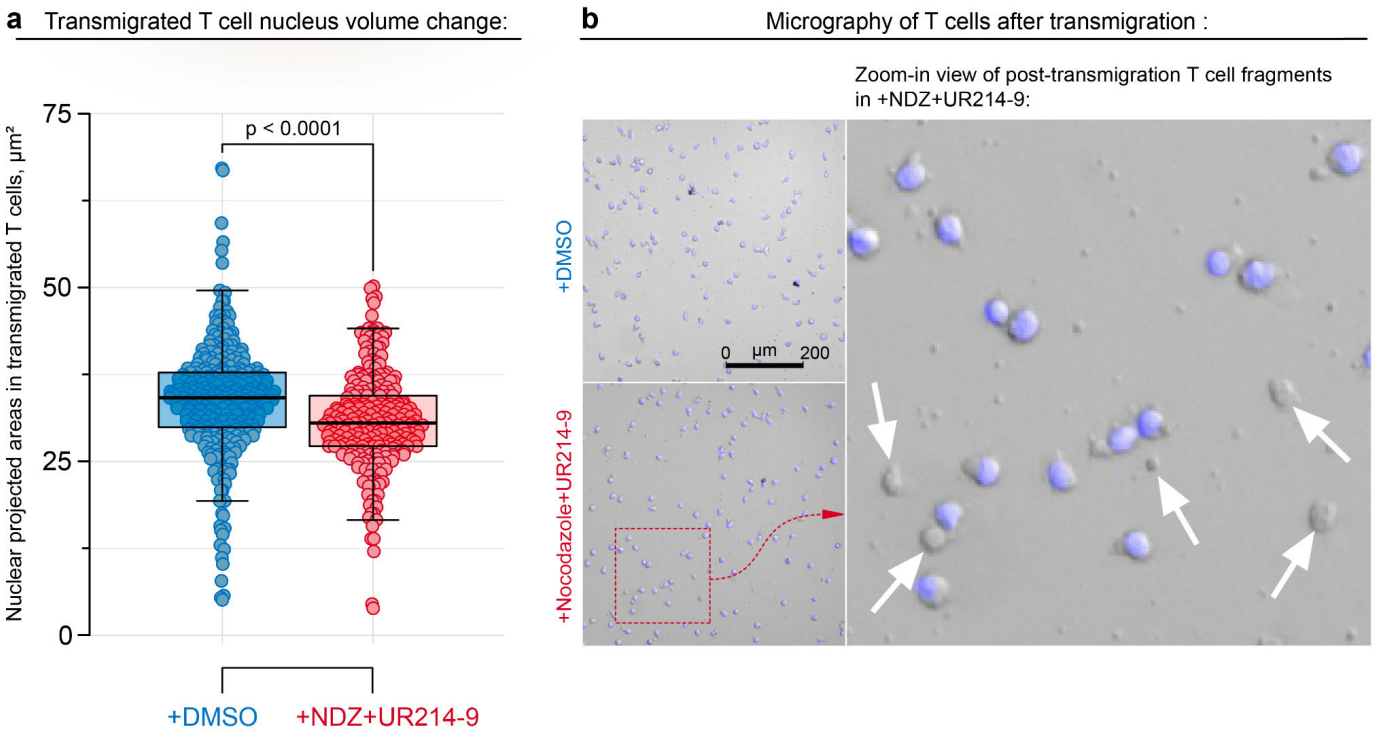

Supplemental figure SI7. Loss of hCD8+ T cell structural stability during enhanced transmigration induced by microtubules destabilization and septins inhibition (+Nocodazole+UR214-9).

(a) Evaluation of the population-wide hCD8+ T cells nuclei sizes (2D projected nucleus areas) after transmigration in control **(+DMSO)** and treated **(+Nocodazole+UR214-9)** T cell groups displays an ~11% loss of the nuclear sizes in the treated cells.

(b) Micrography views (brightfield and Hoechst) of post-transmigration T cells. +Nocodazole+UR214-9-treated T cells form numerous enucleated cell fragments in the post-transmigration fraction (*arrows*).

REFERENCES

Adams, G., Jr, Preciado-Lopez, M., Fischer, R.S., Baird, M.A., Logue, J., and Waterman, C.M. (2018). Functional Behavior of Melanoma Cells Under High Confinement, High Contractility and Low Adhesion Mediating Leader Bleb Based Motility. In MOLECULAR BIOLOGY OF THE CELL, (AMER SOC CELL BIOLOGY 8120 WOODMONT AVE, STE 750, BETHESDA, MD 20814-2755 USA),.

Adams, G., Jr, López, M.P., Cartagena-Rivera, A.X., and Waterman, C.M. (2021). Survey of cancer cell anatomy in nonadhesive confinement reveals a role for filamin-A and fascin-1 in leader bleb-based migration. Mol. Biol. Cell *32*, 1772–1791.

Ageta-Ishihara, N., Miyata, T., Ohshima, C., Watanabe, M., Sato, Y., Hamamura, Y., Higashiyama, T., Mazitschek, R., Bito, H., and Kinoshita, M. (2013). Septins promote dendrite and axon development by negatively regulating microtubule stability via HDAC6-mediated deacetylation. Nat. Commun. *4*, 1–11.

Alper, J.D., Decker, F., Agana, B., and Howard, J. (2014). The motility of axonemal dynein is regulated by the tubulin code. Biophys. J. *107*, 2872–2880.

Aoun, L., Farutin, A., Garcia-Seyda, N., Nègre, P., Rizvi, M.S., Tlili, S., Song, S., Luo, X., Biarnes-Pelicot, M., Galland, R., et al. (2020). Amoeboid Swimming Is Propelled by Molecular Paddling in Lymphocytes. Biophys. J. *119*, 1157–1177.

Badding, M.A., and Dean, D.A. (2012). Highly acetylated tubulin permits enhanced interactions with and trafficking of plasmids along microtubules. Gene Ther. *20*, 616–624.

Bai, X., Karasmanis, E.P., and Spiliotis, E.T. (2016). Septin 9 interacts with kinesin KIF17 and interferes with the mechanism of NMDA receptor cargo binding and transport. Mol. Biol. Cell *27*, 897–906.

Balzer, E.M., Tong, Z., Paul, C.D., Hung, W.-C., Stroka, K.M., Boggs, A.E., Martin, S.S., and Konstantopoulos, K. (2012). Physical confinement alters tumor cell adhesion and migration phenotypes. The FASEB Journal *26*, 4045–4056.

Beber, A., Taveneau, C., Nania, M., Tsai, F.-C., Di Cicco, A., Bassereau, P., Lévy, D., Cabral, J.T., Isambert, H., Mangenot, S., et al. (2019). Membrane reshaping by micrometric curvature sensitive septin filaments. Nat. Commun. *10*, 420.

Bridges, A.A., and Gladfelter, A.S. (2015). Septin Form and Function at the Cell Cortex. J. Biol. Chem. *290*, 17173–17180.

Bustos-Morán, E., Blas-Rus, N., Martin-Cófreces, N.B., and Sánchez-Madrid, F. (2017). Microtubule-associated protein-4 controls nanovesicle dynamics and T cell activation. J. Cell Sci. *130*, 1217–1223.

Carey, S.P., Rahman, A., Kraning-Rush, C.M., Romero, B., Somasegar, S., Torre, O.M., Williams, R.M., and Reinhart-King, C.A. (2015). Comparative mechanisms of cancer cell migration through 3D matrix and physiological microtracks. Am. J. Physiol. Cell Physiol. *308*, C436–C447.

Cartagena-Rivera, A.X., Logue, J.S., Waterman, C.M., and Chadwick, R.S. (2016). Actomyosin Cortical Mechanical Properties in Nonadherent Cells Determined by Atomic Force Microscopy. Biophys. J. *110*, 2528–2539.

Charras, G., and Paluch, E. (2008). Blebs lead the way: how to migrate without lamellipodia. Nat. Rev. Mol. Cell Biol. *9*, 730–736.

Charras, G.T., Yarrow, J.C., Horton, M.A., Mahadevan, L., and Mitchison, T.J. (2005). Non-equilibration of hydrostatic pressure in blebbing cells. Nature *435*, 365–369.

Charras, G.T., Hu, C.-K., Coughlin, M., and Mitchison, T.J. (2006). Reassembly of contractile actin cortex in cell blebs. J. Cell Biol. *175*, 477–490.

Cheffings, T.H., Burroughs, N.J., and Balasubramanian, M.K. (2016). Actomyosin Ring Formation and Tension Generation in Eukaryotic Cytokinesis. Curr. Biol. *26*, R719–R737.

Chen, W., Lou, J., and Zhu, C. (2010). Forcing Switch from Short- to Intermediate- and Long-lived States of the αA Domain Generates LFA-1/ICAM-1 Catch Bonds *. J. Biol. Chem. *285*, 35967–35978.

Ding, F., Yin, S., and Dokholyan, N.V. (2010). Rapid flexible docking using a stochastic rotamer library of ligands. J. Chem. Inf. Model. *50*, 1623–1632.

Dolat, L., Hunyara, J.L., Bowen, J.R., Karasmanis, E.P., Elgawly, M., Galkin, V.E., and Spiliotis, E.T. (2014). Septins promote stress fiber--mediated maturation of focal adhesions and renal epithelial motility. J. Cell Biol. *207*, 225–235.

Estey, M.P., Di Ciano-Oliveira, C., Froese, C.D., Bejide, M.T., and Trimble, W.S. (2010). Distinct roles of septins in cytokinesis: SEPT9 mediates midbody abscission. J. Cell Biol. *191*, 741–749.

Filippi, M.-D. (2016). Mechanism of Diapedesis: Importance of the Transcellular Route. Adv. Immunol. *129*, 25–53.

Fischer, R.S., Myers, K.A., Gardel, M.L., and Waterman, C.M. (2012). Stiffness-controlled three-dimensional extracellular matrices for high-resolution imaging of cell behavior. Nat. Protoc. *7*, 2056–2066.

Fokin, A.I., David, V., Oguievetskaia, K., Derivery, E., Stone, C.E., Cao, L., Rocques, N., Molinie, N., Henriot, V., Aumont-Nicaise, M., et al. (2021). The Arp1/11 minifilament of dynactin primes the endosomal Arp2/3 complex. Sci Adv *7*.

Founounou, N., Loyer, N., and Le Borgne, R. (2013). Septins regulate the contractility of the actomyosin ring to enable adherens junction remodeling during cytokinesis of epithelial cells. Dev. Cell *24*, 242–255.

Fritzsche, M., Lewalle, A., Duke, T., Kruse, K., and Charras, G. (2013). Analysis of turnover dynamics of the submembranous actin cortex. Mol. Biol. Cell *24*, 757–767.

Füchtbauer, A., Lassen, L.B., Jensen, A.B., Howard, J., Quiroga, A. de S., Warming, S., Sørensen, A.B., Pedersen, F.S., and Füchtbauer, E.-M. (2011). Septin9 is involved in septin filament formation and cellular stability. Biol. Chem. *392*, 769–777.

Gilden, J.K., Peck, S., Chen, Y.-C.M., and Krummel, M.F. (2012). The septin cytoskeleton facilitates membrane retraction during motility and blebbing. J. Cell Biol. *196*, 103–114.

van der Gucht, J., Paluch, E., Plastino, J., and Sykes, C. (2005). Stress release drives symmetry breaking for actin-based movement. Proceedings of the National Academy of Sciences *102*, 7847–7852.

Hu, Q., Nelson, W.J., and Spiliotis, E.T. (2008). Forchlorfenuron alters mammalian septin assembly, organization, and dynamics. J. Biol. Chem. *283*, 29563–29571.

Hung, W.-C., Chen, S.-H., Paul, C.D., Stroka, K.M., Lo, Y.-C., Yang, J.T., and Konstantopoulos, K. (2013). Distinct signaling mechanisms regulate migration in unconfined versus confined spaces. J. Cell Biol. *202*, 807–824.

Hynes, R.O. (2002). Integrins: bidirectional, allosteric signaling machines. Cell *110*, 673–687.

Jacobelli, J., Friedman, R.S., Conti, M.A., Lennon-Dumenil, A.-M., Piel, M., Sorensen, C.M., Adelstein, R.S., and Krummel, M.F. (2010). Confinement-optimized three-dimensional T cell amoeboid motility is modulated via myosin IIA-regulated adhesions. Nat. Immunol. *11*, 953–961.

Jimenez, A.J., Schaeffer, A., De Pascalis, C., Letort, G., Vianay, B., Bornens, M., Piel, M., Blanchoin, L., and Théry, M. (2021). Acto-myosin network geometry defines centrosome position. Curr. Biol.

Kim, D., You, E., and Rhee, S. (2012). Dynein regulates cell migration depending on substrate rigidity. Int.

J. Mol. Med. *29*, 440–446.

Kim, K.K., Singh, R.K., Khazan, N., Kodza, A., Singh, N.A., Jones, A., Sivagnanalingam, U., Towner, M., Itamochi, H., Turner, R., et al. (2020). Development of Potent Forchlorfenuron Analogs and Their Cytotoxic Effect in Cancer Cell Lines. Sci. Rep. *10*, 3241.

Kim, M.S., Froese, C.D., Estey, M.P., and Trimble, W.S. (2011). SEPT9 occupies the terminal positions in septin octamers and mediates polymerization-dependent functions in abscission. J. Cell Biol. *195*, 815–826.

Kinoshita, M., and Noda, M. (2001). Roles of septins in the mammalian cytokinesis machinery. Cell Struct. Funct. *26*, 667–670.

Kinoshita, M., Field, C.M., Coughlin, M.L., Straight, A.F., and Mitchison, T.J. (2002). Self- and actin-templated assembly of Mammalian septins. Dev. Cell *3*, 791–802.

Kopf, A., and Kiermaier, E. (2021). Dynamic Microtubule Arrays in Leukocytes and Their Role in Cell Migration and Immune Synapse Formation. Front Cell Dev Biol *9*, 635511.

Kopf, A., Renkawitz, J., Hauschild, R., Girkontaite, I., Tedford, K., Merrin, J., Thorn-Seshold, O., Trauner, D., Häcker, H., Fischer, K.-D., et al. (2020). Microtubules control cellular shape and coherence in amoeboid migrating cells. J. Cell Biol. *219*.

Kremer, B.E., Haystead, T., and Macara, I.G. (2005). Mammalian Septins Regulate Microtubule Stability through Interaction with the Microtubule-binding Protein MAP4. MBoC *16*, 4648–4659.

Kremer, B.E., Adang, L.A., and Macara, I.G. (2007). Septins regulate actin organization and cell-cycle arrest through nuclear accumulation of NCK mediated by SOCS7. Cell *130*, 837–850.

Krendel, M., Zenke, F.T., and Bokoch, G.M. (2002). Nucleotide exchange factor GEF-H1 mediates cross-talk between microtubules and the actin cytoskeleton. Nat. Cell Biol. *4*, 294–301.

Krummel, M.F., Friedman, R.S., and Jacobelli, J. (2014). Modes and mechanisms of T cell motility: roles for confinement and Myosin-IIA. Curr. Opin. Cell Biol. *30*, 9–16.

Krummel, M.F., Bartumeus, F., and Gérard, A. (2016). T cell migration, search strategies and mechanisms. Nat. Rev. Immunol. *16*, 193–201.

Kuzmić, M., Castro Linares, G., Fialová, J.L., Iv, F., Salaün, D., Llewellyn, A., Gomes, M., Belhabib, M., Liu, Y., Asano, K., et al. (2021a). Septin-microtubule association requires a MAP-like motif unique to Sept9 isoform 1 embedded into septin octamers.

Kuzmić, M., Linares, G.C., Fialová, J.L., Iv, F., Salaün, D., Llewellyn, A., Gomes, M., Belhabib, M., Liu, Y., Asano, K., et al. (2021b). Septin-microtubule association via a motif unique to the isoform 1 of septin 9 tunes stress fibers. J. Cell Sci.

Lehtimäki, J.I., Rajakylä, E.K., Tojkander, S., and Lappalainen, P. (2021). Generation of stress fibers through myosin-driven reorganization of the actin cortex. Elife *10*.

Ley, K., Laudanna, C., Cybulsky, M.I., and Nourshargh, S. (2007). Getting to the site of inflammation: the leukocyte adhesion cascade updated. Nat. Rev. Immunol. *7*, 678–689.

Liu, Y.-J., Le Berre, M., Lautenschlaeger, F., Maiuri, P., Callan-Jones, A., Heuzé, M., Takaki, T., Voituriez, R., and Piel, M. (2015). Confinement and low adhesion induce fast amoeboid migration of slow mesenchymal cells. Cell *160*, 659–672.

Logue, J.S., Cartagena-Rivera, A.X., Baird, M.A., Davidson, M.W., Chadwick, R.S., and Waterman, C.M. (2015). Erk regulation of actin capping and bundling by Eps8 promotes cortex tension and leader bleb-based migration. Elife *4*, e08314.

McEvoy, E., Deshpande, V.S., and McGarry, P. (2017). Free energy analysis of cell spreading. J. Mech. Behav. Biomed. Mater. *74*, 283–295.

McKenney, R.J., Huynh, W., Vale, R.D., and Sirajuddin, M. (2016). Tyrosination of α-tubulin controls the initiation of processive dynein-dynactin motility. EMBO J. *35*, 1175–1185.

Mostowy, S., and Cossart, P. (2012). Septins: the fourth component of the cytoskeleton. Nat. Rev. Mol. Cell Biol. *13*, 183–194.

Nakos, K., Rosenberg, M., and Spiliotis, E.T. (2019). Regulation of microtubule plus end dynamics by septin 9. Cytoskeleton *76*, 83–91.

Neubauer, K., and Zieger, B. (2017). The Mammalian Septin Interactome. Front Cell Dev Biol *5*, 3.

Niggli, V. (2003). Microtubule-disruption-induced and chemotactic-peptide-induced migration of human neutrophils: implications for differential sets of signalling pathways. J. Cell Sci. *116*, 813–822.

Nordenfelt, P., Elliott, H.L., and Springer, T.A. (2016). Coordinated integrin activation by actin-dependent force during T-cell migration. Nat. Commun. *7*, 1–15.

Odom, T.W., Love, J.C., Wolfe, D.B., Paul, K.E., and Whitesides, G.M. (2002). Improved Pattern Transfer in Soft Lithography Using Composite Stamps. Langmuir *18*, 5314–5320.

Oh, Y., and Bi, E. (2011). Septin structure and function in yeast and beyond. Trends Cell Biol. *21*, 141–148.

Paluch, E., Piel, M., Prost, J., Bornens, M., and Sykes, C. (2005). Cortical Actomyosin Breakage Triggers Shape Oscillations in Cells and Cell Fragments. Biophys. J. *89*, 724–733.

Paul, C.D., Mistriotis, P., and Konstantopoulos, K. (2017). Cancer cell motility: lessons from migration in confined spaces. Nat. Rev. Cancer *17*, 131–140.

Permana, S., Hisanaga, S.-I., Nagatomo, Y., Iida, J., Hotani, H., and Itoh, T.J. (2005). Truncation of the projection domain of MAP4 (microtubule-associated protein 4) leads to attenuation of microtubule dynamic instability. Cell Struct. Funct. *29*, 147–157.

Plotnikov, S.V., Sabass, B., Schwarz, U.S., and Waterman, C.M. (2014a). High-resolution traction force microscopy. Methods Cell Biol. *123*, 367–394.

Plotnikov, S.V., Sabass, B., Schwarz, U.S., and Waterman, C.M. (2014b). High-resolution traction force microscopy. Methods Cell Biol. *123*, 367–394.

Ramachandran, S., Kota, P., Ding, F., and Dokholyan, N.V. (2011). Automated minimization of steric clashes in protein structures. Proteins *79*, 261–270.

Raman, P.S., Paul, C.D., Stroka, K.M., and Konstantopoulos, K. (2013). Probing cell traction forces in confined microenvironments. Lab Chip *13*, 4599–4607.

Renkawitz, J., and Sixt, M. (2010). Mechanisms of force generation and force transmission during interstitial leukocyte migration. EMBO Rep. *11*, 744–750.

Renkawitz, J., Schumann, K., Weber, M., Lämmermann, T., Pflicke, H., Piel, M., Polleux, J., Spatz, J.P., and Sixt, M. (2009). Adaptive force transmission in amoeboid cell migration. Nat. Cell Biol. *11*, 1438–1443.

Renkawitz, J., Kopf, A., Stopp, J., de Vries, I., Driscoll, M.K., Merrin, J., Hauschild, R., Welf, E.S., Danuser, G., Fiolka, R., et al. (2019). Nuclear positioning facilitates amoeboid migration along the path of least resistance. Nature *568*, 546–550.

Reversat, A., Gaertner, F., Merrin, J., Stopp, J., Tasciyan, S., Aguilera, J., de Vries, I., Hauschild, R., Hons, M., Piel, M., et al. (2020). Cellular locomotion using environmental topography. Nature *582*, 582–585.

Rhee, S., Jiang, H., Ho, C.-H., and Grinnell, F. (2007). Microtubule function in fibroblast spreading is modulated according to the tension state of cell--matrix interactions. Proceedings of the National Academy of Sciences *104*, 5425–5430.

Rolli, C.G., Seufferlein, T., Kemkemer, R., and Spatz, J.P. (2010). Impact of tumor cell cytoskeleton organization on invasiveness and migration: a microchannel-based approach. PLoS One *5*, e8726.

Ruprecht, V., Wieser, S., Callan-Jones, A., Smutny, M., Morita, H., Sako, K., Barone, V., Ritsch-Marte, M., Sixt, M., Voituriez, R., et al. (2015). Cortical contractility triggers a stochastic switch to fast amoeboid cell motility. Cell *160*, 673–685.

Sadjadi, Z., Zhao, R., Hoth, M., Qu, B., and Rieger, H. (2020). Migration of Cytotoxic T Lymphocytes in 3D Collagen Matrices. Biophys. J. *119*, 2141–2152.

Salameh, J., Cantaloube, I., Benoit, B., Poüs, C., and Baillet, A. (2021). Cdc42 and its BORG2 and BORG3 effectors control the subcellular localization of septins between actin stress fibers and microtubules. Curr. Biol.

Schmid, H., and Michel, B. (2000). Siloxane Polymers for High-Resolution, High-Accuracy Soft Lithography. Macromolecules *33*, 3042–3049.

Schmidt, K., and Nichols, B.J. (2004). Functional interdependence between septin and actin cytoskeleton. BMC Cell Biol. *5*, 43.

Schwede, T., Kopp, J., Guex, N., and Peitsch, M.C. (2003). SWISS-MODEL: An automated protein homology-modeling server. Nucleic Acids Res. *31*, 3381–3385.

Shakiba, D., Alisafaei, F., Savadipour, A., Rowe, R.A., Liu, Z., Pryse, K.M., Shenoy, V.B., Elson, E.L., and Genin, G.M. (2020). The Balance between Actomyosin Contractility and Microtubule Polymerization Regulates Hierarchical Protrusions That Govern Efficient Fibroblast–Collagen Interactions. ACS Nano *14*, 7868–7879.

Singh, R.K., Kim, K.K., Khazan, N., Rowswell-Turner, R.B., Laggner, C., Jones, A., Srivastava, P., Hovanesian, V., Lamere, L., Conley, T., et al. (2020). Septins disruption controls tumor growth and enhances efficacy of Herceptin.

Spiliotis, E.T. (2018). Spatial effects − site-specific regulation of actin and microtubule organization by septin GTPases. J. Cell Sci. *131*, jcs207555.

Spiliotis, E.T., and Nakos, K. (2021). Cellular functions of actin- and microtubule-associated septins. Curr. Biol. *31*, R651–R666.

Stroka, K.M., Jiang, H., Chen, S.-H., Tong, Z., Wirtz, D., Sun, S.X., and Konstantopoulos, K. (2014). Water Permeation Drives Tumor Cell Migration in Confined Microenvironments. Cell *157*, 611–623.

Tabdanov, E., Gondarenko, S., Kumari, S., Liapis, A., Dustin, M.L., Sheetz, M.P., Kam, L.C., and Iskratsch, T. (2015). Micropatterning of TCR and LFA-1 ligands reveals complementary effects on cytoskeleton mechanics in T cells. Integr. Biol. *7*, 1272–1284.

Tabdanov, E.D., Puram, V.V., Win, Z., Alamgir, A., Alford, P.W., and Provenzano, P.P. (2018a). Bimodal sensing of guidance cues in mechanically distinct microenvironments. Nat. Commun. *9*, 4891.

Tabdanov, E.D., Puram, V., Zhovmer, A., and Provenzano, P.P. (2018b). Microtubule-Actomyosin Mechanical Cooperation during Contact Guidance Sensing. Cell Rep. *25*, 328–338.e5.

Tabdanov, E.D., Zhovmer, A.S., Puram, V., and Provenzano, P.P. (2020). Engineering Elastic Nano-and Micro-Patterns and Textures for Directed Cell Motility. STAR Protocols.

Tabdanov, E.D., Rodríguez-Merced, N.J., Cartagena-Rivera, A.X., Puram, V.V., Callaway, M.K., Ensminger, E.A., Pomeroy, E.J., Yamamoto, K., Lahr, W.S., Webber, B.R., et al. (2021). Engineering T cells to enhance

3D migration through structurally and mechanically complex tumor microenvironments. Nat. Commun. *12*, 2815.

Takesono, A., Heasman, S.J., Wojciak-Stothard, B., Garg, R., and Ridley, A.J. (2010). Microtubules regulate migratory polarity through Rho/ROCK signaling in T cells. PLoS One *5*, e8774.

Théry, M., Pépin, A., Dressaire, E., Chen, Y., and Bornens, M. (2006). Cell distribution of stress fibres in response to the geometry of the adhesive environment. Cell Motil. Cytoskeleton *63*, 341–355.

Tooley, A.J., Gilden, J., Jacobelli, J., Beemiller, P., Trimble, W.S., Kinoshita, M., and Krummel, M.F. (2009). Amoeboid T lymphocytes require the septin cytoskeleton for cortical integrity and persistent motility. Nat. Cell Biol. *11*, 17–26.

Vasiliev, J.M., Gelfand, I.M., Domnina, L.V., Ivanova, O.Y., Komm, S.G., and Olshevskaja, L.V. (1970). Effect of colcemid on the locomotory behaviour of fibroblasts. J. Embryol. Exp. Morphol. *24*, 625–640.

Vestweber, D. (2015). How leukocytes cross the vascular endothelium. Nat. Rev. Immunol. *15*, 692–704.

Vignaud, T., Copos, C., Leterrier, C., Toro-Nahuelpan, M., Tseng, Q., Mahamid, J., Blanchoin, L., Mogilner, A., Théry, M., and Kurzawa, L. (2021). Stress fibres are embedded in a contractile cortical network. Nat. Mater. *20*, 410–420.

Wang, J., and Dokholyan, N.V. (2019). MedusaDock 2.0: Efficient and Accurate Protein–Ligand Docking With Constraints. J. Chem. Inf. Model. *59*, 2509–2515.

Willms, E., Cabañas, C., Mäger, I., Wood, M.J.A., and Vader, P. (2018). Extracellular Vesicle Heterogeneity: Subpopulations, Isolation Techniques, and Diverse Functions in Cancer Progression. Front. Immunol. *9*, 738.

Wolf, K., Müller, R., Borgmann, S., Bröcker, E.-B., and Friedl, P. (2003). Amoeboid shape change and contact guidance: T-lymphocyte crawling through fibrillar collagen is independent of matrix remodeling by MMPs and other proteases. Blood *102*, 3262–3269.

Woods, B.L., and Gladfelter, A.S. (2021). The state of the septin cytoskeleton from assembly to function. Curr. Opin. Cell Biol. *68*, 105–112.

Yadav, S.K., Stojkov, D., Feigelson, S.W., Roncato, F., Simon, H.-U., Yousefi, S., and Alon, R. (2019). Chemokine-triggered microtubule polymerization promotes neutrophil chemotaxis and invasion but not transendothelial migration. J. Leukoc. Biol. *105*, 755–766.

Yin, S., Biedermannova, L., Vondrasek, J., and Dokholyan, N.V. (2008). MedusaScore: an accurate force field-based scoring function for virtual drug screening. J. Chem. Inf. Model. *48*, 1656–1662.

Zhovmer, A.S., Manning, A., Smith, C., Hayes, J.B., Burnette, D.T., Wang, J., Cartagena-Rivera, A.X., Dokholyan, N.V., Singh, R.K., and Tabdanov, E.D. (2021). Mechanical Counterbalance of Kinesin and Dynein Motors in a Microtubular Network Regulates Cell Mechanics, 3D Architecture, and Mechanosensing. ACS Nano.